



Boiling and Two-Phase Flow Laboratory

Final Report on PHYSICS-BASED MODELING AND MEASUREMENT OF HIGH-FLUX CONDENSATION HEAT TRANSFER

(Contract No. N000140811139)

by

Prof. Issam Mudawar
Sung-Min Kim
Joseph Kim

Boiling and Two-Phase Flow Laboratory
School of Mechanical Engineering
Purdue University
585 Purdue Mall
West Lafayette, IN 47907
Tel. (765) 494-5705

September 2011

Prepared for

Dr. Mark Spector
Office of Naval Research
Ships and Engineering Systems Division, Code 331
875 N. Randolph Street
Arlington, VA 22203-1995

REPORT DOCUMENTATION PAGE					Form Approved OMB No. 0704-0188	
The public reporting burden for this collection of information is estimated to average 1 hour per response, including the time for reviewing instructions, searching existing data sources, gathering and maintaining the data needed, and completing and reviewing the collection of information. Send comments regarding this burden estimate or any other aspect of this collection of information, including suggestions for reducing the burden, to Department of Defense, Washington Headquarters Services, Directorate for Information Operations and Reports (0704-0188), 1215 Jefferson Davis Highway, Suite 1204, Arlington, VA 22202-4302. Respondents should be aware that notwithstanding any other provision of law, no person shall be subject to any penalty for failing to comply with a collection of information if it does not display a currently valid OMB control number.						
PLEASE DO NOT RETURN YOUR FORM TO THE ABOVE ADDRESS.						
1. REPORT DATE (DD-MM-YYYY) 6-09-2011		2. REPORT TYPE Final		3. DATES COVERED (From - To) 01-10-2008 to 30-09-2011		
4. TITLE AND SUBTITLE Physics-Based Modeling and Measurement of High-Flux Condensation Heat Transfer				5a. CONTRACT NUMBER NA		
				5b. GRANT NUMBER N00014-08-1-1139		
				5c. PROGRAM ELEMENT NUMBER NA		
6. AUTHOR(S) Mudawar, Issam Kim, Sung-Min Kim, Joseph				5d. PROJECT NUMBER NA		
				5e. TASK NUMBER NA		
				5f. WORK UNIT NUMBER NA		
7. PERFORMING ORGANIZATION NAME(S) AND ADDRESS(ES) Purdue University Boiling and Two-Phase Flow Laboratory Mechanical Engineering Building, 585 Purdue Mall West Lafayette, IN 47907				8. PERFORMING ORGANIZATION REPORT NUMBER N00014-08-1-1139-FR		
9. SPONSORING/MONITORING AGENCY NAME(S) AND ADDRESS(ES) Office of Naval Research ATTN: Dr. Mark Spector Ships and Engineering Systems Division, ONR Code 331 875 N. Randolph Street Arlington, VA 22203-1995				10. SPONSOR/MONITOR'S ACRONYM(S) ONR		
				11. SPONSOR/MONITOR'S REPORT NUMBER(S) NA		
12. DISTRIBUTION/AVAILABILITY STATEMENT Unlimited						
13. SUPPLEMENTARY NOTES NA						
14. ABSTRACT This report examines condensation of FC-72 along parallel, square micro-channels with a hydraulic diameter of 1 mm and a length of 29.9 cm, which are formed in the top surface of a solid copper plate. Using high-speed video imaging and photomicrographic techniques, five distinct flow regimes are identified: smooth-annular, wavy-annular, transition, slug, and bubbly, with the smooth-annular and wavy-annular regimes being most prevalent. A theoretical control-volume-based model is proposed based on the assumptions of smooth interface between the annular liquid film and vapor core, and uniform film thickness around the channel's circumference. The new model accurately captures the pressure drop and heat transfer coefficient data in both magnitude and trend, evidenced by mean absolute error values of 3.6% and 9.3%, respectively.						
15. SUBJECT TERMS phase change, condensation, electronics cooling, micro-channel, high-flux						
16. SECURITY CLASSIFICATION OF:			17. LIMITATION OF ABSTRACT	18. NUMBER OF PAGES	19a. NAME OF RESPONSIBLE PERSON	
a. REPORT	b. ABSTRACT	c. THIS PAGE			Mudawar, Issam	
U	U	U	UU	107	19b. TELEPHONE NUMBER (Include area code) 765-494-5705	

Reset

**PHYSICS-BASED MODELING AND MEASUREMENT OF HIGH-FLUX
CONDENSATION HEAT TRANSFER**

(Contract No. N000140811139)

by

Prof. Issam Mudawar
Sung-Min Kim
Joseph Kim

Boiling and Two-Phase Flow Laboratory
School of Mechanical Engineering
Purdue University
585 Purdue Mall
West Lafayette, IN 47907
Tel. (765) 494-5705

September 2011

Final Report

Prepared for

Dr. Mark Spector
Office of Naval Research
Ships and Engineering Systems Division, Code 331
875 N. Randolph Street
Arlington, VA 22203-1995

TABLE OF CONTENTS

	Page
LIST OF TABLES	iv
LIST OF FIGURES	v
NOMENCLATURE	viii
ABSTRACT	xiii
CHAPTER 1. INTRODUCTION	1
1.1. Motivation for Study	1
1.2. Miniature Condenser for High-Flux Heat Rejection	2
1.3. Transport Phenomena in Micro-Channel Condenser	3
1.4. Two-Phase Flow Model for Annular Flow Condensation.....	4
1.5. Research Objectives	6
CHAPTER 2. EXPERIMENTAL METHODS	8
2.1. Condensation Flow Loop	8
2.2. Micro-Channel Condensation Module	10
2.3. Operating Conditions and Measurement Accuracy.....	13
CHAPTER 3. EXPERIMENTAL RESULTS	15
3.1. Flow Visualization Results.....	15
3.2. Two-Phase Pressure Drop Results.....	21
3.2.1. Experimental Results	21
3.2.2. Pressure Drop Components.....	21
3.2.3. Comparison with Different Pressure Drop Models and Correlations	25

3.3. Condensation Heat Transfer Results	35
3.3.1. Heat Transfer Data Reduction.....	35
3.3.2. Experimental Results	36
3.3.3. Comparison with Previous Heat Transfer Correlations	44
3.3.4. New Heat Transfer Correlation.....	48
CHAPTER 4. THEORETICAL MODEL.....	59
4.1. Model Development	59
4.1.1. Key Findings from Flow Visualization Experiments	59
4.1.2. Model Assumptions	59
4.1.3. Control Volume Analysis.....	62
4.1.4. Turbulence Model	66
4.1.5. Determination of Heat Transfer Coefficient	67
4.1.6. Calculation Procedure	68
4.1.7. Simplified Model	69
4.2. Model Results	70
4.2.1. Effect of Turbulent Damping Term	70
4.2.2. Effect of Mass Velocity	71
4.2.3. Validation of Model Predictions	74
CHAPTER 5. CONCLUSIONS	81
5.1. Condensation Pressure Drop	81
5.2. Condensation Heat Transfer	82
5.3. Theoretical Model for Annular Flow Condensation.....	83
LIST OF REFERENCES	85

LIST OF TABLES

Table	Page
2.1 Thermophysical properties of FC-72 at $T_{sat} = 60^{\circ}\text{C}$	8
2.2 Test section dimensions	10
3.1 Homogeneous equilibrium model for two-phase frictional pressure gradient, and corresponding MAE in predicting present total pressure drop data.....	26
3.2 Two-phase frictional pressure gradient correlations for macro-channels based on the separated flow model, and corresponding MAE in predicting present total pressure drop data.....	30
3.3 Two-phase frictional pressure gradient correlations for mini/micro-channels based on the separated flow model, and corresponding MAE in predicting present total pressure drop data	31
3.4 Condensation heat transfer correlations for annular flow regime with corresponding MAE in predicting present experimental data	45
3.5 Database for two-phase condensation heat transfer coefficient in mini/micro-channels	51
3.6 Comparison of mini/micro-channel database for annular flow (smooth-annular, wavy-annular and transition) with predictions of annular condensation heat transfer correlations	56

LIST OF FIGURES

Figure	Page
2.1 Schematic diagram of test loop.....	9
2.2 Photos of (a) micro-channel condensation module and (b) main part of test setup....	11
2.3 (a) Construction and (b) cross-sectional view of micro-channel condensation module	12
3.1 Representative (a) photographs and (b) schematics of FC-72 condensation flow regimes in three adjacent channels for $G = 68 \text{ kg/m}^2 \text{ s}$	16
3.2 Comparison of present FC-72 condensation flow regime data with those of (a) Wang <i>et al.</i> (2002) and (b) Triplett <i>et al.</i> (1999) and Chung and Kawaji (2004).....	17
3.3 Comparison of present FC-72 condensation flow regime boundaries with those of Soliman (1986) and Chen <i>et al.</i> (2006).....	20
3.4 Variation of measured total pressure drop with water mass flow rate for different FC- 72 mass velocities	22
3.5 Comparison of present FC-72 pressure drop data with predictions of (a) homogeneous equilibrium model, and (b) homogeneous equilibrium model with accelerational pressure drop based on separated flow model and Zivi (1964)'s relation for void fraction	27
3.6 Contributions of individual components of pressure drop to total pressure drop for different mass velocities and $\dot{m}_w = 3 \text{ g/s}$ predicted with the frictional pressure gradient determined by the homogenous equilibrium model using the viscosity model of Dukler <i>et al.</i> (1964), and the accelerational pressure gradient determined by the separated flow model using Zivi (1964)'s relation for void fraction	29
3.7 Comparison of present FC-72 pressure drop data with predictions of separated flow correlations recommended for (a) macro-channels and (b) mini/micro-channels	32
3.8 (a) Fundamental differences between annular condensation and annular flow boiling in micro-channels. (b) Effects of surface tension on liquid distribution along channel perimeter	34

Figure	Page
3.9 Unit cell for condensation micro-channel.....	37
3.10 Variations of copper block temperatures, base heat flux, and thermodynamic equilibrium quality along stream-wise direction for different FC-72 mass velocities with $\dot{m}_w = 3$ g/s	38
3.11 Variation of experimentally-determined local FC-72 condensation heat transfer coefficient with thermodynamic equilibrium quality for different coolant mass flow rates with (a) $G = 68$ kg/ m ² s, (b) $G = 118$ kg/ m ² s, (c) $G = 186$ kg/ m ² s, (d) $G = 248$ kg/ m ² s, (e) $G = 306$ kg/ m ² s, and (f) $G = 367$ kg/ m ² s.....	40
3.12 Variation of experimentally-determined local FC-72 condensation heat transfer coefficient with thermodynamic equilibrium quality for different FC-72 mass velocities with (a) $\dot{m}_w = 3$ g/s, and (b) $\dot{m}_w = 6$ g/s	41
3.13 Variation of experimentally-determined average FC-72 condensation heat transfer coefficient with coolant mass flow rate for different FC-72 mass velocities.....	43
3.14 Comparison of present experimentally-determined average FC-72 condensation heat transfer coefficient data with predictions of annular flow macro-channel condensation correlations	46
3.15 Comparison of present experimentally-determined average FC-72 condensation heat transfer coefficient data with predictions of annular flow mini/micro-channel condensation correlations	47
3.16 Comparison of present experimentally-determined average FC-72 condensation heat transfer coefficient data with predictions of the new annular condensation correlation	52
3.17 Variation of present experimentally-determined local FC-72 condensation heat transfer coefficient data with thermodynamic equilibrium quality for $G = 306$ kg/ m ² s and $\dot{m}_w = 5$ g/s compared to predictions of new correlation and previous annular condensation correlations.....	53
3.18 Reynolds number transition lines based on 923 mini/micro-channel data points from eight sources	54
3.19 Proposed flow regime map based on present FC-72 flow visualization experiments in square micro-channels with $D_h = 1$ mm plotted alongside 639 mini/micro-channel data points corresponding to $J_g^* > 2.5$ from eight sources	55
3.20 Comparison of predictions of new annular condensation heat transfer correlation with prior experimental mini/micro-channel data.....	57

Figure	Page
4.1 Schematic representations of (a) condenser with rectangular micro-channels and (b) liquid film condensation in micro-channel with three-sided wall cooling.....	61
4.2 Momentum and force components for (a) liquid film control volume and (b) vapor core control volume.....	63
4.3 Effects of interfacial dampening term on (a) eddy momentum diffusivity, (b) velocity, and (c) temperature distributions across condensing FC-72 film for $G = 367 \text{ kg/m}^2 \text{ s}$, and $\dot{m}_w = 6 \text{ g/s}$	72
4.4 Effects of interfacial dampening term on variations of (a) liquid film thickness, and (b) local heat transfer coefficient with quality for $G = 367 \text{ kg/m}^2 \text{ s}$ and $\dot{m}_w = 6 \text{ g/s}$	73
4.5 Variations of (a) liquid film Reynolds number, (b) vapor core Reynolds number, (c) interfacial shear stress, (d) liquid film thickness, and (e) local heat transfer coefficient with quality for different FC-72 mass velocities and $\dot{m}_w = 6 \text{ g/s}$	75
4.6 (a) Variations of predicted and measured total pressure drops with water mass flow rate for different FC-72 mass velocities. (b) Comparison of measured FC-72 total pressure drop data with predictions of present model and previous correlations	78
4.7 (a) Variations of predicted and measured average heat transfer coefficients with water mass flow rate for different FC-72 mass velocities. (b) Comparison of measured FC-72 average condensation heat transfer coefficient data with predictions of present annular model and previous annular condensation heat transfer correlations	79
4.8 Comparison of measured FC-72 local heat transfer coefficient data with predictions of present model and previous annular condensation heat transfer correlations for $\dot{m}_w = 6 \text{ g/s}$ with (a) $G = 248 \text{ kg/m}^2 \text{ s}$, (b) $G = 306 \text{ kg/m}^2 \text{ s}$, and (c) $G = 367 \text{ kg/m}^2 \text{ s}$	80

NOMENCLATURE

A	area
$A_{f,*}$	flow area of liquid control volume
A^+	constant in Eq. (4.30)
Bo	Bond number, $Bo = g(\rho_f - \rho_g)(D_h/2)^2/\sigma$
C	parameter in empirical correlations
C_c	contraction coefficient
c_p	specific heat at constant pressure
D	tube diameter
D_h	hydraulic diameter
F	function
f	Fanning friction factor
f_{app}	apparent friction factor
G	mass velocity
g	gravitational acceleration
H_b	distance between copper block's thermocouple planes
H_{ch}	micro-channel height
H_p	plenum height
H_t	distance between top thermocouple plane and base of micro-channels
h	enthalpy; heat transfer coefficient
h_{fg}	latent heat of vaporization
J	superficial velocity
K	Von-Karman constant
k	thermal conductivity

L	length; length of micro-channel
l^+	turbulent mixing length
M	number of data points
MAE	mean absolute error
m	fin parameter
\dot{m}	mass flow rate
N	number of micro-channels in test section
n	turbulence dampening exponent
Nu	Nusselt number
P	pressure
P_{crit}	critical pressure
P_f	perimeter
P_R	reduced pressure, $P_R = P/P_{crit}$
Pr	Prandtl number
Pr_T	turbulent Prandtl number
ΔP	pressure drop
q''	heat flux at distance y from micro-channel wall
q''_{base}	heat flux based on total base area of micro-channel condenser
q''_w	heat flux based on micro-channel's cooled perimeter
Re	Reynolds number
Su_g	Suratman number, $Su_g = \rho_g \sigma D / \mu_g^2$
T	temperature
T_b	temperature in bottom thermocouple plane in copper block
T_f	fluid temperature
T_{sat}	fluid saturation temperature
T_t	temperature in top thermocouple plane in copper block
$T_{w,b}$	bottom-wall temperature of micro-channel
T^+	dimensionless temperature
T_δ^+	dimensionless boundary layer temperature
u	velocity

u^+	dimensionless velocity
u^*	friction velocity
ν	specific volume
W_{ch}	micro-channel width
W_p	plenum width
W_s	width of solid wall separating micro-channels
We	Weber number
We^*	modified Weber number
X	Martinelli parameter, $X = \sqrt{(dP/dz)_f / (dP/dz)_g}$
x	quality
y	distance perpendicular to channel wall
y^+	dimensionless distance, $y u^* / \nu_f$
z	stream-wise distance

Greek Symbols

α	void fraction
β	channel aspect ratio, $\beta = W_{ch} / H_{ch}$
δ	thickness of condensing film
δ^+	dimensionless thickness, $\delta^+ = \delta u^* / \nu_f$; but in Eqs. (3.7) and (3.8), $\delta^+ = \delta / (D_h / 2)$
ε_h	eddy heat diffusivity
ε_m	eddy momentum diffusivity
ϕ	two-phase pressure drop multiplier
Γ_{fg}	rate of mass transfer due to condensation
η	fin efficiency
μ	dynamic viscosity
ν	kinematic viscosity
ρ	density
$\bar{\rho}$	mixture density

σ	surface tension
σ_c	area ratio, $\sigma_c = (W_{ch}H_{ch}N)/(W_pH_p)$
τ	shear stress
τ_w	wall shear stress
τ_i^*	dimensionless interfacial shear stress

Subscripts

<i>3</i>	based on three-sided heat transfer in rectangular channel
<i>4</i>	based on four-sided heat transfer in rectangular channel
<i>A</i>	accelerational
<i>c</i>	contraction; vapor core
<i>cir</i>	based on uniform circumferential cooling
<i>d</i>	developing region
<i>e</i>	expansion
<i>exp</i>	experimental (measured)
<i>F</i>	frictional
<i>f</i>	fully developed region; saturated liquid; liquid film
<i>fo</i>	liquid only
<i>g</i>	saturated vapor; vapor core
<i>go</i>	vapor only
<i>i</i>	interfacial
<i>in</i>	micro-channel inlet
<i>out</i>	micro-channel outlet
<i>pred</i>	predicted
<i>s</i>	solid copper wall
<i>sat</i>	saturation
<i>sp</i>	single-phase
<i>tot</i>	total
<i>tp</i>	two-phase
<i>tr</i>	transition for laminar to turbulent flow

<i>tt</i>	turbulent liquid-turbulent vapor
<i>tv</i>	turbulent liquid-laminar vapor
<i>vt</i>	laminar liquid-turbulent vapor
<i>vv</i>	laminar liquid-laminar vapor
<i>w</i>	wall; water

ABSTRACT

Experiments were performed to investigate condensation of FC-72 along parallel, square micro-channels with a hydraulic diameter of 1 mm and a length of 29.9 cm, which were formed in the top surface of a solid copper plate. The condensation was achieved by rejecting heat to a counter flow of water through channels brazed to the underside of the copper plate. The FC-72 entered the micro-channels slightly superheated, and operating conditions included FC-72 mass velocities of 68 - 367 kg/m²s, FC-72 saturation temperatures of 57.2 - 62.3°C, and water mass flow rates of 3 - 6 g/s. Using high-speed video imaging and photomicrographic techniques, five distinct flow regimes were identified: smooth-annular, wavy-annular, transition, slug, and bubbly, with the smooth-annular and wavy-annular regimes being most prevalent.

A detailed pressure model is presented which includes all components of pressure drop across the micro-channel. Different sub-models for the frictional and accelerational pressure gradients are examined using the homogenous equilibrium model (with different two-phase friction factor relations) as well as previous macro-channel and mini/micro-channel separated flow correlations. Unexpectedly, the homogenous flow model provided far more accurate predictions of pressure drop than the separated flow models. Among the separated flow models, better predictions were achieved with those for adiabatic and mini/micro-channels than those for flow boiling and macro-channels.

The FC-72 condensation heat transfer coefficient was highest near the channel inlet, where the annular liquid film is thinnest. The heat transfer coefficient decreased along the micro-channel because of the film thickening and eventual collapse of the annular regime. Notable heat transfer enhancement was observed for annular flow regions of the micro-channel associated with interfacial waves. Comparing the present data to predictions of previous annular condensation heat transfer correlations shows correlations intended for macro-channels generally provide better predictions than correlations intended specifically for mini/micro-channels. A new condensation heat transfer coefficient correlation is proposed for annular condensation heat transfer in

mini/micro-channels. The new correlation shows excellent predictive capability based on both the present FC-72 data and a large database for mini/micro-channel flows amassed from eight previous sources.

A theoretical control-volume-based model is proposed based on the assumptions of smooth interface between the annular liquid film and vapor core, and uniform film thickness around the channel's circumference. Mass and momentum conservation are applied to control volumes encompassing the liquid film and the vapor core separately. The model accounts for interfacial suppression of turbulent eddies due to surface tension with the aid of a new eddy diffusivity model specifically tailored to shear-driven turbulent films. The model predictions are compared with present experimental pressure drop and heat transfer data for annular condensation of FC-72 mass velocities of 248 - 367 kg/m²s, saturation temperatures of 57.8 - 62.3°C, qualities of 0.23 – 1.0, and water mass flow rates of 3 - 6 g/s. The data are also compared to predictions of previous separated flow mini/micro-channel and macro-channel correlations. While some of the previous correlations do provide good predictions of the average heat transfer coefficient, they fail to capture axial variation of the local heat transfer coefficient along the channel. The new model accurately captures the pressure drop and heat transfer coefficient data in both magnitude and trend, evidenced by mean absolute error values of 3.6% and 9.3%, respectively.

CHAPTER 1. INTRODUCTION

1.1. Motivation for Study

Developments in many cutting-edge technologies are becoming increasingly dependent upon the ability to dissipate large amounts of heat from small surface areas. Examples include high performance computers, hybrid vehicle power electronics, lasers, radars and avionics. Although single-phase cooling systems have been successfully implemented in the past, the fast increase in power density in these technologies is pushing single-phase systems into uncharted territory in terms coolant flow rate and pressure drop, let alone the need to greatly increase heat transfer area. Even with these provisions, cooling goals in many applications are becoming virtually impossible to achieve with single-phase systems. Because of these inherent limitations, focus has shifted in recent years in favor of two-phase cooling schemes.

Modern technologies are demanding more effective schemes to tackle heat removal from very high power density devices. Most of the phase-change electronic cooling research published during the past three decades has been focused on removing heat from the electronic device using micro-channel heat sinks, jet-impingement or sprays (Mudawar and Wadsworth, 1991; Jiang *et al.*, 2001; Kawahara *et al.* 2002; Lin and Ponnappan, 2003; Lee and Mudawar, 2005). Far less emphasis has been placed on high-flux heat rejection from the two-phase cooling system. A key reason behind this trend is a common perception that a commercial condenser can always be found to reject the heat from virtually any phase-change cooling system. However, recent studies concerning very high power density defense electronics have shown that substantial enhancement in heat dissipation from the device can be achieved by using a two-loop cooling system (Lee and Mudawar, 2008a, 2008b). Here, a primary cooling loop is used to extract the heat from the device by highly subcooled flow boiling, and the heat is rejected via a high performance heat exchanger to a separate low-temperature refrigeration loop. Compact and lightweight system design requires that the intermediate condenser achieve heat fluxes comparable to those of the flow boiling module.

1.2. Miniature Condenser for High-Flux Heat Rejection

The superior cooling performance of two-phase cooling systems is realized by the enormous boiling and condensation heat transfer coefficients associated with heat acquisition from the heat-dissipating device and heat rejection, respectively. The quest for compact and lightweight packaging favors the use of miniature boiler designs, such as micro-channel heat sinks (Lee and Mudawar, 2008a, 2008b) or jet-impingement (Mudawar and Wadsworth, 1991). While many present two-phase cooling systems employ fairly standard air-cooled condensers to reject the heat to the ambient, there is now a growing need for miniature condensers that can reject the heat by condensing a primary coolant in a compact primary cooling loop. The heat is transferred to a secondary liquid coolant and transported to a remote heat exchanger where is ultimately rejected to ambient air (or seawater for marine applications). As described by Lee and Mudawar (2008a, 2008b), the secondary cooling loop could consist of a low-temperature refrigeration cycle. Using separate cooling loops decouples the performance of the boiler from that of the refrigeration cycle, enabling the dissipation of much higher device heat fluxes than with an evaporator incorporated directly in the refrigeration loop. Integrating miniature boilers and condensers in the compact primary cooling loop will necessitate greatly enhancing the condenser's performance to a level commensurate with that of the boiler. This goal can be realized with a condenser containing parallel micro-channels similar to those utilized in micro-channel flow boiling heat sinks. However, special care must be exercised to achieve the thermal goals without compromising the system's efficiency by the increased pressure drop.

Because condensation heat transfer coefficients are typically much smaller than those realized with subcooled flow boiling, commercial condensers are often far too large to meet the size and packaging constraints of defense electronics. The present study concerns the design of a relatively new class of condensers that employ a series of micro-channels to meet the stringent size and weight requirements of defense electronics. Another goal is to maintain mostly annular flow along the micro-channels to capitalize upon the large condensation heat transfer coefficients associated with thin films. With superheated or saturated inlet conditions, a very thin film is initiated in the upstream region of the channel, which is driven along the channel by the shear stresses exerted by the core vapor flow. Micro-channels greatly increase vapor velocity and therefore the

shear stress exerted upon the film interface. This greatly decreases the film thickness, resulting in very high condensation heat transfer coefficients. However, the film thickness increases along the micro-channel as an increasing fraction of the vapor flow condenses into liquid. Eventually, the annular regime collapses and is replaced by a succession of thermally less efficient slug, bubbly, and liquid flow regimes. While micro-channels do enhance heat transfer performance, they also increase pressure drop. Therefore, the design of micro-channel condensers requires predictive tools for both pressure drop and condensation heat transfer coefficient.

1.3. Transport Phenomena in Micro-Channel Condenser

Two-phase pressure drop is comprised of frictional as well as accelerational or decelerational components; acceleration is associated with boiling flows and deceleration condensing flows. In high-flux micro-channel boiling flows, acceleration contributes a large fraction of the total pressure drop and, therefore, pumping power. However, in high-flux micro-channel condensing flows, deceleration provides the benefit of decreasing the pressure drop.

Another factor that influences pressure drop in condensing flows is two-phase flow regime. Condensing flow regimes in a tube can generally be classified into pure vapor, annular, slug, bubbly and pure liquid. The annular flow regime is the most crucial for condenser design since, for most practical designs, it prevails over the largest fraction of the tube length and provides very high heat transfer rates. The annular flow regime commences upstream in the tube once vapor begins to condense into a liquid film along the tube wall. This film is typically very thin and associated with a small thermal resistance between the vapor and the wall, resulting in very high heat transfer coefficients compared to the other flow regimes. As more of the vapor is condensed into liquid, the annular structure collapses and the slug and bubbly regimes are formed in succession.

Key to achieving high condensation heat transfer coefficients is to maintain annular flow over a large fraction of the micro-channel's length. This flow regime consists of a liquid film that sheathes the channel walls, driven by the shear force exerted by the vapor core. The film is extremely thin in the upstream region of the micro-channel where the annular regime is initiated, which yields very high condensation heat transfer coefficients. The heat transfer coefficient decreases along the stream-wise direction as the annular film gradually thickens and, especially, as the annular regime is replaced, in

succession, by transition, slug, bubbly and single-phase liquid flow regimes. Recognizing the importance of annular flow, previous condensation studies have focused mostly on this particular regime (*e.g.*, Akers *et al.*, 1958; Cavallini and Zecchin, 1974; Shah, 1979; Dobson and Chato, 1998; Moser *et al.*, 1998; Want *et al.*, 2002; Koyama *et al.*, 2003; Huang *et al.*, 2010).

The pursuit of compact condenser design is evident from several recent articles concerning multi-port micro-channel condensers (Yang and Webb, 1996; Yan and Lin, 1999; Wang *et al.*, 2002; Koyama *et al.*, 2003; Park and Hrnjak, 2009). Koyama *et al.* (2003) examined the performance of a condenser having rectangular micro-channels with a hydraulic diameter of 0.81 mm using R134a as working fluid. The highest heat transfer coefficient, on the order of 10^4 W/m²K, was achieved in the high quality region with a relatively high mass velocity of $G = 652$ kg/m²s. Recently, Park and Hrnjak (2009) examined the condensation of CO₂ in 0.89-mm circular parallel micro-channels and achieved maximum heat transfer coefficients on the same order as Koyama *et al.* with $G = 600$ kg/m²s.

While past studies have provided valuable databases for condensation in micro-channels, there is a general lack of fundamental understanding of interfacial behavior and shortage of predictive tools for both pressure drop and heat transfer coefficient. On the fundamental side, two key phenomena that are of great interest to modeling condensation in micro-channels are interfacial waves and turbulence in the annular liquid film. Past studies involving adiabatic, heated and evaporating liquid films have shown interfacial waves can greatly influence mass, momentum and heat transfer in the film (Lyu and Mudawar, 1991a, 1991b; Mudawar and Houpt, 1993a, 1993b; Shmerler and Mudawar, 1998a, 1998b). Surface tension at the vapor-liquid interface has been shown by Mudawar and El-Masri (1986) to cause significant dampening of turbulent fluctuations in films, which can have a profound influence on heat transfer across the film. Aside from these fundamental issues, there is also a need for reliable correlations for condensing micro-channel flows. These issues and needs are the primary motivation for the present study.

1.4. Two-Phase Flow Model for Annular Flow Condensation

The vast majority of published studies addressing the prediction of pressure drop and condensation heat transfer coefficient for annular flows are based on semi-empirical

separated flow correlations (mostly Lockhart-Martinelli-type, 1949) and empirical heat transfer correlations (*e.g.*, Shah, 1979), respectively. Like all correlations, these predictive tools are valid only for the range of operating conditions of databases these correlations are based upon. This limitation has created a need for development of theoretical models that possess a broader application range. Theoretical control-volume-based models have been quite effective in predicting both pressure drop (Qu and Mudawar, 2003a) and heat transfer (Qu and Mudawar, 2003c) in saturated flow boiling in micro-channel heat sinks, subcooled flow boiling pressure drop in micro-channel heat sinks (Lee and Mudawar, 2009), and flow boiling critical heat flux (Sturgis and Mudawar, 1999). Nonetheless, several fundamental challenges remain when attempting to develop an accurate model for annular two-phase flow. These include interfacial instabilities, interfacial mass, momentum and heat transfer, and turbulence within the annular film.

One source of difficulty in modeling annular two-phase flow is interfacial waves (Hubbard *et al.*, 1976; Ueda *et al.*, 1977; Shmerler and Mudawar, 1988a, 1988b; Koskie *et al.*, 1989; Lyu and Mudawar, 1991a; Mudawar and Houpt, 1993b). These are highly complex phenomena and no effective method has been developed for their characterization. One type of waves is ripples, which are characterized by both small amplitude and small wavelength and do not contribute substantially to liquid film mass transport. Large waves can also develop, where the perturbed liquid film is replaced by lumps of liquid that are separated by a thin layer of liquid. Due to their appreciable protrusion into the vapor flow, the motion of large waves can be dominated more by vapor drag forces than by interfacial vapor shear. Modeling large waves is complicated by the fact that they are highly nonlinear forms of instability that greatly complicate the effectiveness of averaging methods to predict the liquid film's momentum or heat transfer transport behavior. Despite extensive efforts to assess the influence of interfacial waves on mass, momentum and heat transfer, no systematic tools have been developed to effectively model this influence.

Two other phenomena that complicate the development of accurate annular flow models are droplet entrainment and droplet deposition. These two phenomena are closely related to interfacial waviness. Entrainment refers to tiny liquid droplets that break off the crests of waves and are driven along with the vapor core. Deposition refers to droplets from the vapor core falling back upon the film interface. In their study of annular film evaporation, Qu and Mudawar (2003a) proved that droplet entrainment and deposition play a very important role in micro-channels compared to macro-channels.

Another challenge in modeling annular flows is accurate prediction of turbulent or eddy diffusivity within the annular liquid film. Classical turbulence models are known to break apart when dealing with fluid regions near a vapor-liquid interface (Hubbard *et al.*, 1976; Ueda *et al.*, 1977; Mudawar and El-Masri, 1986). As discussed by Mudawar and El-Masri, surface tension forces along the interface can significantly dampen turbulent eddies, resulting in appreciable resistance to heat transfer near the interface. Ignoring this effect could result in appreciable error in predicting the condensation heat transfer coefficient.

1.5. Research Objectives

This study examines the two-phase flow regimes, pressure drop and heat transfer associated with condensation of FC-72 along parallel micro-channels with a hydraulic diameter of 1 mm (Kim *et al.*, in review; Kim and Mudawar, in review-a). The construction of the condensation module, two-phase condensation loop and experimental methods used will be described. Using high-speed video imaging and photomicrographic techniques, five distinct flow regimes were identified: smooth-annular, wavy-annular, transition, slug, and bubbly, with the smooth-annular and wavy-annular regimes being most prevalent, which are compared to those from previous studies. The FC-72 pressure drop data are compared with the predictions of prior two-phase homogenous (Bottomley, 1936; Lewis and Robertson, 1940; Benjamin and Miller, 1942; Markson *et al.*, 1942; McAdams *et al.*, 1942; Allen, 1951; Akers *et al.*, 1958; Cicchitti *et al.*, 1960; Owens, 1961; Dukler *et al.*, 1964; Beattie and Whalley, 1982; Lin *et al.*, 1991) and separated flow models (Lockhart and Martinelli, 1949; Friedel, 1979; Chisholm, 1983; Muller-Steinhagen and Heck, 1986; Jung and Radermacher, 1989; Mishima and Hibiki, 1996; Wang *et al.*, 1997; Tran *et al.*, 2000; Chen *et al.*, 2001; Lee and Lee, 2001; Zhang and Webb, 2001; Cavallini *et al.*, 2002; Yu *et al.*, 2002; Lee and Mudawar, 2005; Nino *et al.*, 2005; Hwang and Kim, 2006) to identify most suitable models for micro-channel condensing flows. The present FC-72 heat transfer data are first compared with predictions of several previous correlations for both macro-channels (Akers *et al.*, 1958; Cavallini and Zecchin, 1974; Shah, 1979; Dobson and Chato, 1998; Moser and Webb, 1998) and mini/micro-channels (Wang *et al.*, 2002; Koyama *et al.*, 2003; Huang *et al.*, 2010). A new correlation for annular condensation heat transfer is proposed, which is validated against the present data in addition to a database for condensation in

mini/micro-channels from eight previous sources (Hirofumi and Webb, 1995; Zhang, 1998; Yan and Lin, 1999; Wang *et al.*, 2002; Cavallini *et al.*, 2005; Matkovic *et al.*, 2009; Park and Hrnjak, 2009; Huang *et al.*, 2010).

Another goal of the present study is to develop a theoretical control-volume-based model for annular condensing micro-channel flows (Kim and Mudawar, in review-b). Addressed in the development of this new model are the effects of droplet entrainment and deposition, interfacial instabilities, and dampening of liquid film turbulence near the liquid-vapor interface. The model's predictive accuracy is assessed against the FC-72 pressure drop and heat transfer data measured previously by the authors (Kim *et al.*, in review; Kim and Mudawar, in review-a), and compared to those of prior annular condensation correlations.

Another goal is to extend both the theoretical models and correlation approaches to flow boiling in micro-channels.

CHAPTER 2. EXPERIMENTAL METHODS

2.1. Condensation Flow Loop

Figure 2.1 shows a schematic of the two-phase experimental apparatus constructed for this study. It uses two sub-loops, one for FC-72, the primary coolant, and the second for the cooling water. A 3M-company Fluorinert electronic liquid, FC-72 has excellent dielectric properties, a relatively moderate boiling point of 56°C at 1 bar, and a surface tension much smaller than that of water, 0.0084 compared to 0.059 N/m at 1 bar. Table 2.1 provides a summary of the thermophysical properties of FC-72 at $T_{sat} = 60^\circ\text{C}$, which the saturation temperature corresponding an operating pressure close to that used in the present experiments.

The FC-72 is circulated through the primary loop with the aid of a gear pump. The fluid passes through a set of flow meters followed by an in-line electric heater, which is powered by a variable voltage transformer, before entering the micro-channel condensation module. Both temperature and pressure are measured in the inlet plenum of condensation module to determine fluid quality, which can be regulated to the desired value with the aid of a variable voltage transformer that powers the in-line heater upstream. The FC-72 condenses along the condensation module by rejecting heat to the waterside. The FC-72 temperature and pressure are measured once more at the condensation module's outlet plenum. Exiting the condenser module, the FC-72 is passed through a plate-type heat exchanger to condense any remaining vapor and achieve the desired temperature as the FC-72 returns to the primary loop's reservoir.

Table 2.1 Thermophysical properties of FC-72 at $T_{sat} = 60^\circ\text{C}$.

h_{fg}	ρ_f	ρ_g	μ_f	k_f	$c_{p,f}$	σ
kJ/kg	kg/m ³	kg/m ³	kg/m·s	W/m·K	kJ/kg·K	mN/m
93.7	1583.4	14.90	4.18×10^{-4}	0.0534	1.1072	8.0

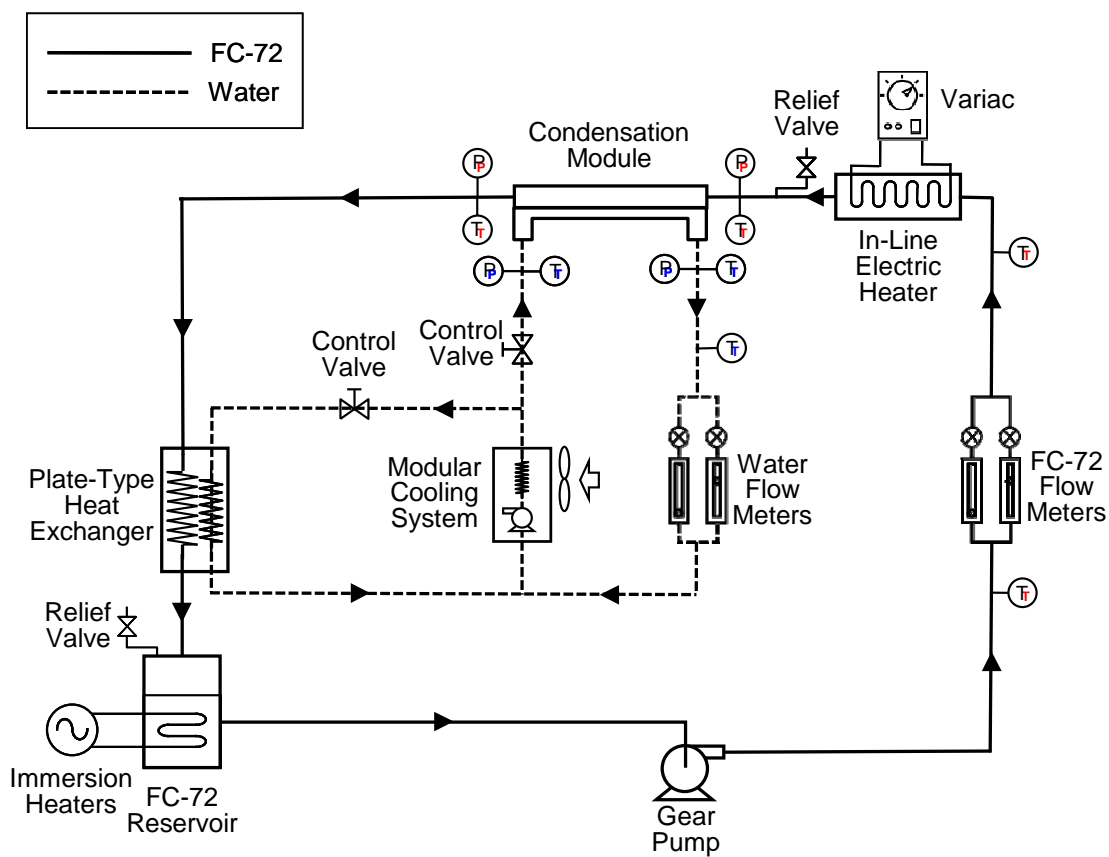


Figure 2.1 Schematic diagram of test loop.

In the condensation module, water travels in a counter-flow direction to that of the FC-72. The water enters the condensation module at near room temperature and warms up by capturing heat from the condensing FC-72 flow. The warm water flows through a Lytron modular cooling system, where it cools back to near room temperature. The water flow exiting the Lytron cooling system is divided into two parts, one flows back to the condensation module and the second to the plate-type heat exchanger. Figure 2.2(a) and 2.2(b) show, respectively, a photo of the micro-channel condensation module and another of the main part of the experimental set-up.

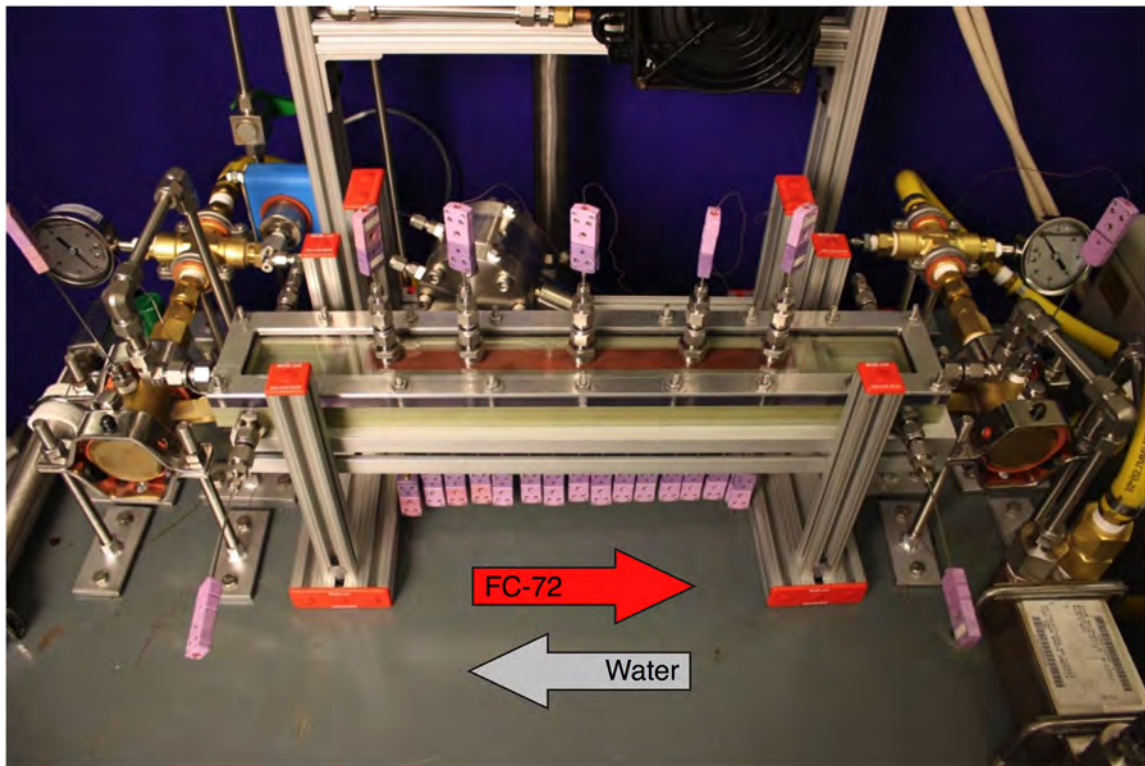
2.2. Micro-Channel Condensation Module

Figures 2.3(a) and 2.3(b) show the construction of micro-channel condensation module. The module consists of a cover plate, housing, condensation copper block, and water channels. The cover plate, which seals the tops of the square micro-channels, is made from transparent polycarbonate (Lexan) to facilitate photographic study of the condensing flow. The top of the oxygen-free copper block is 2-cm wide by 29.9-cm long, and contains ten of $1 \times 1 \text{ mm}^2$ square micro-channels. Soldered to the underside of the copper block are three of $3.8 \times 3.8 \text{ mm}^2$ brass tubes, which carry the counter flow of cooling water. Sixteen pairs of type-E thermocouples, which are embedded in the copper block beneath the micro-channels, run down the length of the copper block at 19 mm intervals. Using the assumption of one-dimensional heat conduction between the two thermocouple planes, both the heat flux and surface temperature at the base of the micro-channels may be determined along the stream-wise direction (Kim and Mudawar, 2010a). The dimensions of the test section are provided in Table 2.2.

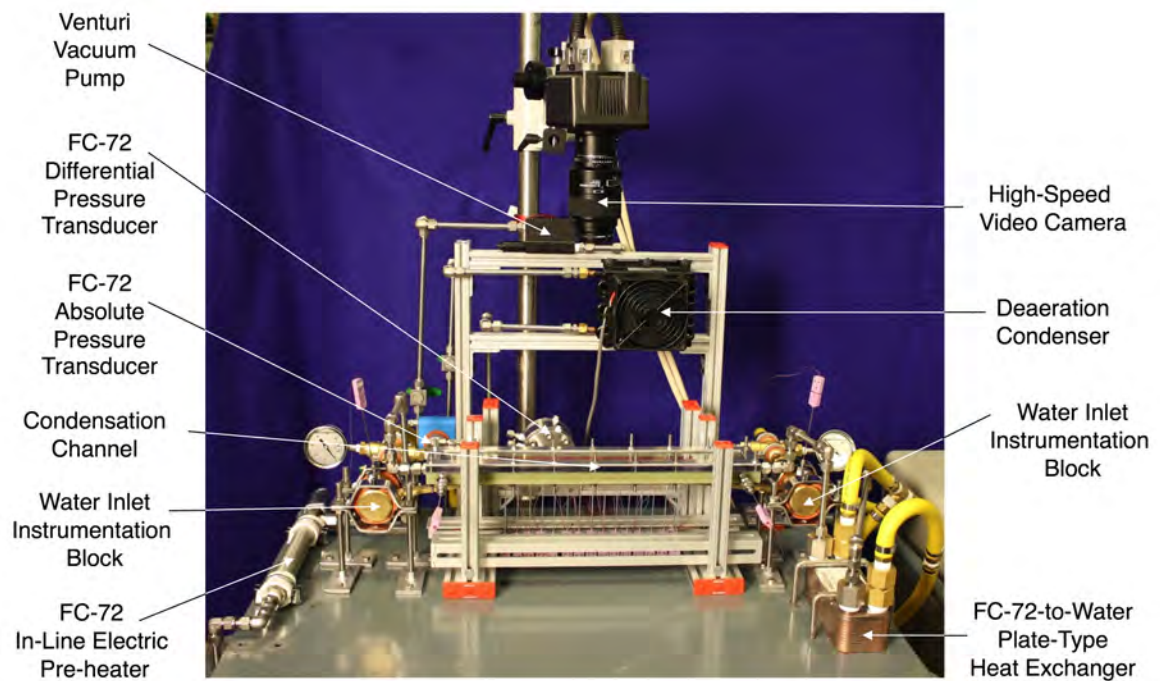
The copper block is inserted into an insulating G-10 housing that features FC-72 inlet and outlet ports, micro-channel inlet and outlet plenums, and pressure and temperature measurement ports. The G-10 housing and water channels are covered by insulating layers of fiberglass.

Table 2.2 Test section dimensions.

W_{ch}	H_{ch}	W_s	H_t	H_b	L	N
mm	mm	mm	mm	mm	cm	-
1.0	1.0	1.0	9.65	7.62	29.9	10



(a)



(b)

Figure 2.2 Photos of (a) micro-channel condensation module and (b) main part of test setup.

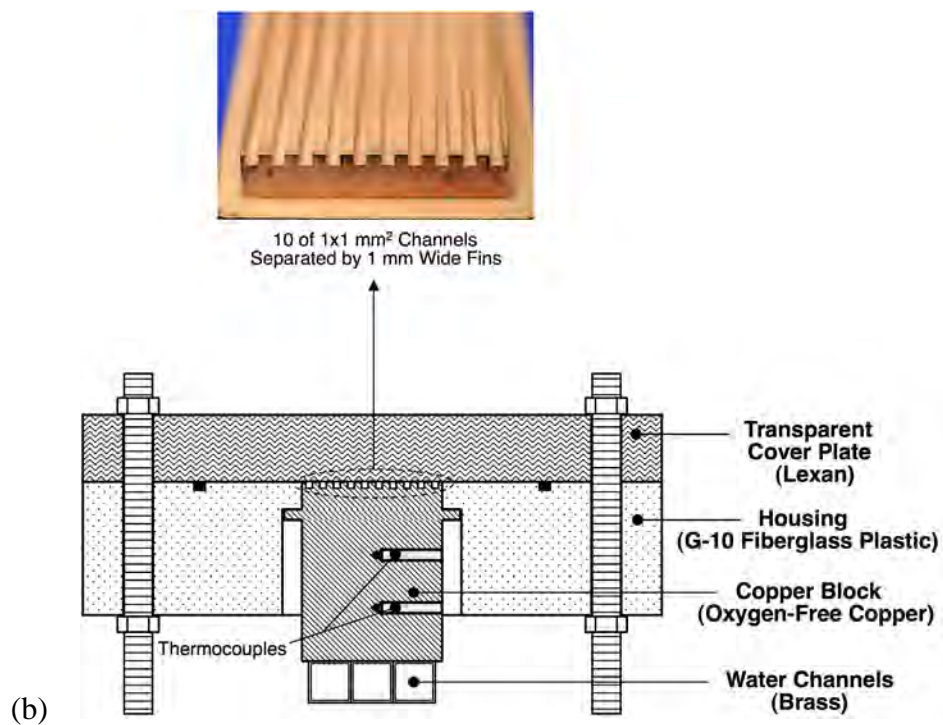
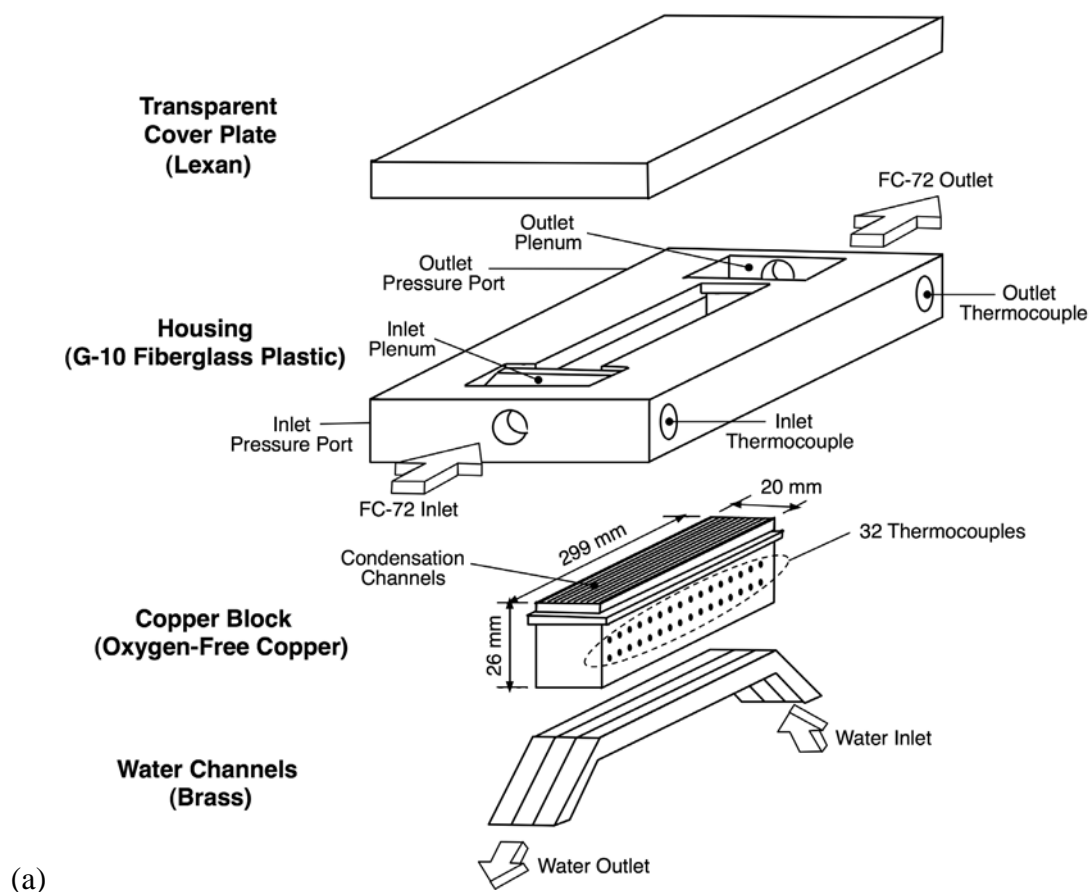


Figure 2.3 (a) Construction and (b) cross-sectional view of micro-channel condensation module.

2.3. Operating Conditions and Measurement Accuracy

Experiments were performed to examine flow regimes and measure pressure drop and heat transfer coefficients corresponding to different flow rates of FC-72 and cooling water. The test matrix for the study consisted of 24 tests covering six FC-72 flow rates ($G = 68, 118, 186, 248, 306, \text{ and } 367 \text{ kg/m}^2\text{s}$) and four water flow rates ($\dot{m}_w = 3, 4, 5, \text{ and } 6 \text{ g/s}$).

Since the focus of this study is high-flux condensation, operating conditions were set to achieve mostly annular flow near the inlet of the micro-channels. Therefore, the FC-72 was introduced into the condensation module in pure vapor state with a quality of 1.11 - 1.17 for low FC-72 flow rates ($G = 68 - 186 \text{ kg/m}^2\text{s}$) and 1.08 - 1.10 for high FC-72 flow rates ($G = 248 - 367 \text{ kg/m}^2\text{s}$). These conditions resulted in an upstream single-phase superheated vapor region 1.1 - 3.1 cm long (4 - 10% of the total channel length) for the low FC-72 flow rate range, and 2.7 - 5.8 cm long (9 - 19% of the total channel length) for the high FC-72 flow rate range. The inlet plenum pressure ranged from 1.040 - 1.324 bar. Operating conditions along the channel length were as follows: saturation temperatures of $T_{sat} = 57.2 - 62.3^\circ\text{C}$, qualities of $x = 0 - 1.17$, and heat fluxes of $q_w'' = 0.43 - 3.21 \text{ W/cm}^2$.

There are several techniques for measuring liquid film thickness in two-phase applications (Koskie *et al.*, 1989; Lyu and Mudawar, 1991a, 1991b). Unfortunately, small channel size precludes the use of these techniques in the present application, causing a reliance on photographic methods instead. High-speed video imaging played a crucial role in capturing two-phase condensation flow regimes. Two key requirements for capturing the complex interfacial features in the micro-channels with high resolution are high shutter speed and high magnification. These goals were achieved with a Photron FASTCAM-Ultima camera capable of shutter speeds up to $1/120,000 \text{ s}$, which was used in conjunction with an assortment of Infinity K-2 lenses.

FC-72 pressure was measured in the inlet plenum with the aide of an absolute pressure transducer, while a differential pressure transducer measured pressure drop between the inlet and outlet plenums. Temperatures in the inlet and outlet plenums, copper block, and water channels were measured and processed by an HP-3852A data acquisition system. All measurements were made after all the system pressures and temperatures reached steady state.

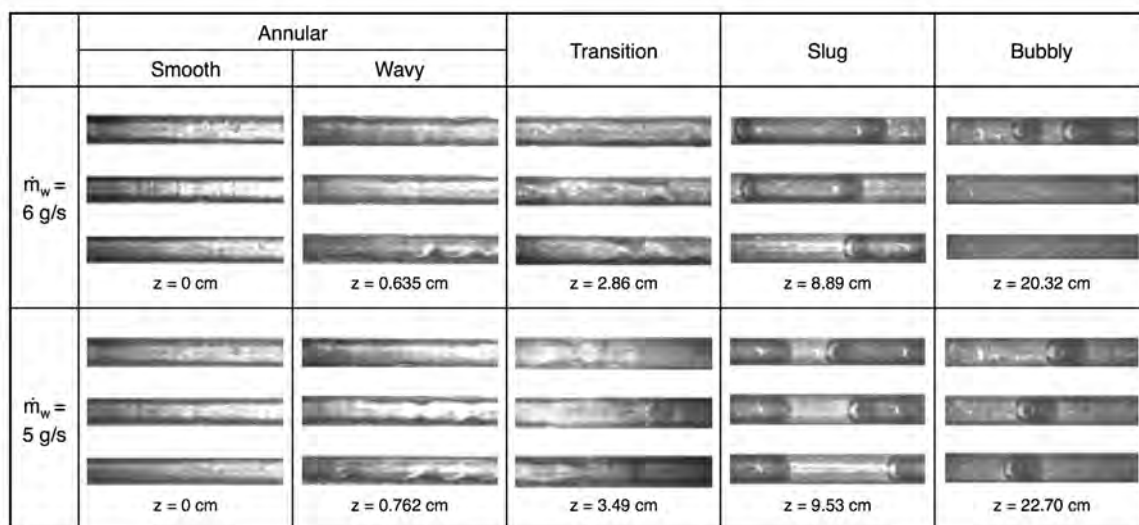
By using five thermocouple ports attached on top of the cover plate, heat loss through the cover plate is estimated at less than 2% of the heat input through the base of the micro-channels, which is calculated using the assumption of one-dimensional heat conduction between the two thermocouple planes (Kim and Mudawar, 2010a). All pressure transducers used in this study featured an accuracy of 0.05%. The rotameters had a flow rate accuracy of $\pm 2\%$ of measurement.

CHAPTER 3. EXPERIMENTAL RESULTS

3.1. Flow Visualization Results

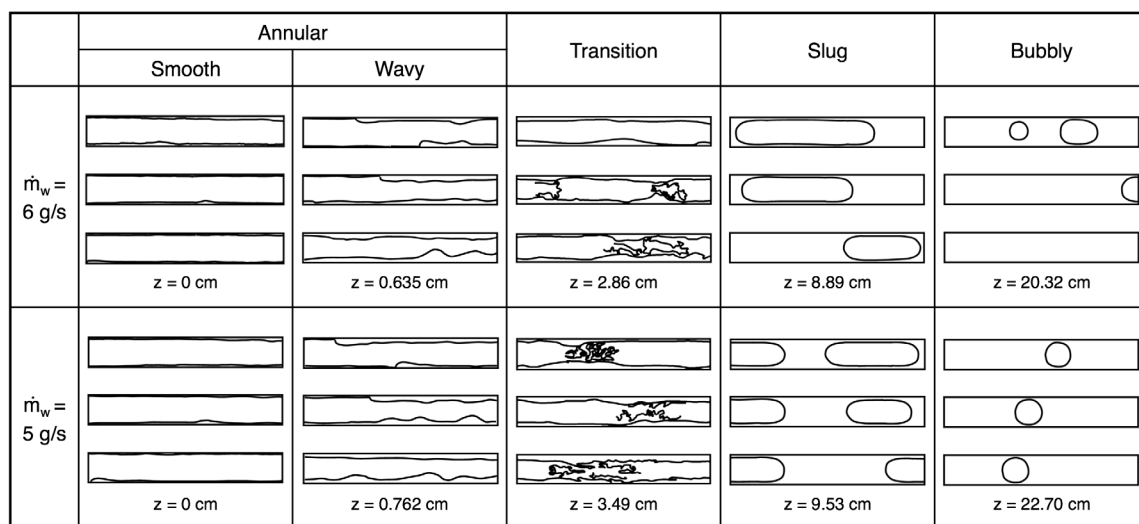
High-speed video imaging and photomicrographic techniques were used to capture dominant condensation flow regimes along the parallel micro-channels. Figure 3.1 depicts representative flow regimes in three adjacent micro-channels channels at different locations from the micro-channel inlet. Five distinct flow regimes were identified. The *smooth-annular* flow regime is characterized by a very thin and fairly smooth liquid film that flows along the channel wall, with vapor flowing in the core clear of any liquid droplets. The film is barely discernible even when using a high magnification lens. This regime occurred in the inlet region of micro-channels under conditions of high inlet quality. The *wavy-annular* regime features a liquid film that is notably thicker than that of the smooth-annular regime, and having discernible interfacial waves. The next *transition* regime is characterized by bridging of liquid ligaments across the vapor core. The *slug* regime features elongated cylindrical bubbles whose length is several times larger than the width of the channel. The *bubbly* regime features spherical bubbles with a diameter approaching the of the micro-channel width. The bubbly regimes was least prevalent, observed only at the lowest tested mass velocity of $G = 68 \text{ kg/m}^2\text{s}$. Notice that no droplets are entrained in the vapor core for the smooth-annular and wavy-annular flows. This is in sharp contrast with annular flow associated with flow boiling in micro-channels. As observed by Qu and Mudawar (2004), liquid droplets entrained in the vapor core have an appreciable influence on pressure drop and heat transfer in micro-channel boiling flows. This fundamental difference between micro-channel flow boiling and condensing flows and its implications to pressure drop prediction will be discussed later.

Figure 3.2(a) shows the observed FC-72 flow regime transition data. Increasing the mass velocity is shown causing the smooth-annular regime, which corresponds to high quality values, to extend further downstream towards lower quality values, while narrowing the slug flow in the low quality region. Although the bubbly regime was



Flow direction

(a)



Flow direction

(b)

Figure 3.1 Representative (a) photographs and (b) schematics of FC-72 condensation flow regimes in three adjacent channels for $G = 68 \text{ kg/m}^2\text{s}$.

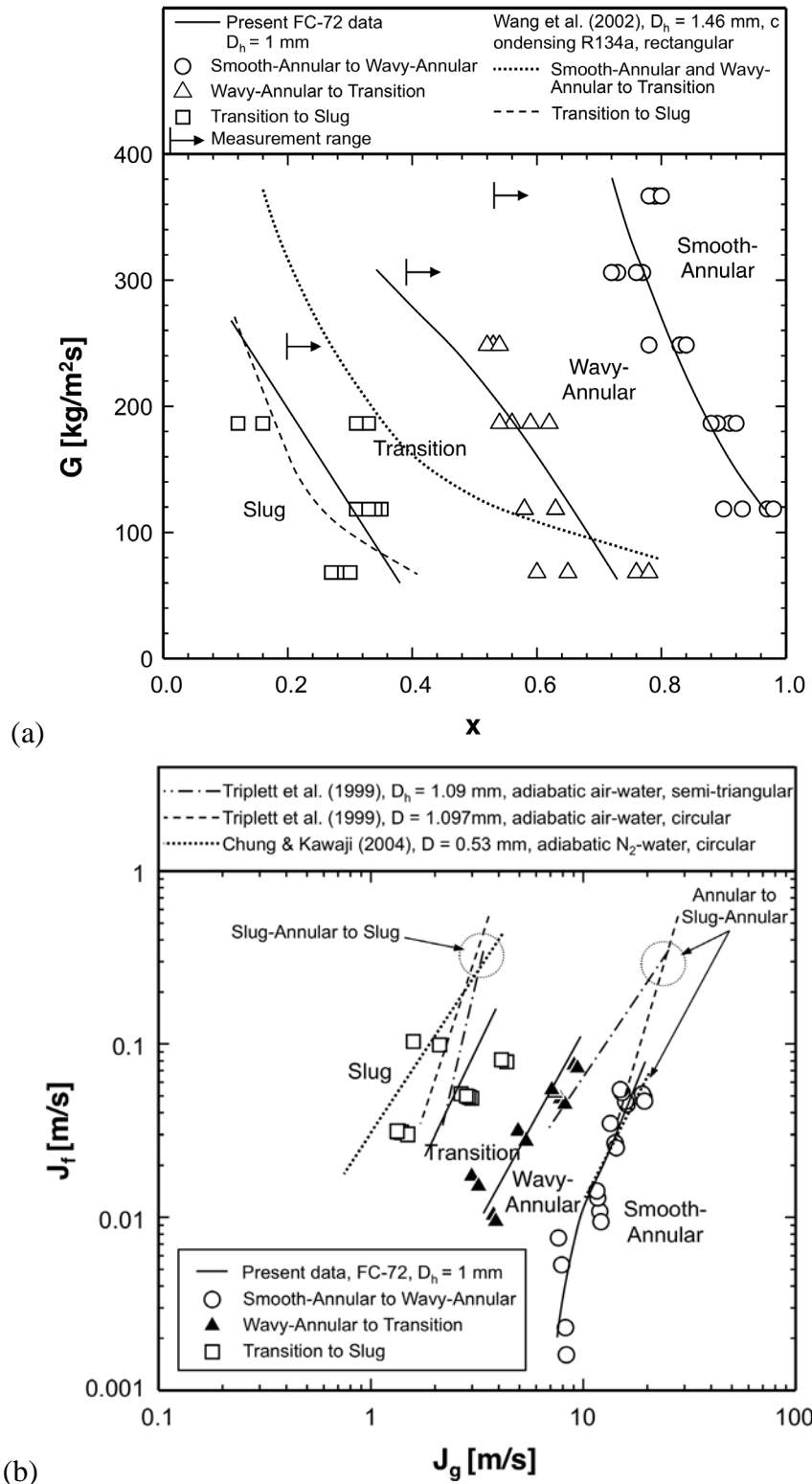


Figure 3.2 Comparison of present FC-72 condensation flow regime data with those of (a) Wang *et al.* (2002) and (b) Triplet *et al.* (1999) and Chung and Kawaji (2004).

observed in the present study for $G = 68 \text{ kg/m}^2\text{s}$, no bubbly regime data are shown in Fig. 3.2(a). This is due to the fact that the bubbly regime was observed for negative values of quality, indicating bubbles persisted in subcooled liquid flow due to thermodynamic non-equilibrium effects. Figure 3.2(a) also compares the present FC-72 flow regime boundary data with flow regime boundary lines from Wang *et al.* (2002) for R134a condensing flow inside a horizontal multi-port condenser featuring rectangular channels with a hydraulic diameter of 1.46 mm. Notice that both the smooth-annular and wavy-annular regimes identified in the present study were designated simply as annular by Wang *et al.*. The boundary between the transition and slug regimes of the present study is in good agreement with that of Wang *et al.*, however, the boundary between the wavy-annular and transition regimes corresponds to higher quality values than observed by Wang *et al.*.

Figure 3.2(b) compares the present FC-72 flow regime transition data with those of Triplett *et al.* (1999) and Chung and Kawaji (2004). Triplett *et al.*'s data are based on air-water adiabatic flow in horizontal semi-triangular and circular micro-channels with hydraulic diameters of 1.09 and 1.097 mm, respectively. Chung and Kawaji conducted their experiments with an adiabatic mixture of nitrogen gas and water inside a 0.53-mm diameter horizontal circular tube. For all cases, the transition line to slug flow is observed when the superficial gas velocity is in a range of 1 to 4 m/s. The transition flow regime of this study was designated as slug-annular by both Triplett *et al.* and Chung and Kawaji, or 'serpentine-like gas core in churn flow' by Chung and Kawaji. The wavy-annular flow regime of this study had a thicker liquid film with waves having larger amplitude and wavelength than those of Triplett *et al.* and Chung and Kawaji, and is similar to the 'gas core with a wavy liquid film' regime designated as churn flow by Chung and Kawaji. Taking into consideration the differences in flow regime designation, the present flow regime boundaries are generally consistent with those from the two earlier studies.

Despite the fair agreement depicted in Figs. 3.2(a) and 3.2(b), it is important to emphasize the fundamental weaknesses of flow regime maps that utilize dimensional plots. The first is that the use of G versus x or J_f versus J_g may imply that such pairs of parameters govern all flow regimes, which is obviously not the case. The second weakness is the fact that flow regime boundaries are dominated by physical mechanisms and corresponding dimensionless groups that vary greatly from one boundary to another.

Figure 3.3 shows an alternative presentation of flow regime boundaries in a dimensionless plot of modified Weber number, We^* , versus the Martinelli parameter, X_{tt} . Using the assumption that the inertia of the vapor phase is the dominant destructive force acting on the liquid film, while surface tension and liquid viscous forces are the stabilizing forces, Soliman (1986) derived the following relations for modified Weber number by balancing the destructive and stabilizing forces.

$$We^* = 2.45 \frac{Re_g^{0.64}}{Su_g^{0.3} (1 + 1.09 X_{tt}^{0.039})^{0.4}} \text{ for } Re_f \leq 1250, \quad (3.1a)$$

$$\text{and } We^* = 0.85 \frac{Re_g^{0.79} X_{tt}^{0.157}}{Su_g^{0.3} (1 + 1.09 X_{tt}^{0.039})^{0.4}} \left[\left(\frac{\mu_g}{\mu_f} \right)^2 \left(\frac{\nu_g}{\nu_f} \right) \right]^{0.084} \text{ for } Re_f > 1250, \quad (3.1b)$$

where the Suratman number, Su_g , and Martinelli parameter (based on turbulent liquid-turbulent vapor) are given by

$$Su_g = \frac{\rho_g \sigma D}{\mu_g^2}, \quad (3.2a)$$

$$\text{and } X_{tt} = \left(\frac{\mu_f}{\mu_g} \right)^{0.1} \left(\frac{1-x}{x} \right)^{0.9} \left(\frac{\nu_f}{\nu_g} \right)^{0.5}, \quad (3.2b)$$

respectively (Soliman, 1986). Based on his own database, Soliman proposed that the flow is always annular for $We^* < 20$ and always mist for $We^* > 30$. While a few of the present smooth-annular flow regime data fall into Soliman's annular-to-mist transition region, most of the present data fall in Soliman's annular regime region. Figure 3.3 also shows boundaries between annular, stratified-wavy, and plug regimes identified by Chen et al. (2006) for condensation of R134a inside horizontal 12 and 14 mm diameter micro-finned tubes. Overall, there is general agreement with the present boundary lines between the wavy-annular and transition regimes, and between the transition and slug regimes.

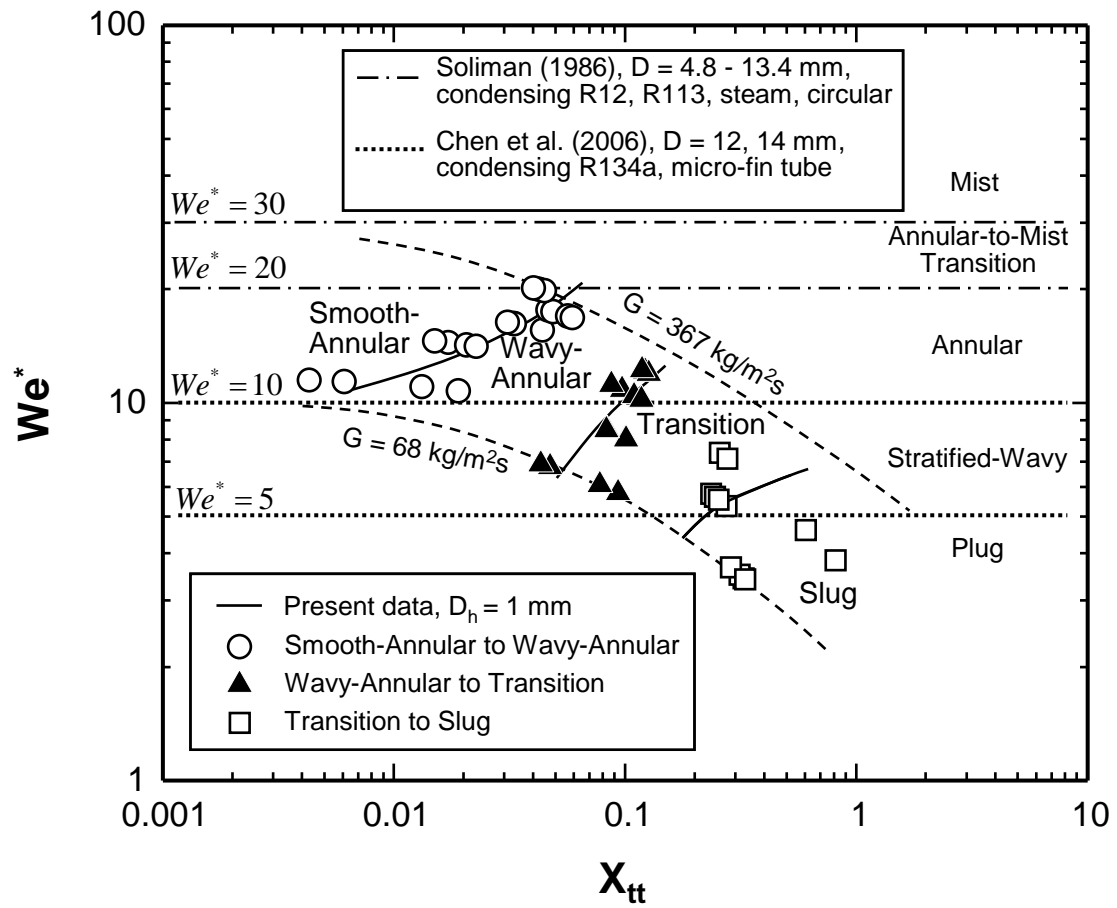


Figure 3.3 Comparison of present FC-72 condensation flow regime boundaries with those of Soliman (1986) and Chen *et al.* (2006).

3.2. Two-Phase Pressure Drop Results

3.2.1. Experimental Results

Figure 3.4 shows the variation of total pressure drop measured between the inlet and outlet plenums of the condensation module with water mass flow rate for different FC-72 mass velocities. Increasing the mass velocity of FC-72 increases the interfacial shear stress between the vapor core and liquid film due to the increasing vapor core velocity, which results in the measured increase in pressure drop. Figure 3.4 shows the total pressure drop decreases slightly with increasing water mass flow rate. This trend can be explained by the higher water flow rate increasing the wall heat flux, which hastens the flow deceleration leading to diminished interfacial shear.

3.2.2. Pressure Drop Components

For a superheated inlet condition, the total pressure drop between the upstream and downstream plenums can be obtained from

$$\Delta P_{tot} = \Delta P_c + \Delta P_{sp,d} + \Delta P_{tp} + \Delta P_{sp,f} + \Delta P_e. \quad (3.3)$$

The contraction pressure loss and expansion recovery at the inlet and outlet of the micro-channels, respectively, are determined from relations by Collier and Thome (1994),

$$\Delta P_c = \frac{G^2 \nu_f}{2} \left[\left(\frac{1}{C_c} - 1 \right)^2 + (1 - \sigma_c^2) \right] \left[1 + \frac{\nu_{fg} x_{e,in}}{\nu_f} \right], \quad (3.4a)$$

and

$$\Delta P_e = G^2 \sigma_c (\sigma_c - 1) \nu_f \left[1 + \frac{\nu_{fg} x_{e,out}}{\nu_f} \right]. \quad (3.4b)$$

For single-phase vapor flow at the plenum inlet, the contraction coefficient C_c due to the vena-contracta is obtained from a relation by Geiger (1964),

$$C_c = 1 - \frac{1 - \sigma_c}{2.08(1 - \sigma_c) + 0.5371}. \quad (3.5)$$

For single-phase hydrodynamically developing vapor flow in the inlet region of the micro-channels, the pressure drop can be expressed as a function of the apparent friction factor,

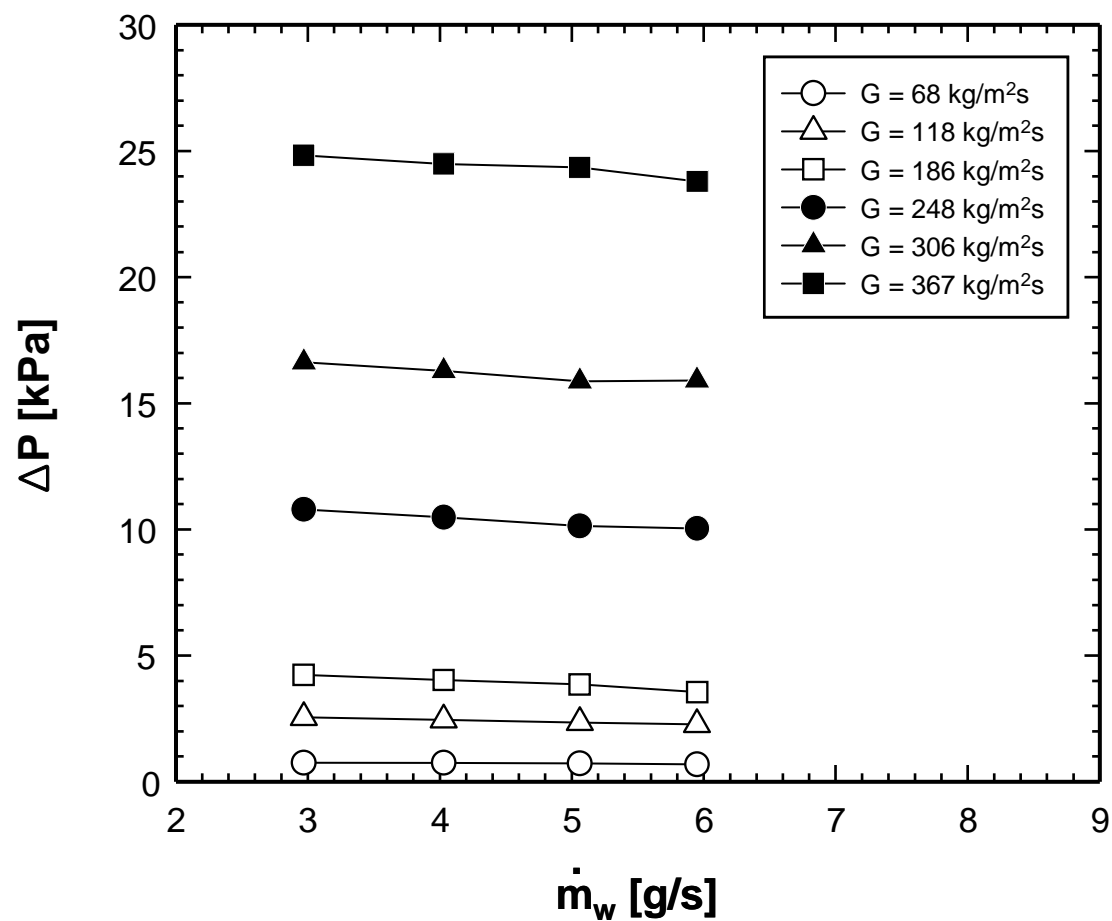


Figure 3.4 Variation of measured total pressure drop with water mass flow rate for different FC-72 mass velocities.

$$\Delta P_{sp,d} = \frac{2f_{app} G^2 L_{sp} \nu_g}{D_h}. \quad (3.6)$$

Since the FC-72 is introduced into the condensation module in superheated turbulent state with a Reynolds number range of 6000 – 31,000, the local pressure is predicted according to Zhi-qing (1982)'s analytical solution for turbulent developing vapor flow in a circular tube,

$$L_{sp}/D_h = 1.4039 \text{Re}_{sp}^{0.25} \delta^{+1.25} \left(1 + 0.1577\delta^+ - 0.1793\delta^{+2} - 0.0168\delta^{+3} + 0.0064\delta^{+4} \right), \quad (3.7)$$

$$\text{where } f_{app} = \left[\frac{1}{\left(1 - 0.25\delta^+ + 0.0667\delta^{+2} \right)^2} - 1 \right] \frac{0.25}{L_{sp}/D_h} \text{ for } \delta^+ < 1 \text{ (developing region)}, \quad (3.8a)$$

$$\text{and } f_{app} = \left(0.07 + 0.316 \frac{L_{sp}/D_h}{\text{Re}_{sp}^{0.25}} \right) \frac{0.25}{L_{sp}/D_h} \text{ for } \delta^+ = 1 \text{ (fully-developed region)}. \quad (3.8b)$$

When the FC-72 completely condenses to pure liquid in the downstream region of the micro-channel, the pressure drop for the single-phase liquid region, where the flow is assumed fully-developed, can be determined from (Shah and London, 1978; Incropera and Dewitt, 2002)

$$\Delta P_{sp,f} = \frac{2f_{sp,f} G^2 L_{sp,f} \nu_f}{D_h}, \quad (3.9)$$

$$\text{where } f_{sp,f} \text{Re}_{sp,f} = 24 \left(1 - 1.3553\beta + 1.9467\beta^2 - 1.7012\beta^3 + 0.9564\beta^4 - 0.2537\beta^5 \right)$$

$$\text{for } \text{Re}_{sp,f} < 2,000, \quad (3.10a)$$

$$f_{sp,f} = 0.079 \text{Re}_{sp,f}^{-0.25} \text{ for } 2,000 \leq \text{Re}_{sp,f} < 20,000, \quad (3.10b)$$

$$\text{and } f_{sp,f} = 0.046 \text{Re}_{sp,f}^{-0.2} \text{ for } \text{Re}_{sp,f} \geq 20,000. \quad (3.10c)$$

For the two-phase region, the pressure drop consists of accelerational and frictional components,

$$\Delta P_{tp} = \Delta P_{tp,A} + \Delta P_{tp,F}. \quad (3.11)$$

For a constant mass velocity, the differential form of accelerational two-phase pressure drop can be expressed as

$$-\left(\frac{dP}{dz} \right)_A = G^2 \frac{d}{dz} \left[\frac{\nu_g x^2}{\alpha} + \frac{\nu_f (1-x)^2}{(1-\alpha)} \right], \quad (3.12)$$

where the void fraction can be obtained from Zivi (1964)'s correlation

$$\alpha = \left[1 + \left(\frac{1-x}{x} \right) \left(\frac{\nu_f}{\nu_g} \right)^{2/3} \right]^{-1}. \quad (3.13)$$

For the homogeneous equilibrium model, the void fraction is related to thermodynamic equilibrium quality by the relation

$$\alpha = \left[1 + \left(\frac{1-x}{x} \right) \left(\frac{\nu_f}{\nu_g} \right) \right]^{-1}. \quad (3.14)$$

Substituting the above relation in Eq. (3.12) while neglecting property changes yields the following widely used form of accelerational two-phase pressure gradient for the homogeneous equilibrium model,

$$-\left(\frac{dP}{dz} \right)_A = G^2 \nu_{fg} \frac{dx}{dz}. \quad (3.15)$$

The accelerational two-phase pressure drop can be determined by integrating Eqs. (3.12) or (3.15) numerically along the streamwise direction,

$$\Delta P_{tp,A} = \int_0^{L_{tp}} -\left(\frac{dP}{dz} \right)_A dz. \quad (3.16)$$

When determining the total pressure drop via the homogeneous equilibrium models, both the simple and general forms of accelerational pressure drop, Eqs. (3.15) and (3.12), respectively, will be examined. In case of separated flow models, only the general form of accelerational pressure gradient, Eq. (3.12), will be used to determine the accelerational pressure drop.

The frictional two-phase pressure drop can be determined by integrating the relation for frictional pressure gradient corresponding to the chosen model or correlation as indicated in Tables 3.1 - 3.3,

$$\Delta P_{tp,F} = \int_0^{L_{tp}} -\left(\frac{dP}{dz} \right)_F dz. \quad (3.17)$$

In the two-phase condensing region, the local saturation temperature of FC-72 is obtained from the local saturation pressure, and the thermophysical properties for liquid and vapor are based on local saturation pressure.

3.2.3. Comparison with Different Pressure Drop Models and Correlations

To determine the two-phase frictional pressure drop, both homogeneous equilibrium and separated flow models are considered.

Homogeneous Equilibrium Model (HEM)

Both constant friction factor (Bottomley, 1936; Lewis and Robertson, 1940; Benjamin and Miller, 1942; Markson *et al.*, 1942; Allen, 1951) and two-phase mixture viscosity (McAdams *et al.*, 1942; Akers *et al.*, 1958; Cicchitti *et al.*, 1960; Owens, 1961; Dukler *et al.*, 1964; Beattie and Whalley, 1982; Lin *et al.*, 1991) methods are used to predict the two-phase frictional pressure gradient via the homogeneous equilibrium model. In order to check the sensitivity of different accelerational pressure drop relations to total pressure drop, both the simple and general forms of accelerational pressure drop, Eqs. (3.15) and (3.12), respectively, are compared. Figures 3.5(a) and 3.5(b) compare the present FC-72 pressure drop data to predictions based on two different constant friction factors, $f_{tp} = 0.003$ and 0.005 , and seven different two-phase viscosity models. The total pressure drop in Fig. 3.5(a) is based entirely on the homogeneous equilibrium model (*i.e.*, using Eq. (3.15) for the accelerational pressure gradient), while the accelerational pressure gradient in Fig. 3.5(b) is based on Eq. (3.12) and Zivi's relation for void fraction. Comparing Figs. 3.5(a) and 3.5(b) shows the former approach only slightly overpredicts the data compared to the latter. Therefore, the differences in predictions of total pressure drop in Figs. 3.5(a) and 3.5(b) are due mostly to the different frictional pressure drop models used.

Given the slightly better predictions in Fig. 3.5(b) compared to Fig. 3.5(a), all subsequent accelerational pressure drop calculations in Figs. 3.6, 3.7(a) and 3.7(b) will be based on the general form of accelerational pressure drop, Eq. (3.12), using Zivi's void fraction relation.

Table 3.1 provides details of the constant two-phase friction factor and two-phase viscosity methods as well as their accuracy in predicting the present data. The accuracy of individual models is measured by mean absolute error, which is defined as

$$MAE = \frac{1}{M} \sum \frac{|\Delta P_{\text{pred}} - \Delta P_{\text{exp}}|}{\Delta P_{\text{exp}}} \times 100\% . \quad (3.18)$$

In general, the homogeneous equilibrium model is better suited to dispersed two-phase flows such as bubbly flow. The fundamental premises of this model fall apart for

Table 3.1 Homogeneous equilibrium model for two-phase frictional pressure gradient, and corresponding MAE in predicting present total pressure drop data.

$\left(\frac{dP}{dz}\right)_F = -\frac{2}{D_h} f_{tp} \bar{\rho} u^2 = -\frac{2}{D_h} f_{tp} v_f G^2 \left(1 + x \frac{v_{fg}}{v_f}\right)$			
Constant friction factor method			
Author(s)	Applications	f_{tp}	MAE [%]
Lewis and Robertson (1940) Markson <i>et al.</i> (1942)	High pressure steam-water boilers	0.005	31.72
Bottomley (1936) Benjamin and Miller (1942) Allen (1951)	Low pressure flashing steam-water flows	0.003	56.77
Two-phase mixture viscosity method			
$f_{tp} \text{Re}_{tp} = 24(1 - 1.3553\beta + 1.9467\beta^2 - 1.7012\beta^3 + 0.9564\beta^4 - 0.2537\beta^5)$ for $\text{Re}_{tp} < 2,000$ $f_{tp} = 0.079 \text{Re}_{tp}^{-0.25}$ for $2,000 \leq \text{Re}_{tp} < 20,000$ $f_{tp} = 0.046 \text{Re}_{tp}^{-0.2}$ for $\text{Re}_{tp} \geq 20,000$, where $\text{Re}_{tp} = GD_h/\mu_{tp}$			
Author(s)	Equation	MAE [%]	
McAdams <i>et al.</i> (1942)	$\frac{1}{\mu_{tp}} = \frac{x}{\mu_g} + \frac{1-x}{\mu_f}$	17.22	
Akers <i>et al.</i> (1958)	$\mu_{tp} = \frac{\mu_f}{\left[(1-x) + x\left(\frac{v_g}{v_f}\right)^{0.5}\right]}$	34.98	
Cicchitti <i>et al.</i> (1960)	$\mu_{tp} = x\mu_g + (1-x)\mu_f$	85.16	
Owens (1961)	$\mu_{tp} = \mu_f$	306.0	
Dukler <i>et al.</i> (1964)	$\mu_{tp} = \frac{xv_g\mu_g + (1-x)v_f\mu_f}{xv_g + (1-x)v_f}$	15.92	
Beattie and Whalley (1982)	$\mu_{tp} = \omega\mu_g + (1-\omega)(1+2.5\omega)\mu_f$ $\omega = \frac{xv_g}{v_f + xv_{fg}}$	17.34	
Lin <i>et al.</i> (1991)	$\mu_{tp} = \frac{\mu_f\mu_g}{\mu_g + x^{1.4}(\mu_f - \mu_g)}$	17.05	

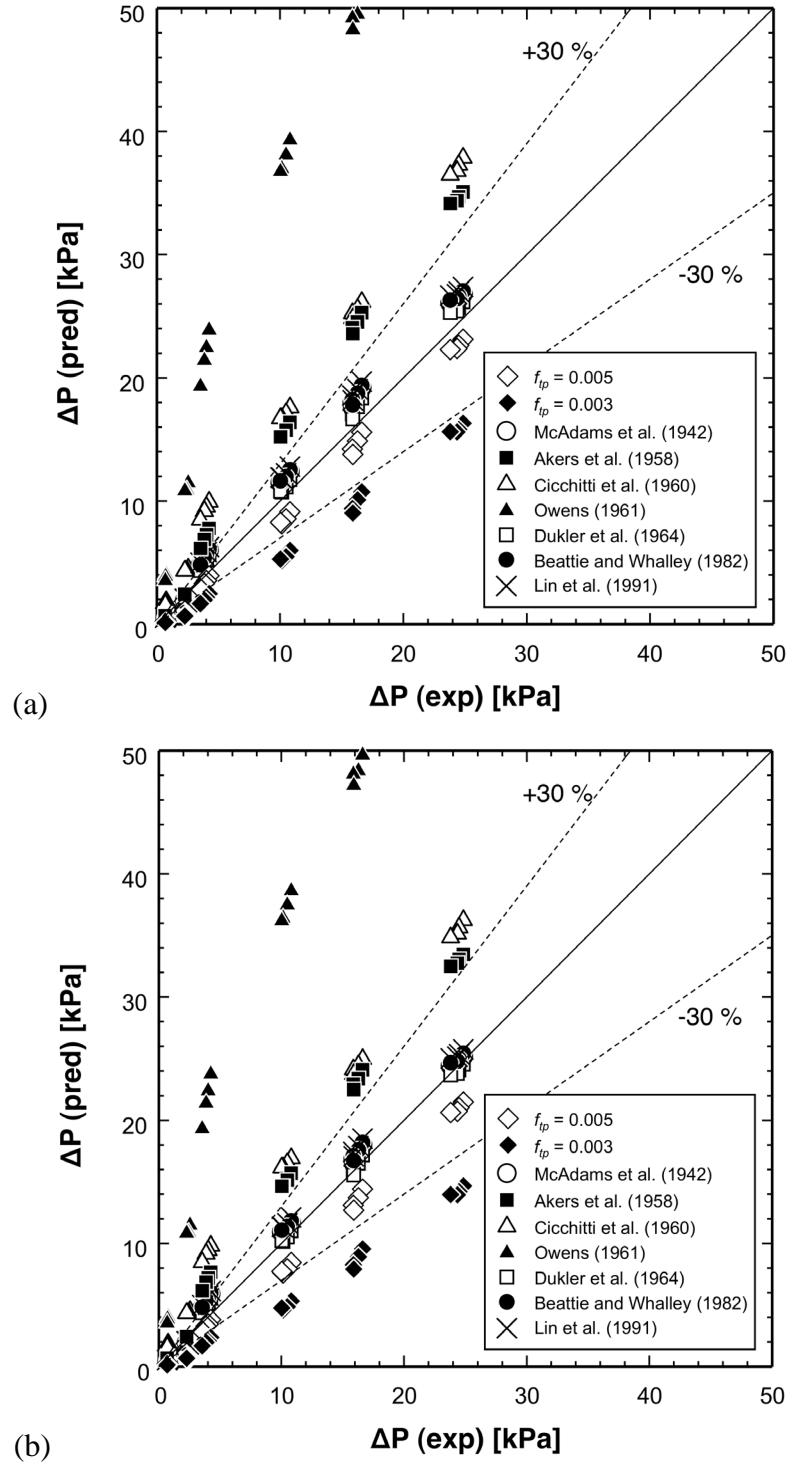


Figure 3.5 Comparison of present FC-72 pressure drop data with predictions of (a) homogeneous equilibrium model, and (b) homogeneous equilibrium model with accelerational pressure drop based on separated flow model and Zivi (1964)'s relation for void fraction.

regimes involving separation between the liquid and vapor phases or large velocity differences between the two phases. Annular flow is an example of a regime where the use of the homogenous equilibrium model is generally avoided. In spite of the fact that annular flow was dominant throughout the present measurement, Figs. 3.5(a) and 3.5(b) prove that, when used in conjunction with most two-phase viscosity models, excepting those of Cicchitti *et al.* (1960) and Owens (1961), the homogeneous equilibrium model provides fairly accurate predictions of the present experimental data. Most notably, the viscosity model by Dukler *et al.* (1964), with a MAE of 15.92%, provides the best predictions among all viscosity relations. In fact, this model provides better accuracy than all separated flow correlations as discussed in the next section.

Figure 3.6 shows the contributions of individual pressure drop components to total pressure drop using the mixture viscosity model by Dukler *et al.*. For a condensing flow, the accelerational two-phase pressure drop term is negative because of the deceleration along the stream-wise direction. In fact, condensation reduces two-phase pressure drop, as opposed to flow boiling, where two-phase pressure drop is increased by the stream-wise acceleration, and the accelerational pressure drop is positive. Figure 3.6 shows that the magnitude of ΔP_{tot} is dictated mostly by two-phase friction and acceleration. Increasing the mass velocity decreases the magnitude of $\Delta P_{tp,A} / \Delta P_{tot}$ because of the decreasing amount of vapor being condensed. The contributions of $\Delta P_{sp,f}$ and ΔP_e to ΔP_{tot} are minimal, while those of ΔP_c and $\Delta P_{sp,d}$ are more significant because of the pure vapor state at the micro-channel inlet.

Separated Flow Models (SFM)

Tables 3.2 and 3.3 provide a select summary of separated flow frictional pressure drop correlations that have been recommended for macro-channels (Lockhart and Martinelli, 1949; Friedel, 1979; Chisholm, 1983; Muller-Steinhagen and Heck, 1986; Jung and Radermacher, 1989; Wang *et al.*, 1997; Cavallini *et al.*, 2002) and mini/micro-channels (Mishima and Hibiki, 1996; Tran *et al.*, 2000; Chen *et al.*, 2001; Lee and Lee, 2001; Zhang and Webb, 2001; Yu *et al.*, 2002; Lee and Mudawar, 2005; Nino *et al.*, 2005; Hwang and Kim, 2006), respectively. These include a mix of correlations for flow boiling and condensation, adiabatic, flow boiling and condensing flows, and for isolated tubes and multi-channel heat sinks. Notice that the correlation of Jung and Radermacher (1989) is based on the assumption of $\Delta P_{tp} \approx \Delta P_f$ because the accelerational component was found to be small in their flow boiling experiments.

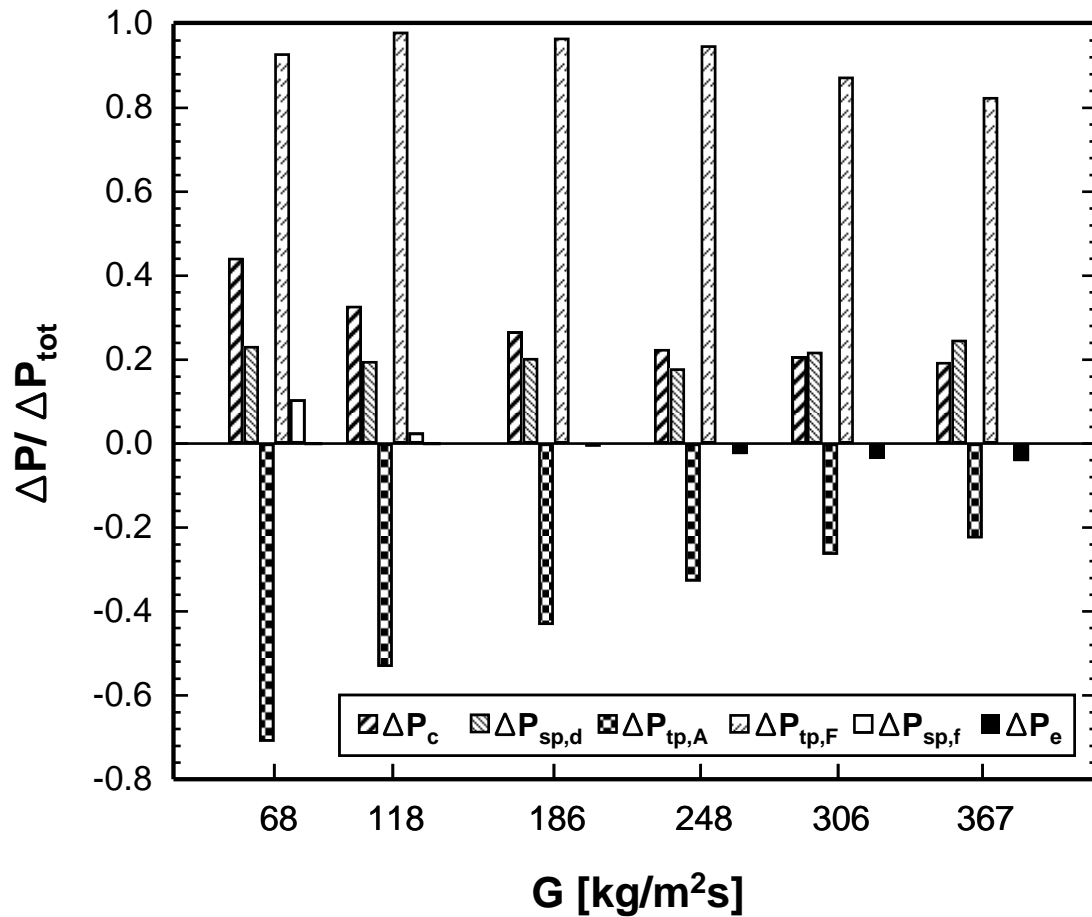


Figure 3.6 Contributions of individual components of pressure drop to total pressure drop for different mass velocities and $\dot{m}_w = 3\text{g/s}$ predicted with the frictional pressure gradient determined by the homogenous equilibrium model using the viscosity model of Dukler *et al.* (1964), and the accelerational pressure gradient determined by the separated flow model using Zivi (1964)'s relation for void fraction.

Table 3.2 Two-phase frictional pressure gradient correlations for macro-channels based on the separated flow model, and corresponding MAE in predicting present total pressure drop data.

Author(s)	Equation	Remarks	MAE [%]
Lockhart and Martinelli (1949)	$\left(\frac{dP}{dz}\right)_F = \left(\frac{dP}{dz}\right)_f \phi_f^2, \phi_f^2 = 1 + \frac{C}{X} + \frac{1}{X^2}, X^2 = \frac{(dP/dz)_f}{(dP/dz)_g}$ $C_{vv} = 5, C_{tv} = 10, C_{vt} = 12, C_{tt} = 20$	$D_h = 1.49 - 25.83$ mm Adiabatic Fluids: water, oils, hydrocarbons	80.26
Friedel (1979)	$\left(\frac{dP}{dz}\right)_F = \left(\frac{dP}{dz}\right)_{fo} \phi_{fo}^2, \phi_{fo}^2 = (1-x)^2 + x^2 \left(\frac{\nu_g}{\nu_f}\right) \left(\frac{f_{go}}{f_{fo}}\right) + \dots$ $+ 3.24x^{0.78}(1-x)^{0.224} \left(\frac{\nu_g}{\nu_f}\right)^{0.91} \left(\frac{\mu_g}{\mu_f}\right)^{0.19} \left(1 - \frac{\mu_g}{\mu_f}\right)^{0.7} Fr_{tp}^{-0.045} We_{tp}^{-0.035}$ $Fr_{tp} = \frac{G^2}{g D_h \rho_H^2}, We_{tp} = \frac{G^2 D_h}{\sigma \rho_H}, \rho_H = \frac{1}{x\nu_g + (1-x)\nu_f}$	$D > 4$ mm Fluids: air/water, air/oil, R12 (25000 data points)	173.4
Chisholm (1983)	$\left(\frac{dP}{dz}\right)_F = \left(\frac{dP}{dz}\right)_{fo} \phi_{fo}^2, \phi_{fo}^2 = 1 + (\Gamma^2 - 1) \left[B x^{0.875} (1-x)^{0.875} + x^{1.75} \right]$ $\Gamma^2 = \frac{(dP/dz)_{go}}{(dP/dz)_{fo}}, \text{ for } B \text{ values refer to Chisholm (1983)}$	Flow boiling Fluids: air/water, steam	114.1
Muller-Steinhagen and Heck (1986)	$\left(\frac{dP}{dz}\right)_F = \left(\frac{dP}{dz}\right)_{fo} + 2 \left[\left(\frac{dP}{dz}\right)_{go} - \left(\frac{dP}{dz}\right)_{fo} \right] x \left\{ (1-x)^{1/3} + \left(\frac{dP}{dz}\right)_{go} x^3 \right\}$	$D = 4 - 392$ mm Fluids: air/water, water, hydrocarbons, refrigerants (9300 data points)	54.88
Jung and Radermacher (1989)	$\left(\frac{dP}{dz}\right)_F = \left(\frac{dP}{dz}\right)_{fo} \phi_{fo}^2, \phi_{fo}^2 = 12.82 X_u^{-1.47} (1-x)^{1.8}$ $X_u = \left(\frac{\mu_f}{\mu_g}\right)^{0.1} \left(\frac{1-x}{x}\right)^{0.9} \left(\frac{\nu_f}{\nu_g}\right)^{0.5}$	$D = 9.1$ mm Annular flow boiling Fluids: pure and mixtures of R22, R114, R12, R152a	288.3
Wang <i>et al.</i> (1997)	For $G \geq 200 \text{ kg/m}^2 \text{ s}$, $\left(\frac{dP}{dz}\right)_F = \left(\frac{dP}{dz}\right)_g \phi_g^2$, $\phi_g^2 = 1 + 9.4X^{0.62} + 0.564X^{2.45}$ For $G < 200 \text{ kg/m}^2 \text{ s}$, $\left(\frac{dP}{dz}\right)_F = \left(\frac{dP}{dz}\right)_f \phi_f^2, \phi_f^2 = 1 + \frac{C}{X} + \frac{1}{X^2}$, $C = 4.566 \times 10^{-6} X^{0.128} Re_{fo}^{0.938} \left(\frac{\nu_f}{\nu_g}\right)^{2.15} \left(\frac{\mu_f}{\mu_g}\right)^{5.1}$	$D = 6.5$ mm Adiabatic Fluids: R22, R134a, R407C	86.19
Cavallini <i>et al.</i> (2002)	$\left(\frac{dP}{dz}\right)_F = \left(\frac{dP}{dz}\right)_{fo} \phi_{fo}^2, We_{go} = \frac{G^2 D_h}{\rho_g \sigma}, j_g^* = \frac{Gx}{\rho_g} \sqrt{\frac{\rho_g}{(\rho_f - \rho_g) g D_h}}$ $\text{For } j_g^* \geq 2.5, \phi_{fo}^2 = (1-x)^2 + x^2 \left(\frac{\nu_g}{\nu_f}\right) \left(\frac{f_{go}}{f_{fo}}\right) + \dots$ $+ 1.262x^{0.6978} \left(\frac{\nu_g}{\nu_f}\right)^{0.3278} \left(\frac{\mu_g}{\mu_f}\right)^{-1.181} \left(1 - \frac{\mu_g}{\mu_f}\right)^{3.477} We_{go}^{-0.1458}$ $\text{For } j_g^* < 2.5, \phi_{fo}^2 = \phi_{fo, \text{Friedel}}^2$	$D > 3.1$ mm Condensation Fluids: R22, R134a, R125, R32, R236ea, R407c, R410A	597.8

Table 3.3 Two-phase frictional pressure gradient correlations for mini/micro-channels based on the separated flow model, and corresponding MAE in predicting present total pressure drop data.

Author(s)	Equation	Remarks	MAE [%]
Mishima and Hibiki (1996)	$\left(\frac{dP}{dz}\right)_F = \left(\frac{dP}{dz}\right)_f \phi_f^2, \phi_f^2 = 1 + \frac{C}{X} + \frac{1}{X^2}$ $C = 21[1 - \exp(-0.319D_h)]; D_h [mm]$	$D = 1.05\text{--}4.08$ mm Adiabatic Fluid: air/water	27.15
Tran <i>et al.</i> (2000)	$\left(\frac{dP}{dz}\right)_F = \left(\frac{dP}{dz}\right)_{fo} \phi_{fo}^2, N_{conf} = \sqrt{\frac{\sigma}{g(\rho_f - \rho_g)D_h^2}}$ $\phi_{fo}^2 = 1 + (4.3\Gamma^2 - 1)[N_{conf}x^{0.875}(1-x)^{0.875} + x^{1.75}]$	$D_h = 2.40, 2.46, 2.92$ mm Flow boiling Fluids: R134a, R12, R113	276.1
Lee and Lee (2001)	$\left(\frac{dP}{dz}\right)_F = \left(\frac{dP}{dz}\right)_f \phi_f^2, \phi_f^2 = 1 + \frac{C}{X} + \frac{1}{X^2}, \psi = \frac{\mu_f j_f}{\sigma}, \lambda = \frac{\mu_f^2}{\rho_f \sigma D_h}$ $C_{vv} = 6.833 \times 10^{-8} \lambda^{-1.317} \psi^{0.719} \text{Re}_{fo}^{0.557}, C_{iv} = 3.627 \text{Re}_{fo}^{0.174}$ $C_{vt} = 6.185 \times 10^{-2} \text{Re}_{fo}^{0.726}, C_{tt} = 0.048 \text{Re}_{fo}^{0.451}$	$D_h = 0.78\text{--}6.67$ mm Adiabatic Fluid: air/water	36.26
Zhang and Webb (2001)	$\left(\frac{dP}{dz}\right)_F = \left(\frac{dP}{dz}\right)_{fo} \phi_{fo}^2$ $\phi_{fo}^2 = (1-x)^2 + 2.87x^2 P_R^{-1} + 1.68x^{0.8}(1-x)^{0.25} P_R^{-1.64}, P_R = P/P_{crit}$	$D = 0.96\text{--}6.20$ mm Adiabatic Multi-channel Fluids: R134a, R22, R404a	522.9
Chen <i>et al.</i> (2001)	$\left(\frac{dP}{dz}\right)_F = \left(\frac{dP}{dz}\right)_{fo, Friedel} \Omega$ $\text{For } Bo < 2.5, \Omega = \frac{0.0333 \text{Re}_{fo}^{0.45}}{\text{Re}_g^{0.09}(1 + 0.4e^{-Bo})}$ $\text{For } Bo \geq 2.5, \Omega = \frac{We_{tp}^{0.2}}{(2.5 + 0.06Bo)}, Bo = g(\rho_f - \rho_g) \frac{(D_h/2)^2}{\sigma}$	$D = 1.02\text{--}9$ mm Adiabatic Fluids: air/water, R410A, ammonia	47.65
Yu <i>et al.</i> (2002)	$\left(\frac{dP}{dz}\right)_F = \left(\frac{dP}{dz}\right)_f \phi_f^2, \phi_f^2 = \frac{1}{X_{vt}^{1.9}},$ $X_{vt} = 18.65 \left(\frac{\nu_f}{\nu_g}\right)^{0.5} \left(\frac{1-x}{x}\right) \frac{\text{Re}_g^{0.1}}{\text{Re}_f^{0.5}}$	$D = 2.98$ mm Flow boiling Fluids: water, ethylene glycol, aqueous mixtures of ethylene glycol	51.25
Nino <i>et al.</i> (2005)	$\left(\frac{dP}{dz}\right)_F = \left(\frac{dP}{dz}\right)_{go} \phi_{go}^2, We_g = \frac{(Gx)^2 D_h}{\sigma \rho_g}$ $\phi_{go}^2 = \exp(-0.046X_{ann}) + 0.22[\exp(-0.002X_{ann}) - \exp(-7X_{ann})]$ $X_{ann} = \left[\left(X_{tt} + \frac{1}{We_g^{1.3}} \right) \left(\frac{\nu_g}{\nu_f} \right)^{0.9} \right], X_{tt} = \left(\frac{\mu_f}{\mu_g} \right)^{0.125} \left(\frac{1-x}{x} \right)^{0.875} \left(\frac{\nu_f}{\nu_g} \right)^{0.5}$	$D_h = 1.02, 1.54$ mm Adiabatic Multi-channel Fluids: R410A, R134a, air/water	34.24
Lee and Mudawar (2005)	$\left(\frac{dP}{dz}\right)_F = \left(\frac{dP}{dz}\right)_f \phi_f^2, \phi_f^2 = 1 + \frac{C}{X} + \frac{1}{X^2}$ $C_{vv} = 2.16 \text{Re}_{fo}^{0.047} We_{fo}^{0.60}, C_{vt} = 1.45 \text{Re}_{fo}^{0.25} We_{fo}^{0.23}, We_{fo} = \frac{G^2 D_h}{\sigma \rho_f}$	$D_h = 0.349$ mm Flow boiling Multi-channel Fluids: R134a, water	57.55
Hwang and Kim (2006)	$\left(\frac{dP}{dz}\right)_F = \left(\frac{dP}{dz}\right)_f \phi_f^2, \phi_f^2 = 1 + \frac{C}{X} + \frac{1}{X^2}, C = 0.227 \text{Re}_{fo}^{0.452} X^{-0.32} N_{conf}^{-0.82}$	$D = 0.244\text{--}0.792$ mm Adiabatic Fluid: R134a	53.95

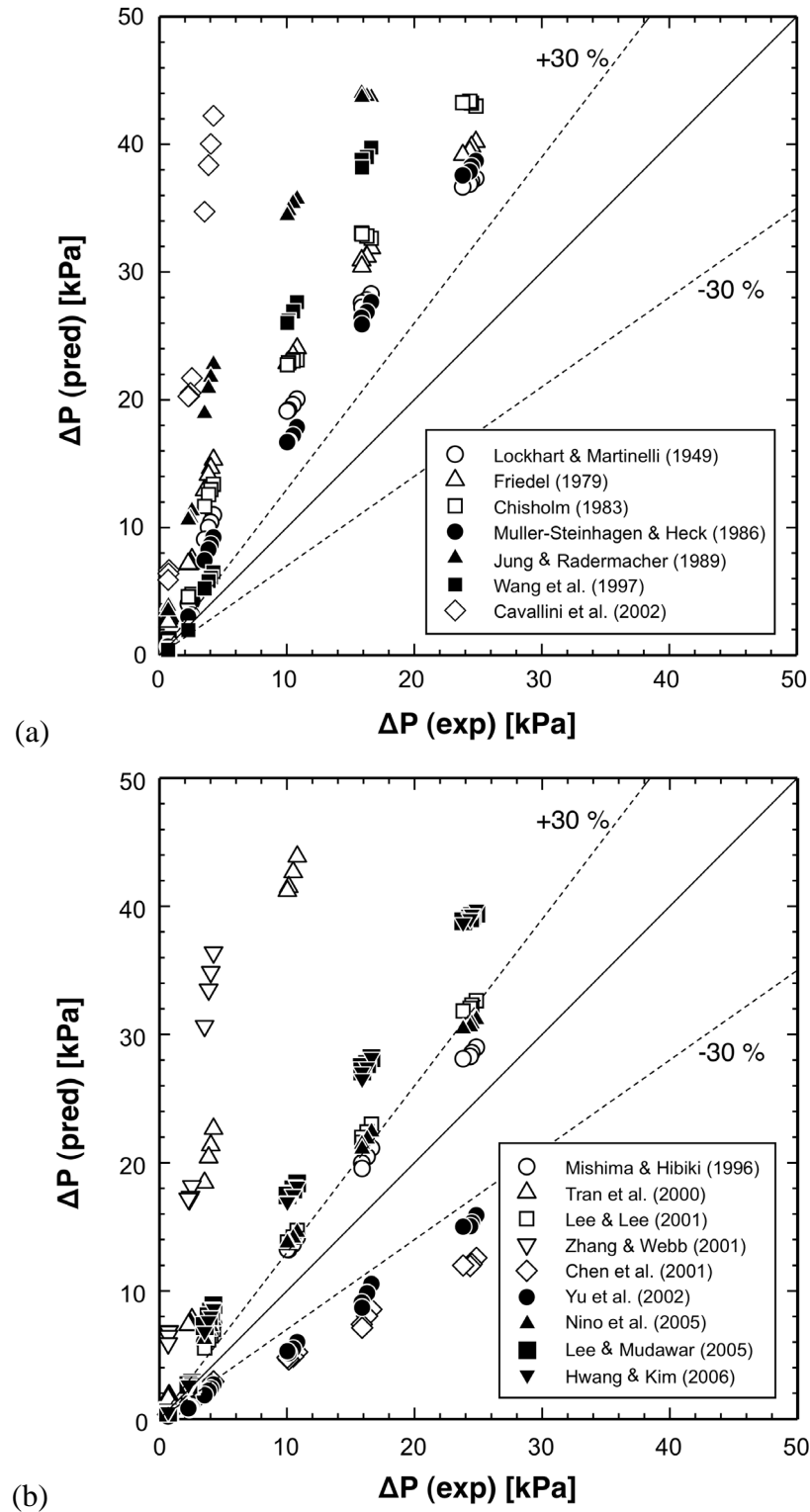


Figure 3.7 Comparison of present FC-72 pressure drop data with predictions of separated flow correlations recommended for (a) macro-channels and (b) mini/micro-channels.

Figure 3.7(a) shows that all seven macro-channel correlations overpredict the present FC-72 condensation data. Notably, the total pressure drop is highly overpredicted by the correlations of Friedel (1979), Chisholm (1983), Jung and Radermacher (1989), and Cavallini *et al.* (2002), with corresponding MAE values of 173.42%, 114.06%, 288.27%, and 597.75%, respectively.

Figure 3.7(b) compares the present FC-72 micro-channel condensation pressure drop data with predictions using separated flow correlations for frictional pressure drop in mini/micro-channels. The correlations of Mishima and Hibiki (1996), Lee and Lee (2001), and Nino *et al.* (2005), which are all based on adiabatic air-water flow, provide fair predictions of the present data, with MAE values of 27.15%, 36.26%, and 34.24%, respectively. The correlations of Lee and Mudawar (2005a) and Tran *et al.* (2000), which are based on micro-channel flow boiling, overpredict the present data with a MAE of 57.55% and 276.1%, respectively. The large MAE of 522.86% for Zhang and Webb (2001)'s correlation may be attributed to the relatively low reduced pressure range of the present FC-72 data, $P_R = 0.05\text{--}0.07$, compared to the recommended range of $P_R > 0.2$ for the original correlation.

By closely examining the predictive accuracy of the separated mini/micro-channels flow correlations, it can be concluded that, even on a local basis, condensation behavior is fundamentally different from that of flow boiling and perhaps closer to that of adiabatic two-phase flow. One obvious difference between flow boiling on one hand, and condensing and adiabatic two-phase flows on the other, is the relative abundance of entrained droplet in the former and absence from the latter two, as schematically shown in Fig. 3.8(a). This phenomenon is especially important for mini/micro-channel flows, where the annular regime is dominant regardless of heating conditions. As indicated by Qu and Mudawar (2004), the transition to the annular regime in flow boiling occurs far upstream in a micro-channel, but with an abundance of entrained droplets that are formed by shattering of liquid from the micro-channel's upstream. However, the flow visualization results of the present study show no droplets are formed in the annular regions of the micro-channel. This conclusion highlights the need for new models and correlations that can accurately predict condensation behavior in mini/micro-channels, especially when implemented in a multi-channel configuration.

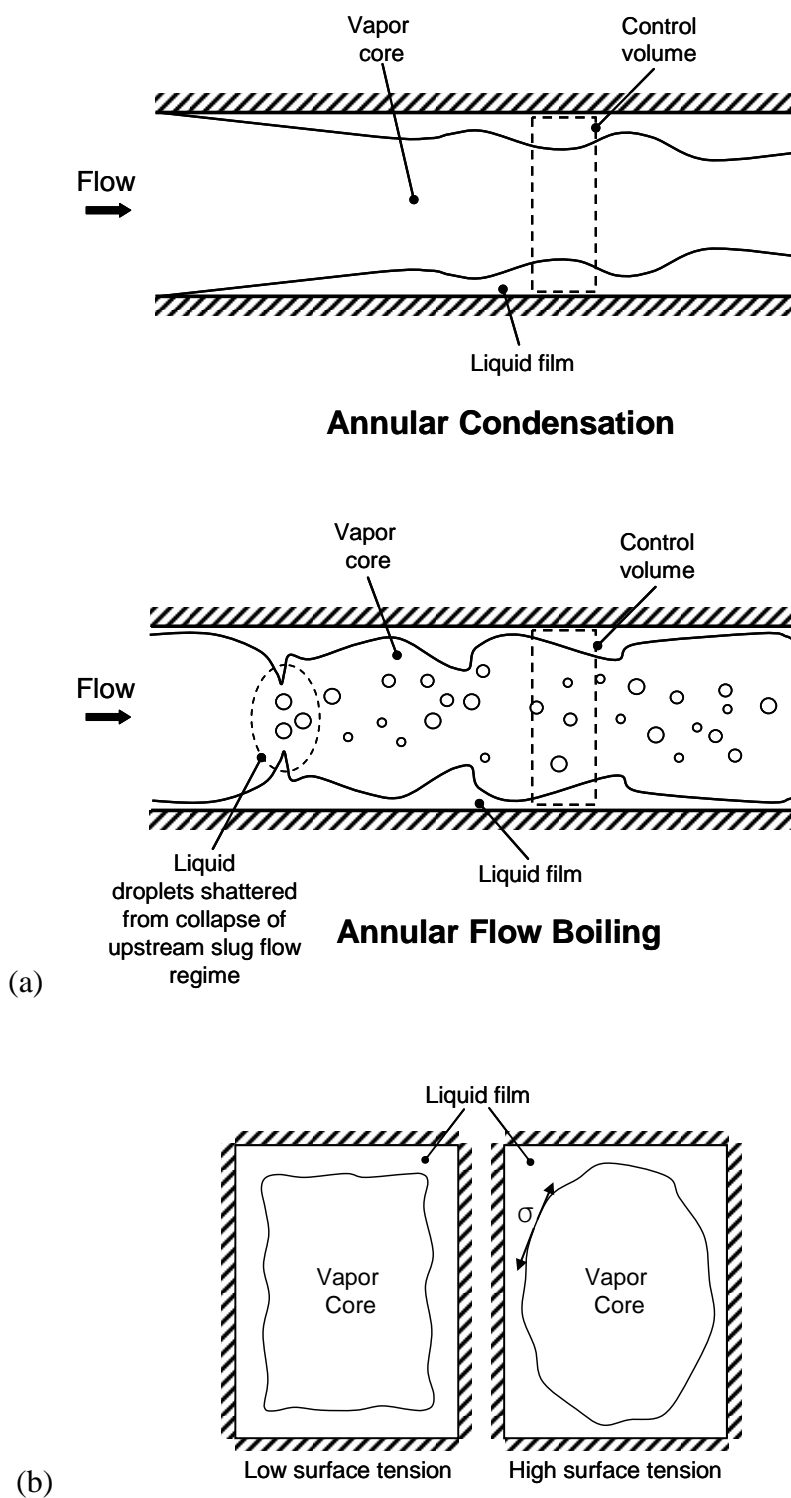


Figure 3.8 (a) Fundamental differences between annular condensation and annular flow boiling in micro-channels. (b) Effects of surface tension on liquid distribution along channel perimeter.

3.3. Condensation Heat Transfer Results

3.3.1. Heat Transfer Data Reduction

Efforts were made to achieve slightly superheated FC-72 conditions at the inlet to the condensation module. This helped maintain annular flow in the inlet region of the micro-channels and achieve high heat transfer coefficients as well as a broad range of operating conditions.

Figure 3.9 shows a unit cell illustrating key parameters that are used in determining the heat transfer performance of the condensation micro-channels. Unlike most boiling experiments, where the heat flux is measured from electrical power input, heat flux in this study is determined from temperature measurements along two parallel planes in the copper block beneath the micro-channels. Sixteen pairs of type-E thermocouples are embedded at 19-mm intervals along the length of the copper block. At each axial thermocouple location, both the heat flux along the base of the micro-channels and the base temperature are determined from temperature measurements by the thermocouple pair using the assumption of one-dimensional heat conduction between the two thermocouple planes.

$$q''_{base} = \frac{k_s(T_t - T_b)}{H_b}. \quad (3.19)$$

The temperature corresponding to the plane in line with the bottom of the micro-channels can be determined from

$$T_{w,b} = T_t + \frac{q''_{base} H_t}{k_s}. \quad (3.20)$$

The local rates of sensible heat loss in the superheated vapor region and latent heat loss in the two-phase condensing region from FC-72 can be calculated from the following energy balances, respectively,

$$\frac{\dot{m}}{N} c_{p,g} \Delta T_f = q''_{base} (W_{ch} + W_s) \Delta z, \quad (3.21a)$$

and

$$\frac{\dot{m}}{N} h_{fg} \Delta x = q''_{base} (W_{ch} + W_s) \Delta z. \quad (3.21b)$$

The onset of two-phase condensation occurs at a distance from the inlet of the micro-channel where the fluid temperature reaches the saturation temperature

corresponding to local pressure. The local quality in the superheated region can be determined from

$$x = 1 + \frac{c_{p,g}(T_f - T_{sat})}{h_{fg}}. \quad (3.22)$$

Figure 3.10 shows a sample of top and bottom thermocouple temperatures measured along the copper block for three FC-72 mass velocities. The corresponding temperature distribution along the two thermocouple planes is fitted by a third-order or fourth-order polynomial function of axial distance. These distributions are then used to determine the corresponding variations of base heat flux and thermodynamic equilibrium quality. Figure 3.10 shows that the base heat flux increases with increasing mass velocity due to the increasing temperature difference between the two thermocouple planes.

Inlet quality was maintained at 1.11 - 1.17 for low FC-72 mass velocities ($G = 68$ - 186 kg/m²s) and 1.08 - 1.10 for high mass velocities ($G = 248$ - 367 kg/m²s), which correspond to a single-phase superheated vapor region 1.1 - 3.1 cm long (4 - 10% of the channel length) and 2.7 - 5.8 cm long (9 - 19% of the channel length), respectively. For the two-phase condensation region ($x \leq 1$), the present study covered the following operating conditions: FC-72 mass velocities of $G = 68$ - 367 kg/m²s, FC-72 saturation temperatures of $T_{sat} = 57.2$ - 62.3°C , FC-72 qualities of $x = 1$ - 0 , water mass flow rates of $\dot{m}_w = 3$ - 6 g/s, and heat fluxes of $q''_w = 0.43$ - 3.21 W/cm².

3.3.2. Experimental Results

Kim and Mudawar (2010a, 2010b) showed that the one-dimensional fin analysis method is both convenient and accurate in evaluating the local heat transfer coefficient for micro-channels with rectangular, inverse trapezoidal, triangular, trapezoidal, diamond-shaped, and circular cross sections.

In case of a condenser having rectangular micro-channels with three-sided cooling walls (*i.e.*, assuming a perfectly insulating top cover plate) as illustrated in Fig. 3.9, applying the fin analysis method yields

$$h = \frac{q''_w(2H_{ch} + W_{ch})}{(T_{w,b} - T_f)(2\eta H_{ch} + W_{ch})} = \frac{q''_{base}(W_s + W_{ch})}{(T_{w,b} - T_f)(2\eta H_{ch} + W_{ch})}, \quad (3.23)$$

where q''_{base} is the base heat flux, and the fin efficiency and fin parameter are defined, respectively, as (Incropera and Dewitt, 2002)

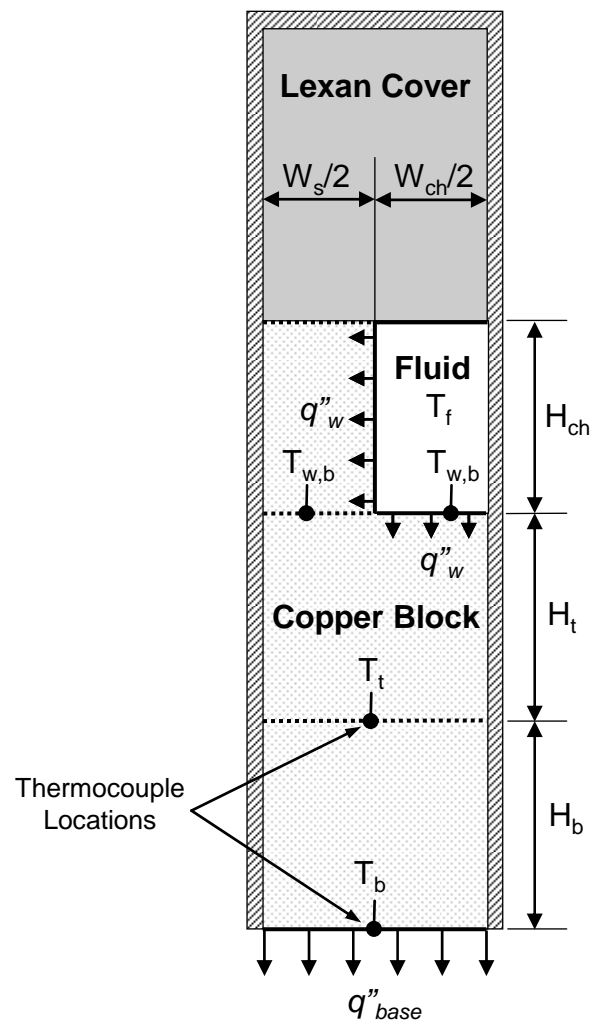


Figure 3.9 Unit cell for condensation micro-channel.

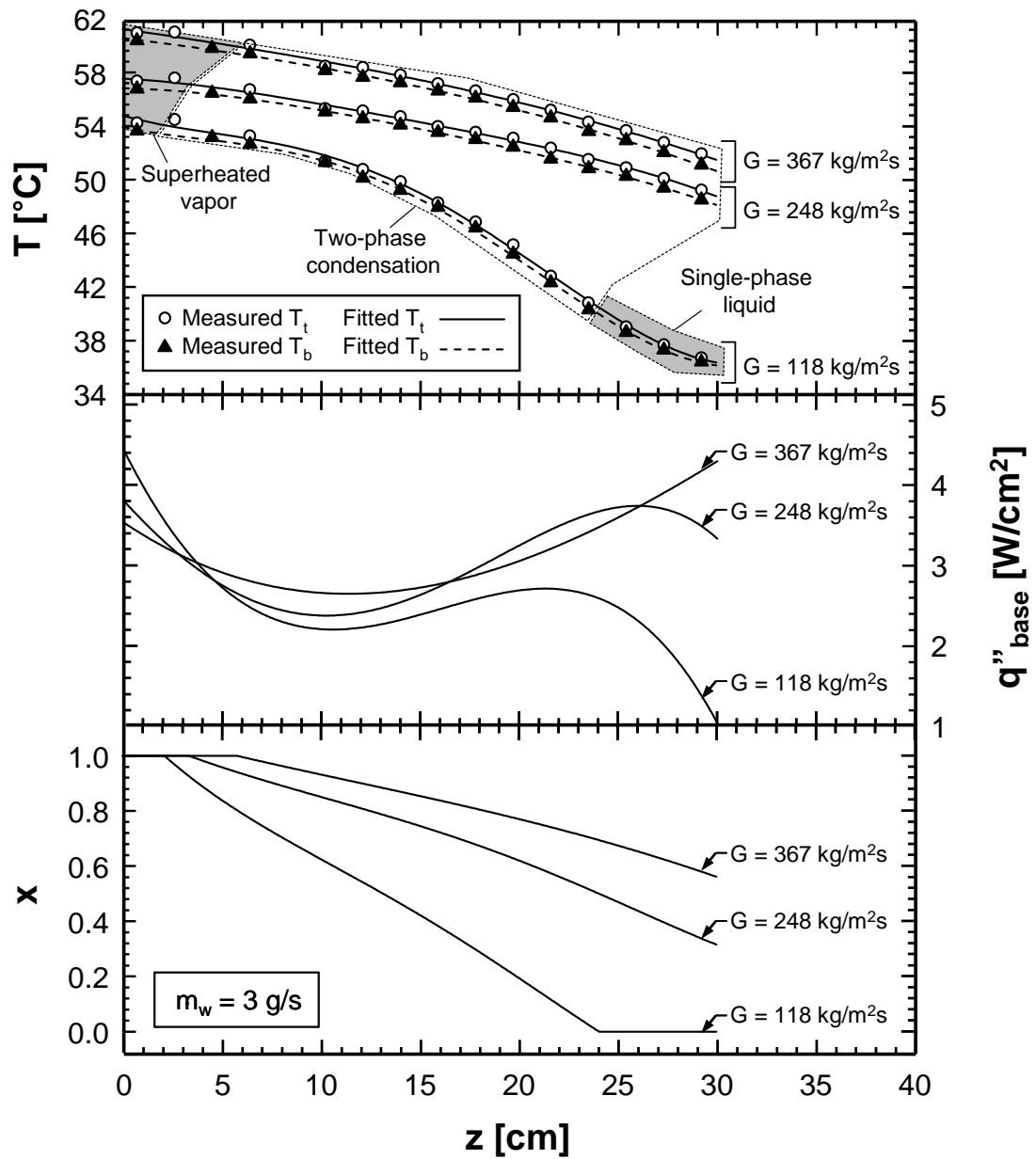


Figure 3.10 Variations of copper block temperatures, base heat flux, and thermodynamic equilibrium quality along stream-wise direction for different FC-72 mass velocities with $\dot{m}_w = 3$ g/s.

$$\eta = \frac{\tanh(mH_{ch})}{mH_{ch}}, \quad (3.24a)$$

and

$$m = \sqrt{\frac{2h}{k_s W_s}}. \quad (3.24b)$$

Figure 3.11 shows the variation of the experimentally-determined local FC-72 condensation heat transfer coefficient with thermodynamic equilibrium quality in the saturated region for different water mass flow rates and FC-72 mass velocities in the range of 68 - 367 kg/m²s. Very high heat transfer coefficient values are achieved near $x = 1$, where annular flow regime is initiated and the liquid film is very thin. The condensation coefficient decreases along the channel as the film gradually thickens and/or the annular regime is replaced by transition or slug flow regimes. Overall, there is a far stronger sensitivity to FC-72 mass velocity than to water flow rate.

Figure 3.12 shows the variation of local FC-72 condensation heat transfer coefficient with thermodynamic equilibrium quality in the saturated region for different FC-72 mass velocities and two water flow rates. Increasing the mass velocity of FC-72 extends the annular regime farther downstream towards lower quality values. Increasing the mass velocity increases the condensation heat transfer coefficient by thinning the liquid film due to the increased interfacial vapor shear stress. Notice that the slope of heat transfer coefficient plot in Fig. 3.12 decreases appreciably in range of $x = 0.4 - 0.7$ for $G = 248$ kg/m²s and $x = 0.6 - 0.8$ for $G = 306$ kg/m²s. As presented in Chapter 3.1, these quality ranges correspond mostly to the wavy-annular regime. It can therefore be inferred that at high mass velocities, interfacial waves enhance the condensation heat transfer by slowing the trend of declining heat transfer coefficient along the channel caused by the film thinning. Notice that the flattening in the variation of h_{tp} versus x is nonexistent for the lower mass velocities. This can be explained by the narrowing of the extent of the wavy annular regime at low mass velocities.

Figure 3.13 shows the variation of the average condensation heat transfer coefficient with water mass flow rate for different FC-72 mass velocities. It should be emphasized that all of the average condensation heat transfer coefficient data in this figure, as well as Figs. 3.14-3.16 and 3.20, correspond to values averaged over only the two-phase condensing region (corresponding to the range $x = 0 - 1$), and exclude the upstream superheated vapor region and downstream single-phase liquid region of the micro-channel. In Fig. 3.13, the condensation heat transfer coefficient increases with

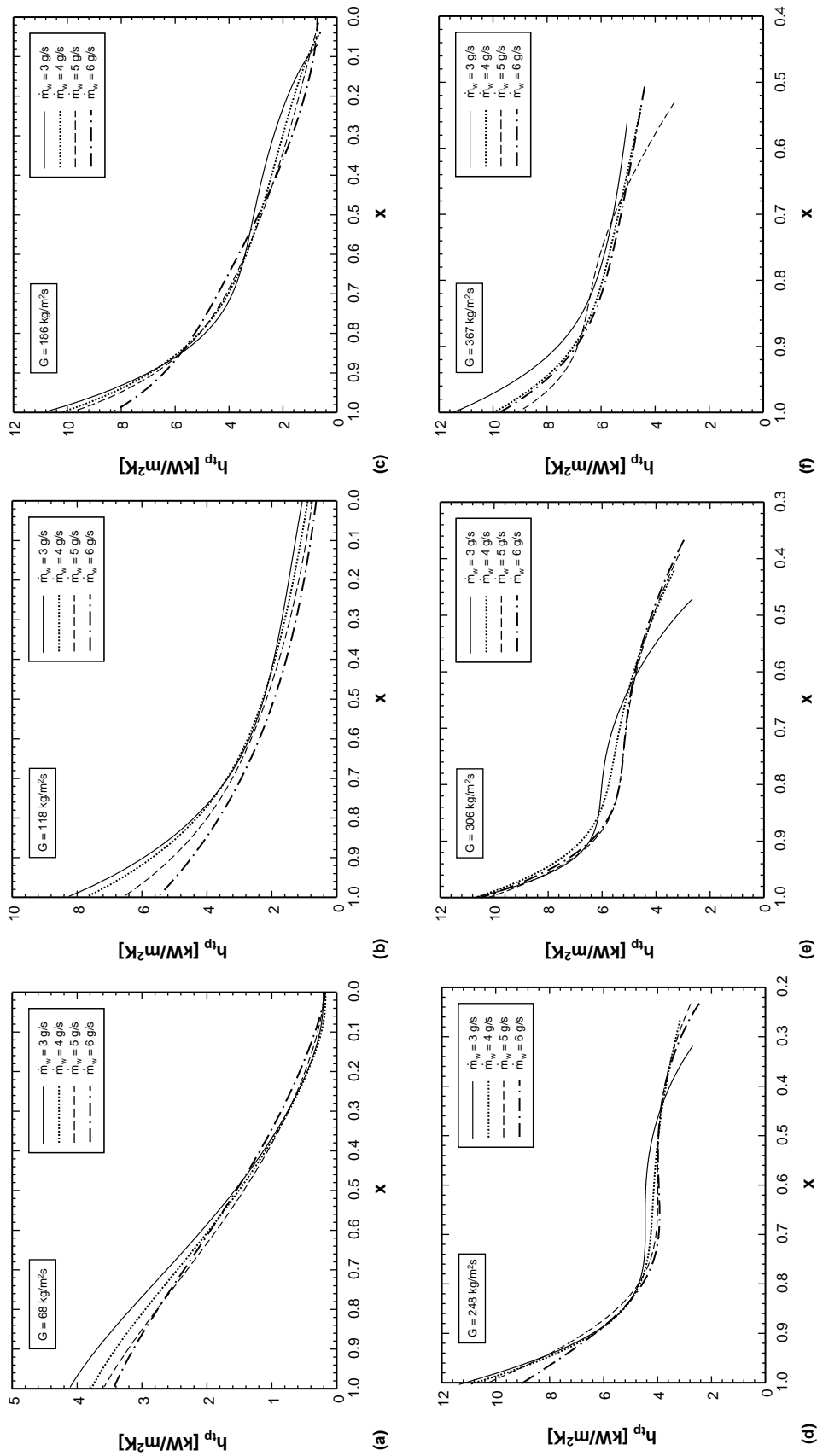


Figure 3.11 Variation of experimentally-determined local FC-72 condensation heat transfer coefficient with thermodynamic equilibrium quality for different coolant mass flow rates with (a) $G = 68 \text{ kg/m}^2\text{s}$, (b) $G = 118 \text{ kg/m}^2\text{s}$, (c) $G = 186 \text{ kg/m}^2\text{s}$, (d) $G = 248 \text{ kg/m}^2\text{s}$, (e) $G = 306 \text{ kg/m}^2\text{s}$, and (f) $G = 367 \text{ kg/m}^2\text{s}$.

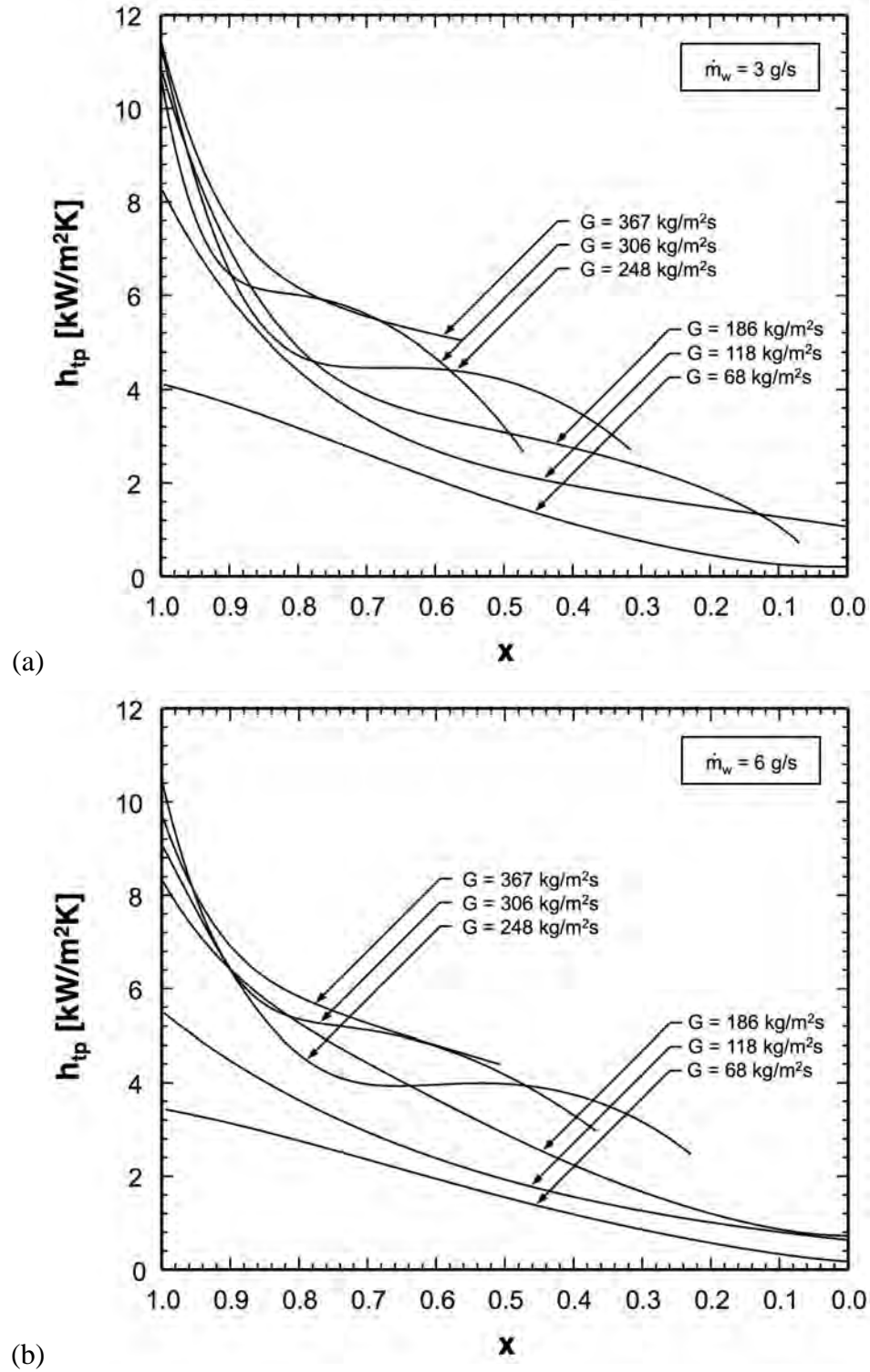


Figure 3.12 Variation of experimentally-determined local FC-72 condensation heat transfer coefficient with thermodynamic equilibrium quality for different FC-72 mass velocities with (a) $\dot{m}_w = 3$ g/s, and (b) $\dot{m}_w = 6$ g/s.

increasing FC-72 mass velocity because of the increased interfacial shear stress and resulting liquid film thinning. On the other hand, increasing the water flow rate increases the flow rate of FC-72 and film thickness, causing a reduction in the heat transfer coefficient.

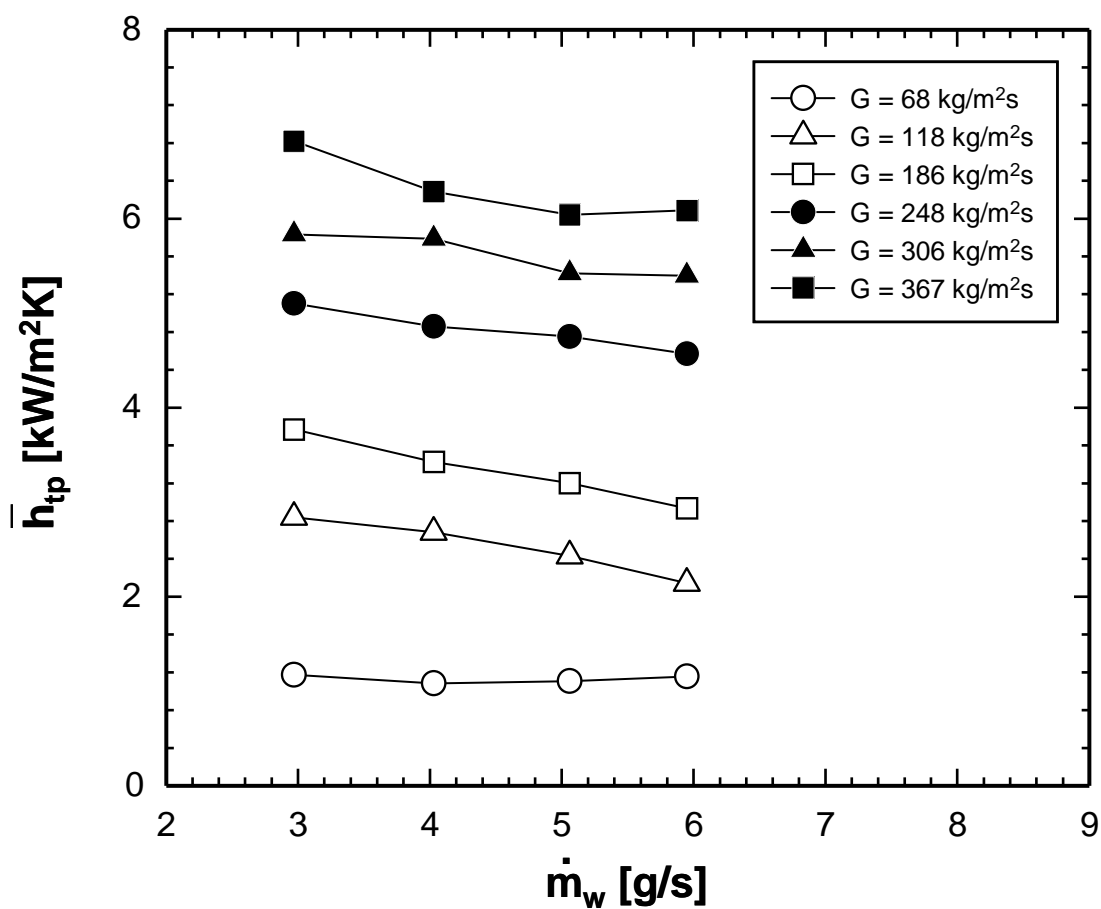


Figure 3.13 Variation of experimentally-determined average FC-72 condensation heat transfer coefficient with coolant mass flow rate for different FC-72 mass velocities.

3.3.3. Comparison with Previous Heat Transfer Correlations

Table 3.4 provides a summary of select condensation heat transfer correlations for the annular flow regime. The predictive accuracy of the correlations is measured by mean absolute error, which is defined as

$$MAE = \frac{1}{M} \sum \frac{|\bar{h}_{tp,pred} - \bar{h}_{tp,exp}|}{\bar{h}_{tp,exp}} \times 100\% . \quad (3.25)$$

The correlations in Table 3.4 can be classified into the following categories: two-phase multiplier-based correlations (Akers *et al.*, 1958; Shah, 1979; Dobson and Chato, 1998), and boundary layer-based correlations (Cavallini and Zecchin, 1974; Moser *et al.*, 1998; Wang *et al.*, 2002; Koyama *et al.*, 2003; Huang *et al.*, 2010). Notice that the correlations of Koyama *et al.* and Huang *et al.* are based on Haraguchi *et al.*'s (1994b) boundary layer-based correlation. Since the correlations in Table 3.4 are intended for uniform circumferential cooling in circular tubes or rectangular channels with four-sided cooling, a multiplier must be adopted when applying these correlations to condensation in rectangular micro-channels with three-sided wall cooling (*i.e.*, with a perfectly insulating top cover plate). Following a technique adopted by Qu and Mudawar (2003b) and Lee and Mudawar (2005) to correct for three-sided heating in flow boiling, the condensation heat transfer coefficient for three-sided cooling is related to that obtained from a correlation for uniform circumferential cooling by the relation

$$h_{tp} = \left(\frac{Nu_3}{Nu_4} \right) h_{tp,cir} , \quad (3.26)$$

where $h_{tp,cir}$ is the heat transfer correlation based on uniform circumferential cooling, and Nu_3 and Nu_4 are Nusselt numbers for thermally developed laminar flow with three-sided and four-sided heat transfer, respectively, (Shah and London, 1978)

$$Nu_3 = 8.235(1 - 1.833\beta + 3.767\beta^2 - 5.814\beta^3 + 5.361\beta^4 - 2.0\beta^5), \quad (3.27a)$$

$$\text{and } Nu_4 = 8.235(1 - 2.042\beta + 3.085\beta^2 - 2.477\beta^3 + 1.058\beta^4 - 0.186\beta^5). \quad (3.27b)$$

Figure 3.14 compares the present FC-72 average condensation heat transfer coefficient data, which correspond mostly to the smooth-annular, wavy-annular, and transition flow regimes, to predictions of five correlations for annular flow condensation in macro-channels. Four of the correlations show good to fair predictions of the present data, while the correlation by Akers *et al.* (1958) highly over-predicts the present data.

Table 3.4 Condensation heat transfer correlations for annular flow regime with corresponding MAE in predicting present experimental data.

Author(s)	Equation	Remarks	MAE [%]
Akers <i>et al.</i> (1958)	$\frac{h_p D_h}{k_f} = \left(\frac{Nu_3}{Nu_4} \right) 0.0265 Re_{eq}^{0.8} Pr_f^{1/3} \text{ for } Re_{eq} > 50000$ $\frac{h_p D_h}{k_f} = \left(\frac{Nu_3}{Nu_4} \right) 5.03 Re_{eq}^{1/3} Pr_f^{1/3} \text{ for } Re_{eq} \leq 50000$ $Re_{eq} = G \left[(1-x) + x \left(\frac{\rho_f}{\rho_g} \right)^{0.5} \right] \frac{D_h}{\mu_f}$	Fluids: R12, propane All flow regimes $60 \leq Nu Pr_f^{-1/3} \leq 400$	160.0
Cavallini and Zecchin (1974)	$\frac{h_p D}{k_f} = \left(\frac{Nu_3}{Nu_4} \right) 0.05 Re_f^{0.8} Pr_f^{0.33} \left[1 + \left(\frac{\rho_f}{\rho_g} \right)^{0.5} \left(\frac{x}{1-x} \right) \right]^{-0.8}$	Fluids: R12, R22, R113 $7000 \leq Re_{fo} \leq 53000$	8.42
Shah (1979)	$\frac{h_p D_h}{k_f} = \left(\frac{Nu_3}{Nu_4} \right) 0.023 Re_{fo}^{0.8} Pr_f^{0.4} \left[(1-x)^{0.8} + \frac{3.8 x^{0.76} (1-x)^{0.04}}{P_R^{0.38}} \right]$	$D = 7\text{-}40$ mm Fluids: water, R11, R12, R22, R113, methanol, ethanol, benzene, toluene, trichloroethylene	13.32
Moser <i>et al.</i> (1998)	$\frac{h_p D_h}{k_f} = \left(\frac{Nu_3}{Nu_4} \right) \frac{0.0994 C_1 Re_f^{C_2} Re_{eq}^{1+0.875 C_1} Pr_f^{0.815}}{(1.58 \ln Re_{eq} - 3.28)(2.58 \ln Re_{eq} + 13.7 Pr_f^{2/3} - 19.1)}$ $C_1 = 0.126 Pr_f^{-0.448}, C_2 = -0.113 Pr_f^{-0.563}, Re_{eq} = \phi_{fo, Friedel}^{8/7} Re_{fo}$	$D = 3.14\text{-}20$ mm Fluids: R11, R12, R125, R22, R134a, R410A 1197 data points	31.79
Dobson and Chato (1998)	$\frac{h_p D_h}{k_f} = \left(\frac{Nu_3}{Nu_4} \right) 0.023 Re_f^{0.8} Pr_f^{0.4} \left(1 + \frac{2.22}{X_u^{0.89}} \right)$ $X_u = \left(\frac{\mu_f}{\mu_g} \right)^{0.1} \left(\frac{1-x}{x} \right)^{0.9} \left(\frac{\nu_f}{\nu_g} \right)^{0.5}$	$D = 3.14\text{-}7.04$ mm Fluids: R12, R22, R134a, R32/R125	10.65
Wang <i>et al.</i> (2002)	$\frac{h_p D_h}{k_f} = \left(\frac{Nu_3}{Nu_4} \right) 0.0274 Pr_f Re_f^{0.6792} x^{0.2208} \frac{\phi_g}{X_u}$ $\phi_g^2 = 1.376 + 8 X_u^{1.665}$	$D_h = 1.46$ mm Fluid: R134a Multi-channel	88.03
Koyama <i>et al.</i> (2003)	$\frac{h_p D_h}{k_f} = \left(\frac{Nu_3}{Nu_4} \right) 0.0152 (1 + 0.6 Pr_f^{0.8}) \frac{\phi_g}{X_u} Re_f^{0.77}$ $\phi_g^2 = 1 + 21 [1 - \exp(-0.319 D_h)] X_u + X_u^2$	$D_h = 0.80, 1.11$ mm Fluid: R134a Multi-channel	31.35
Huang <i>et al.</i> (2010)	$\frac{h_p D}{k_f} = \left(\frac{Nu_3}{Nu_4} \right) 0.0152 (-0.33 + 0.83 Pr_f^{0.8}) \frac{\phi_g}{X_u} Re_f^{0.77}$ $\phi_g^2 = 1 + 0.5 \left\{ \frac{G}{[g D_h \rho_g (\rho_f - \rho_g)]^{0.5}} \right\}^{0.75} X_u^{0.35}$	$D = 1.6, 4.18$ mm Fluids: R410A, R410A/oil	49.23

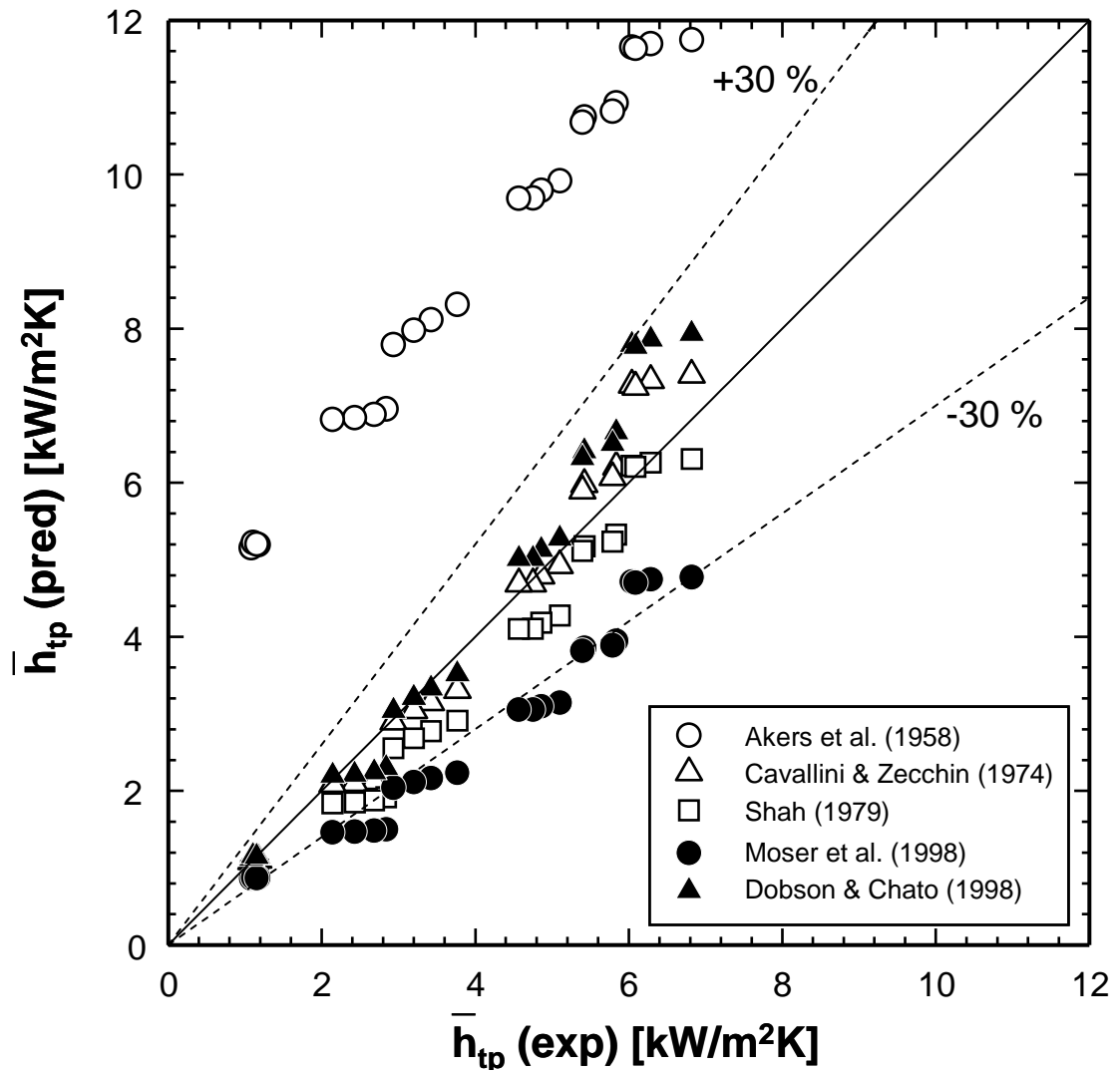


Figure 3.14 Comparison of present experimentally-determined average FC-72 condensation heat transfer coefficient data with predictions of annular flow macro-channel condensation correlations.

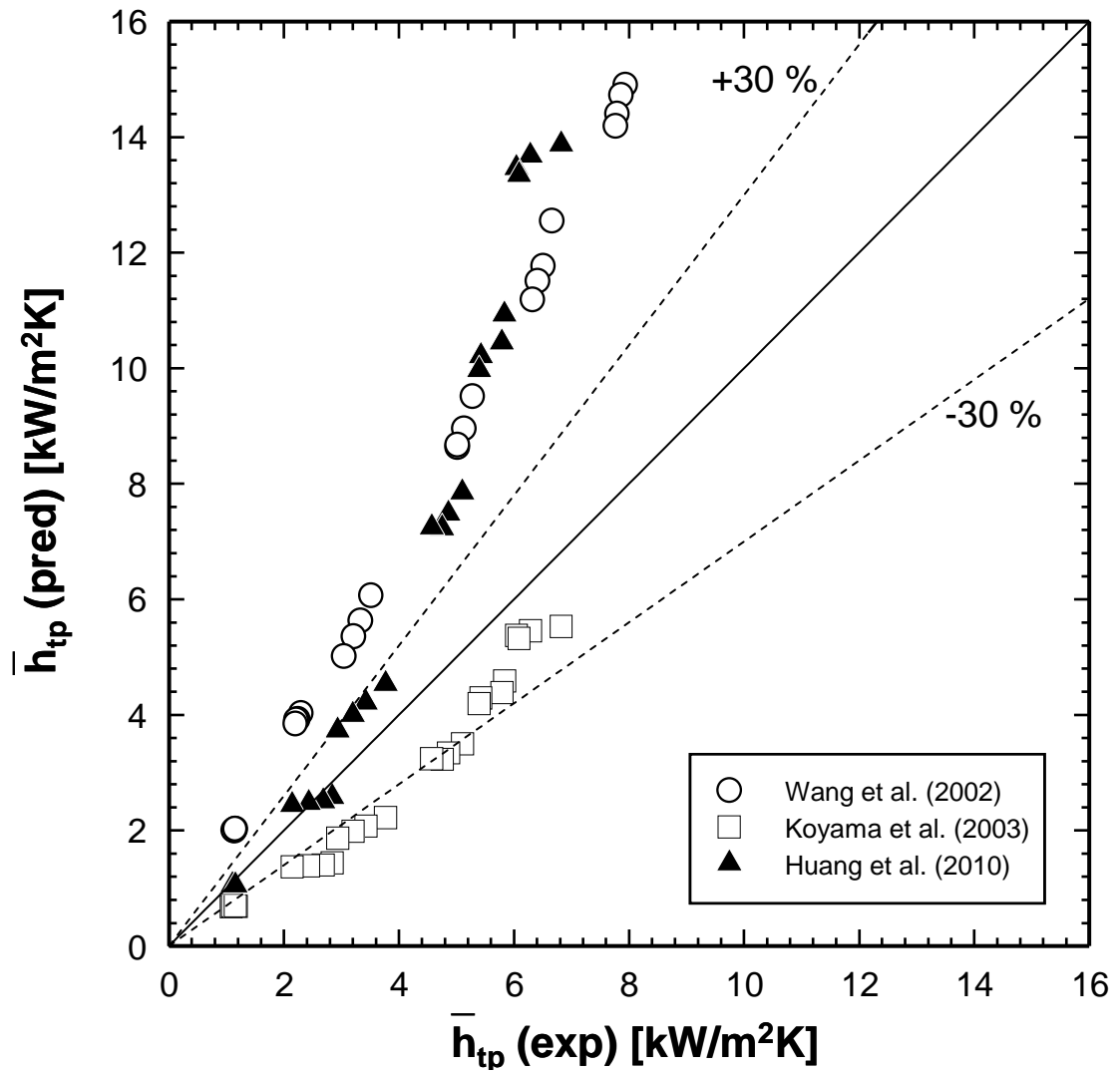


Figure 3.15 Comparison of present experimentally-determined average FC-72 condensation heat transfer coefficient data with predictions of annular flow mini/micro-channel condensation correlations.

Notably, the correlations of Cavallini and Zecchin (1974), Shah (1979), and Dobson and Chato (1998) predict the present FC-72 data with MAEs of 8.42%, 13.32%, and 10.65%, respectively.

Figure 3.15 compares the present FC-72 average condensation heat transfer coefficient data with predictions of annular condensation heat transfer correlations intended for mini/micro-channels. Wang *et al.* (2002) developed a boundary layer-based correlation for annular flow in which the two-phase frictional multiplier and dimensionless boundary layer temperature were evaluated for R134a condensing inside a horizontal rectangular multi-channel with a hydraulic diameter of 1.46 mm. The correlation of Koyama *et al.* (2003) is based on Haraguchi *et al.* (1994b)'s correlation for annular flow, which is derived from boundary layer analysis for condensation of R22, R134a, and R123 inside a horizontal 8.4 mm diameter circular tube and Mishima and Hibiki's (1996) correlation for the two-phase frictional multiplier. Huang *et al.*'s (2010) correlation is based on Haraguchi *et al.*'s (1994a) frictional multiplier correlation for a diameter of 8.4 mm and Haraguchi *et al.*'s (1994b) annular condensation correlation, which Huang *et al.* modified with their own experimental data. Although the correlations in Fig. 3.15 are intended for mini/micro-channels, they show relatively poor agreement with the present FC-72 data compared to the top four macro-channel correlations in Fig. 3.14.

3.3.4. New Heat Transfer Correlation

For a shear-dominated annular condensing flow, the local condensation heat transfer coefficient of liquid film can be obtained from the following relation,

$$h_{tp,cir} = \frac{q_w''}{T_{sat} - T_w} = \frac{\rho_f c_{p,f} u^*}{T_\delta^+}, \quad (3.28)$$

where the friction velocity and dimensionless boundary layer temperature are defined, respectively, as

$$u^* = \sqrt{\tau_w / \rho_f}, \quad (3.29a)$$

and

$$T_\delta^+ = \int_0^{\delta^+} \frac{q_w''}{q_w''} \left(\frac{1}{Pr_f} + \frac{1}{Pr_T} \frac{\varepsilon_m}{\nu_f} \right)^{-1} dy^+. \quad (3.29b)$$

The wall shear stress can be expressed as a function of the single-phase frictional pressure drop based on liquid flow and the two-phase frictional multiplier,

$$\tau_w = -\left(\frac{dP}{dz}\right)_f \frac{D_h}{4} = -\left(\frac{dP}{dz}\right)_f \frac{D_h}{4} \phi_f^2. \quad (3.30)$$

The single-phase frictional pressure drop based on liquid flow can be expressed as

$$-\left(\frac{dP}{dz}\right)_f = \frac{2fG^2(1-x)^2\nu_f}{D_h}. \quad (3.31)$$

The correlation of Mishima and Hibiki (1996), which is based on adiabatic air-water two-phase flow inside 1-4 mm diameter circular tubes, showed good predictions of experimental pressure drop data in small channels such as circular tubes (Cavallini *et al.*, 2005), trapezoidal channels (Quan *et al.*, 2008), and rectangular channels (Koyama *et al.*, 2003; Qu and Mudawar, 2003a; Park and Hrnjak, 2009). Mishima and Hibiki's correlation also provided the best predictions of the present FC-72 pressure drop data (MAE of 27.15%) among all the separated flow correlations examined in Chapter 3.2. Therefore, the two-phase frictional multiplier in Eq. (3.30) is based on Mishima and Hibiki's correlation

$$\phi_f^2 = 1 + \frac{21[1 - \exp(-0.319D_h)]}{X} + \frac{1}{X^2}, \quad D_h[mm]. \quad (3.32)$$

It was shown earlier that most macro-channel correlations intended for circular tubes provide good agreement with the present square micro-channel condensation heat transfer data. This suggests that, unlike non-annular flow regimes, there are no major differences in condensation behavior between small and large channels in the annular regime. Furthermore, the low surface tension of FC-72 tends to maintain nearly uniform liquid film thickness along the inner walls of the square channel, barely affected by corner effects. Therefore, the following relation by Haraguchi *et al.* (1994b) for condensation of R22, R134a, and R123 inside an 8.4-mm horizontal circular tube with $G = 200 - 400 \text{ kg/m}^2\text{s}$ is used for determination of the dimensionless boundary layer temperature in the present square micro-channel,

$$T_\delta^+ = (0.1 + 0.06\text{Pr}_f^{0.8})^{-1} \text{Pr}_f \text{Re}_f^{0.13}. \quad (3.33)$$

Substituting Eqs. (3.29) - (3.33) into Eq. (3.28), and accounting for the effects of three-sided cooling via Eq. (3.26), the local heat transfer coefficient for annular condensation with three-sided cooling can be expressed as

$$h_{tp} = \left(\frac{Nu_3}{Nu_4} \right) (0.1 + 0.06 Pr_f^{0.8}) Pr_f^{-1} Re_f^{-0.13} c_{p,f} \sqrt{\frac{f G^2 (1-x)^2}{2} \left\{ 1 + \frac{21[1 - \exp(-0.319 D_h)]}{X} + \frac{1}{X^2} \right\}}, \quad (3.34)$$

where X is the Martinelli parameter. The Fanning friction factor based on liquid flow can be determined from (Shah and London, 1978; Incropera and Dewitt, 2002).

$$f Re_f = 24 (1 - 1.3553 \beta + 1.9467 \beta^2 - 1.7012 \beta^3 + 0.9564 \beta^4 - 0.2537 \beta^5) \quad \text{for } Re_f < 2,000, \quad (3.35a)$$

$$f = 0.079 Re_f^{-0.25} \quad \text{for } 2,000 \leq Re_f < 20,000, \quad (3.35b)$$

$$f = 0.046 Re_f^{-0.2} \quad \text{for } Re_f \geq 20,000, \text{ and } Re_f = G(1-x)D_h/\mu_f. \quad (3.35c)$$

Figure 3.16 shows the new condensation heat transfer correlation accurately predicts the present FC-72 average heat transfer data with a mean absolute error of 9.0%, although some low mass velocity data include non-annular data.

Figure 3.17 compares the present local heat transfer coefficient data for $G = 306 \text{ kg/m}^2\text{s}$ and $\dot{m}_w = 5 \text{ g/s}$ with predictions of the new correlation, Eq. (3.34), and previous correlations given in Table 3.4. The new correlation shows best predictions of the present data both in magnitude and trend. The correlations of Akers *et al.* (1958), Wang *et al.* (2002) and Huang *et al.* (2010) over-predict the data by an appreciable margin. While the Shah (1979) correlation predicts an unrealistic trend of decreasing heat transfer coefficient in the high vapor quality region where the film is thinnest, this correlation provides good overall prediction of the average heat transfer coefficient, evidenced by a MAE of 13.32%.

In order to further assess the accuracy of the new annular condensation heat transfer correlation, a total 923 data points for condensation in mini/micro-channels were amassed from eight sources which are described in Table 3.5. Figure 3.18 shows all 923 data points in a plot of Martinelli parameter based on turbulent liquid-turbulent vapor versus modified Weber number, which is defined by Soliman (1986) as

$$We^* = 2.45 \frac{Re_g^{0.64}}{Su_g^{0.3} (1 + 1.09 X_{tt}^{0.039})^{0.4}} \quad \text{for } Re_f \leq 1250, \quad (3.36a)$$

$$\text{and} \quad We^* = 0.85 \frac{Re_g^{0.79} X_{tt}^{0.157}}{Su_g^{0.3} (1 + 1.09 X_{tt}^{0.039})^{0.4}} \left[\left(\frac{\mu_g}{\mu_f} \right)^2 \left(\frac{\nu_g}{\nu_f} \right) \right]^{0.084} \quad \text{for } Re_f > 1250, \quad (3.36b)$$

where the Suratman number, Su_g , and the turbulent-turbulent Martinelli parameter, X_{tt} , are defined as

$$Su_g = \frac{\rho_g \sigma D}{\mu_g^2}, \quad (3.37a)$$

and

$$X_{tt} = \left(\frac{\mu_f}{\mu_g} \right)^{0.1} \left(\frac{1-x}{x} \right)^{0.9} \left(\frac{\nu_f}{\nu_g} \right)^{0.5}, \quad (3.37b)$$

respectively (Soliman, 1986). The vapor and liquid Reynolds numbers of the 923 data points are also symbolized in Fig. 3.18 with a transition Reynolds number value of 2000. Although all the data are plotted versus the turbulent-turbulent Martinelli parameter, they are classified clearly into the following four different zones by two fitted lines of $We^* = 3$ and $We^* = 6.3X_{tt}^{-0.68}$,

$$Re_f < 2000 \text{ and } Re_g < 2000: We^* < 3 \text{ and } We^* < 6.3X_{tt}^{-0.68}. \quad (3.38a)$$

$$Re_f < 2000 \text{ and } Re_g > 2000: 3 < We^* < 6.3X_{tt}^{-0.68}. \quad (3.38b)$$

$$Re_f > 2000 \text{ and } Re_g < 2000: 6.3X_{tt}^{-0.68} < We^* < 3. \quad (3.38c)$$

$$Re_f > 2000 \text{ and } Re_g > 2000: We^* > 3 \text{ and } We^* > 6.3X_{tt}^{-0.68}. \quad (3.38d)$$

Table 3.5 Database for two-phase condensation heat transfer coefficient in mini/micro-channels.

Author(s)	D_h [mm]	Fluid(s)	Geometry*	All data / annular data ⁺
Hirofumi and Webb (1995)	0.96 - 2.13	R134a	C/R multi	62 / 61
Zhang (1998)	2.13, 3.25	R134a, R22, R404A	C single/multi	66 / 65
Yan and Lin (1999)	2.0	R134a	C multi	78 / 60
Wang <i>et al.</i> (2002)	1.46	R134a	R multi	410 / 268
Cavallini <i>et al.</i> (2005)	1.4	R134a, R410A	R multi	59 / 56
Park and Hrnjak (2009)	0.89	CO ₂	C multi	52 / 37
Matkovic <i>et al.</i> (2009)	0.96	R134a, R32	C single	161 / 131
Huang <i>et al.</i> (2010)	1.6, 4.18	R410A	C single	35 / 35

* C: circular, R: rectangular, ⁺annular data (smooth-annular, wavy-annular and transition) correspond to $We^* > 7X_{tt}^{0.2}$.

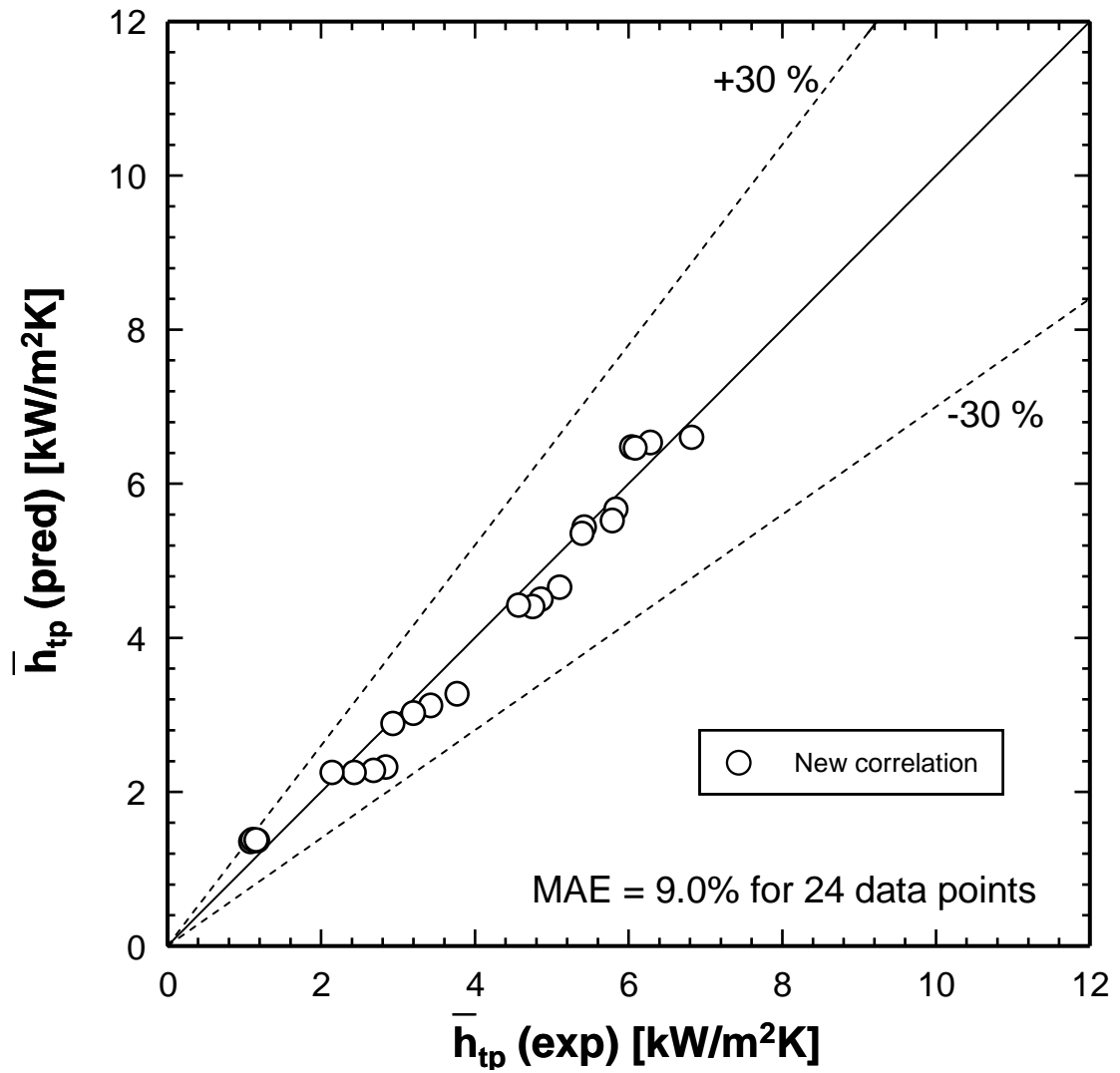


Figure 3.16 Comparison of present experimentally-determined average FC-72 condensation heat transfer coefficient data with predictions of the new annular condensation correlation.

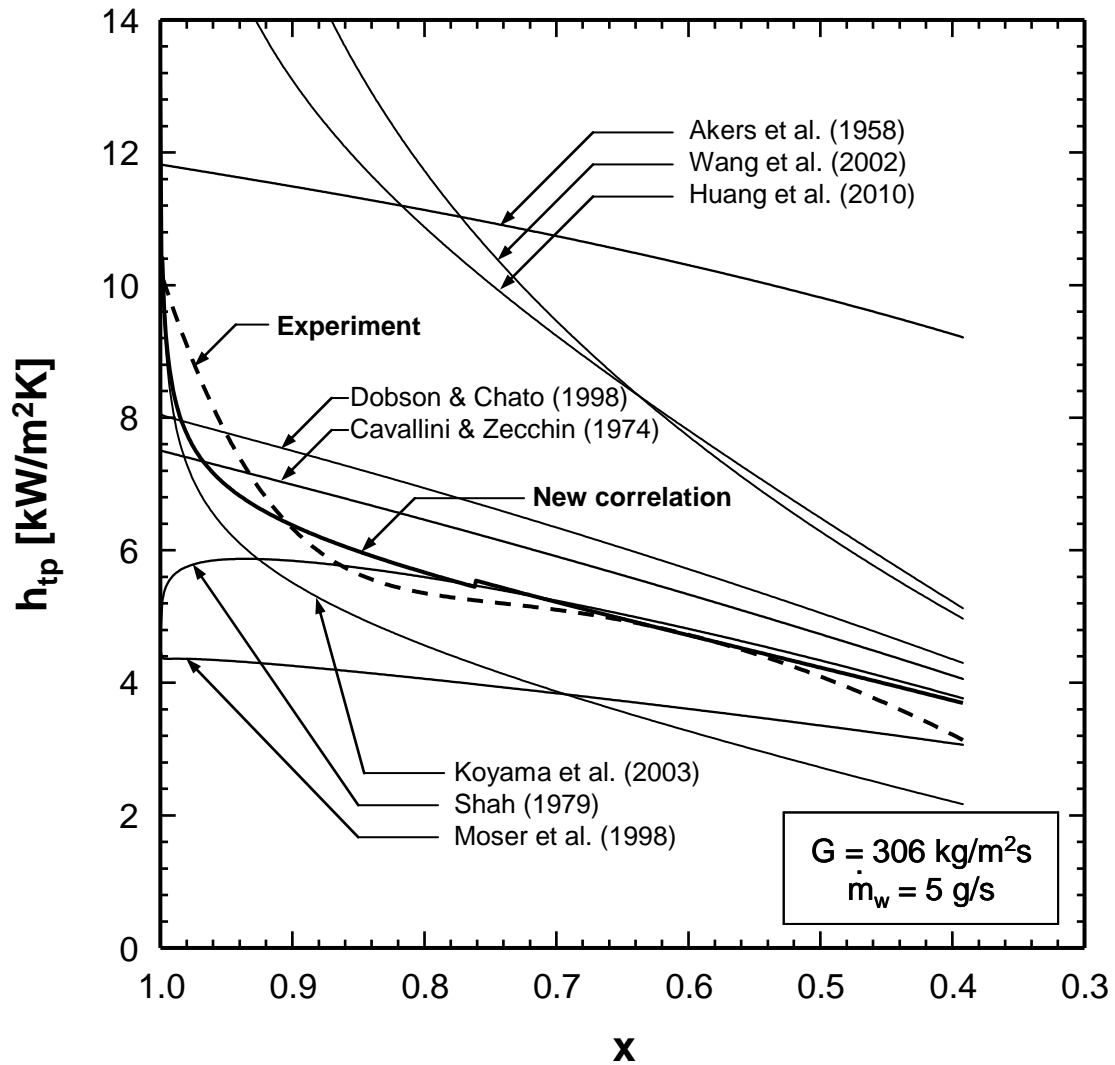


Figure 3.17 Variation of present experimentally-determined local FC-72 condensation heat transfer coefficient data with thermodynamic equilibrium quality for $G = 306 \text{ kg/m}^2\text{s}$ and $\dot{m}_w = 5 \text{ g/s}$ compared to predictions of new correlation and previous annular condensation correlations.

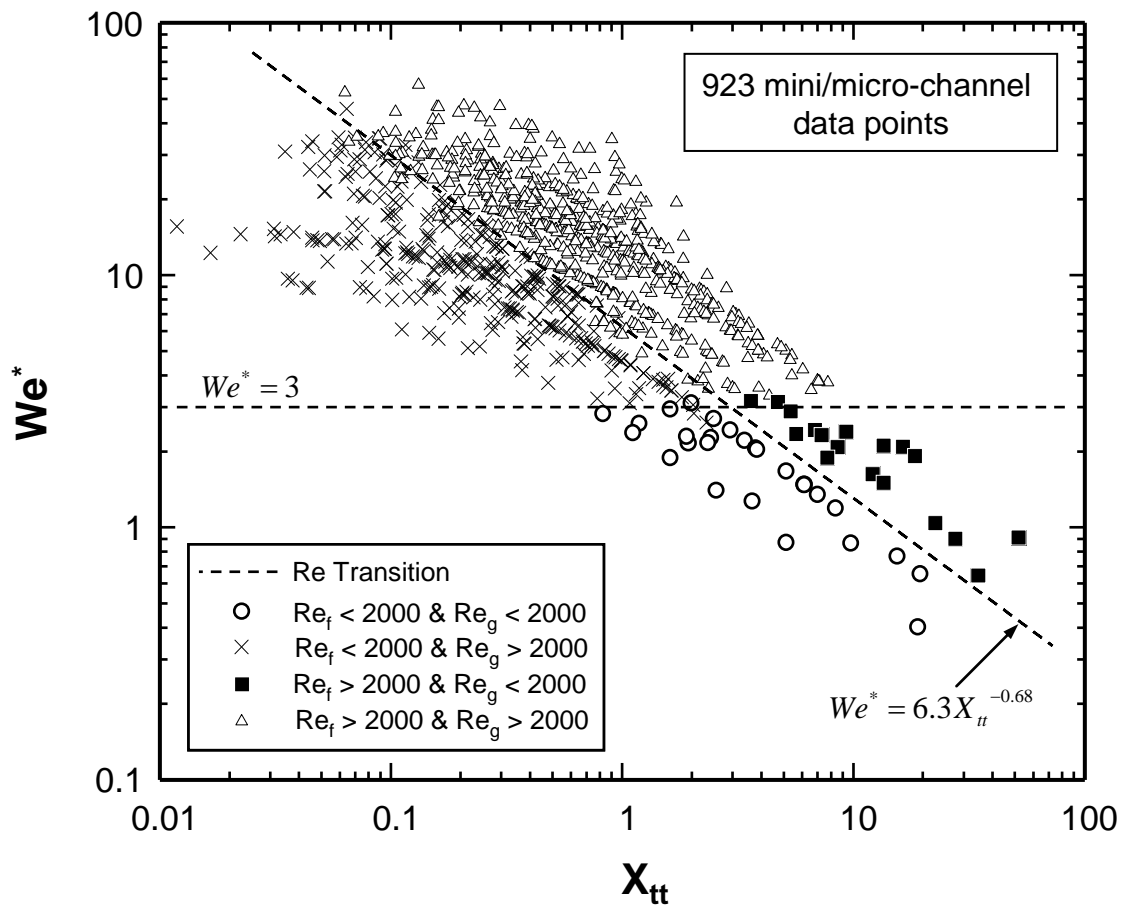


Figure 3.18 Reynolds number transition lines based on 923 mini/micro-channel data points from eight sources.

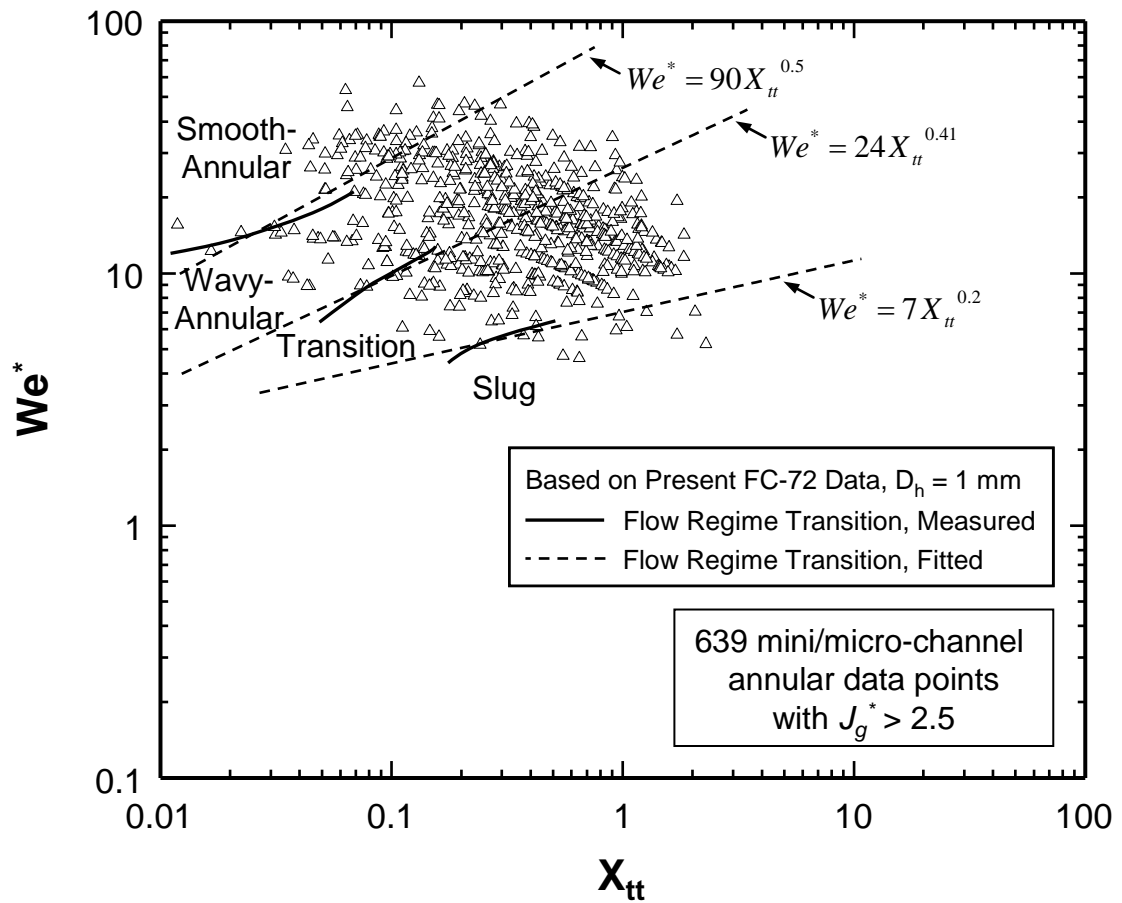


Figure 3.19 Proposed flow regime map based on present FC-72 flow visualization experiments in square micro-channels with $D_h = 1$ mm plotted alongside 639 mini/micro-channel data points corresponding to $J_g^* > 2.5$ from eight sources.

Based on the FC-72 flow visualization data presented in Chapter 3.1, the following lines are fitted for boundaries between different flow regimes:

$$\text{Smooth-annular to wavy-annular: } We^* = 90X_{tt}^{0.5}. \quad (3.39a)$$

$$\text{Wavy-annular to transition: } We^* = 24X_{tt}^{0.41}. \quad (3.39b)$$

$$\text{Transition to slug: } We^* = 7X_{tt}^{0.2}. \quad (3.39c)$$

Cavallini *et al.* (2002) proposed that the flow is annular for $J_g^* > 2.5$, and intermittent and slug for $J_g^* < 2.5$, based on previous flow regime maps, where the dimensionless superficial vapor velocity is defined as

$$J_g^* = Gx / \sqrt{\rho_g(\rho_g - \rho_g)}gD. \quad (3.40)$$

Figure 3.19 shows 639 mini/micro-channel annular data points from the eight aforementioned sources excluding all data with dimensionless superficial gas velocities below 2.5. Although a few data points do appear for $We^* < 7X_{tt}^{0.2}$, the boundary line between the transition and slug regimes from the present study is in general agreement with that from Cavallini *et al.*.

Table 3.6 Comparison of mini/micro-channel database for annular flow (smooth-annular, wavy-annular and transition) with predictions of annular condensation heat transfer correlations.

Author(s)	Mean absolute error [%]								
	Akers <i>et al.</i> (1958)	Cavallini and Zecchin (1974)	Shah (1979)	Moser <i>et al.</i> (1998)	Dobson and Chato (1998)	Wang <i>et al.</i> (2002)	Koyama <i>et al.</i> (2003)	Huang <i>et al.</i> (2010)	New correl.
Hirofumi and Webb (1995)	89.1	84.9	72.4	39.1	77.9	12.3	30.2	30.0	29.3
Zhang (1998)	27.6	32.6	22.5	10.6	27.8	33.7	50.4	36.6	15.5
Yan and Lin (1999)	84.5	16.8	12.0	11.8	16.4	21.0	48.3	39.6	13.4
Wang <i>et al.</i> (2002)	27.2	59.8	45.8	22.2	46.5	14.1	45.5	38.4	16.8
Cavallini <i>et al.</i> (2005)	53.3	33.5	23.7	12.6	28.7	33.6	49.9	28.8	17.1
Park and Hrnjak (2009)	178.3	73.6	54.6	40.8	67.7	14.7	30.0	19.7	11.0
Matkovic <i>et al.</i> (2009)	59.6	29.9	18.8	14.0	26.8	34.5	48.4	22.4	21.6
Huang <i>et al.</i> (2010)	12.8	19.1	15.2	15.8	17.4	48.2	57.3	58.9	20.8
Total	90.1	47.0	35.4	20.1	39.6	23.3	45.5	34.0	18.3

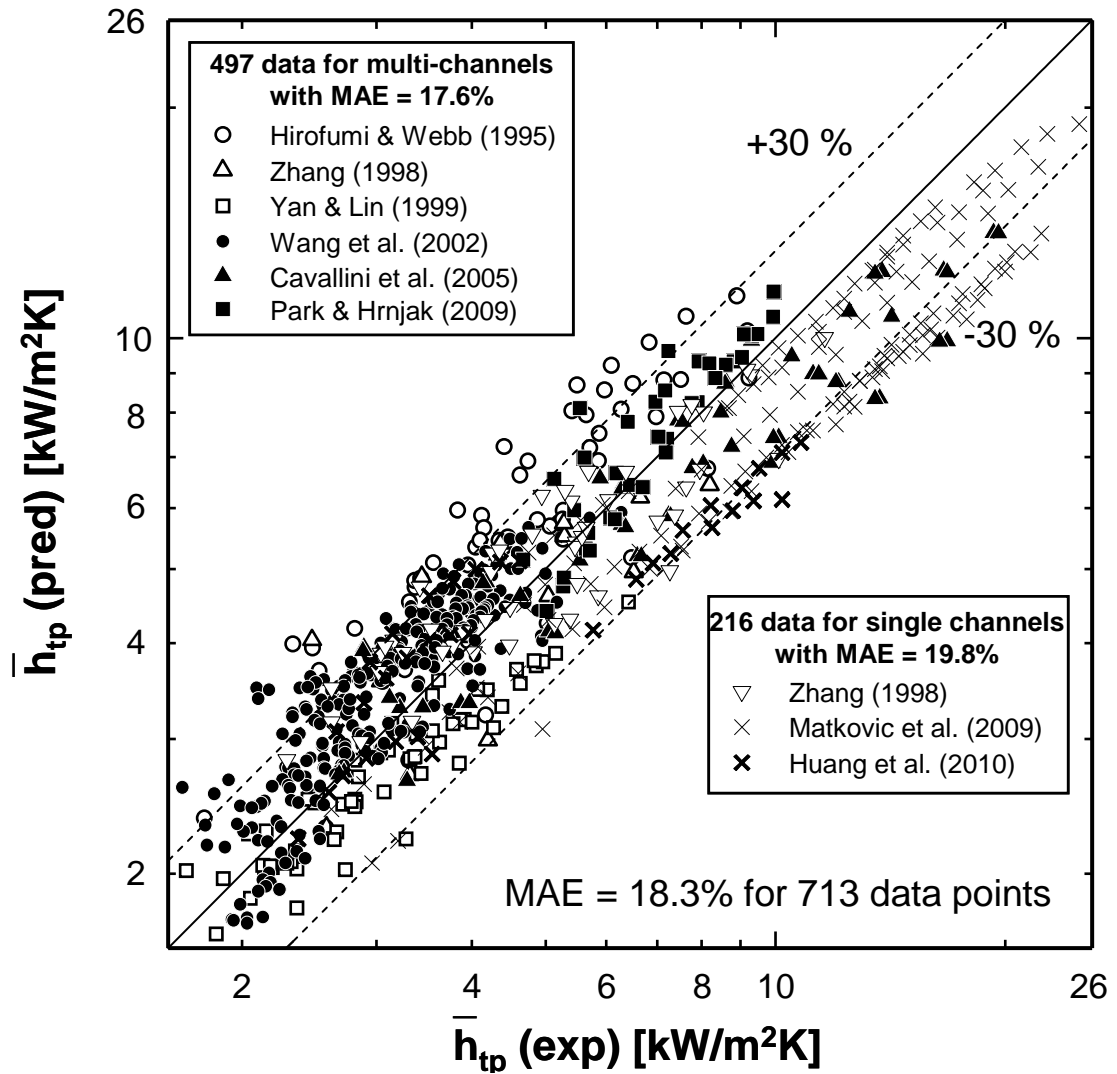


Figure 3.20 Comparison of predictions of new annular condensation heat transfer correlation with prior experimental mini/micro-channel data.

In order to isolate data corresponding to flow regimes with a clearly identifiable annular liquid film (smooth-annular, wavy-annular and transition) to assess the accuracy of the new correlation, all 210 data points (from a total of 923 data points) that correspond to $We^* < 7X_{tt}^{0.2}$ are excluded. Table 3.6 shows both the total number of data points from each of the eight previous sources as well as corresponding number of data points that are deemed to fall into the present broad classification of annular flows.

Table 3.6 compares the predictive accuracy of previous correlations and the new annular flow correlation against the mini/micro-channel data that fall into the broad classification of annular flows. Although the correlations of Moser *et al.* (1998) and Wang *et al.* (2002) provide good predictive capability against the entire annular database, with MAEs of 20.1% and 23.3%, respectively, they are far less accurate in predicting the present FC-72 data, with corresponding MAEs of 31.8% and 88.0%, respectively. The new annular heat transfer correlation accurately predicts each of the eight previous sources with a MAE less than 30%.

Figure 3.20 shows the new annular correlation provides the best prediction of 713 annular mini/micro-channels data points with an overall MAE of 18.3% (17.6% for multi-channels and 19.8% for single channels). Most data points are shown falling within $\pm 30\%$ of predicted values.

CHAPTER 4. THEORETICAL MODEL

4.1. Model Development

4.1.1. Key Findings from Flow Visualization Experiments

Qu and Mudawar (2003a) showed that droplet entrainment and deposition play a crucial role in mass, momentum and heat transfer in annular evaporating micro-channel flows. As shown in Fig. 3.8(a), droplets are formed by shattering of liquid from the micro-channel's upstream. However, the flow visualization results from the present authors' study have shown that no droplets are formed in the annular region of micro-channel condensing flow (refer to Chapter 3.1). Therefore, these effects are neglected in the development of the present theoretical annular flow model.

The authors' recent micro-channel condensation studies also showed that the annular region consists of two distinct sub-regimes. The upstream, smooth-annular regime features a thin smooth liquid film. However, the annular film in the wavy-annular regime is marred by interfacial waves. Nonetheless, these waves were fairly sinusoidal in profile and do not shatter or produce entrained droplets, nor do they evolve into large waves as is commonly observed in annular macro-channel flows.

4.1.2. Model Assumptions

A key challenge in developing the theoretical model is determining the distribution of liquid along the channel's circumference. Gravity effects are negligible in micro-channels compared to macro-channels, given the large shear stresses encountered in the former. This precludes any preferential accumulation of liquid based on orientation of the flow relative to gravity. However, the surface tension of the working fluid can have a significant influence on the liquid distribution. Figure 3.8(b) contrasts the liquid distribution in a rectangular micro-channel for the case of a very low

surface tension fluid such as FC-72 (0.0084 N/m at 1 bar) compared to that of a relatively high surface tension fluid such as water (0.059 N/m at 1 bar). Notice how low surface tension fluids, which include most dielectric fluids used in electronic cooling applications, tend to maintain a nearly uniform liquid film thickness around the channel circumference. The present study will be based on this assumption since it concerns mostly low surface tension electronic cooling fluids.

Figure 4.1 provides a schematic representation of liquid film condensation in a rectangular micro-channel with three-sided wall cooling and relevant nomenclature used in the development of the annular condensation model. Following are key assumptions of the model:

- (1) The annular condensing flow is steady, incompressible, and concurrent.
- (2) Gravitational effects are negligible.
- (3) Both entrainment and deposition of liquid droplets are negligible.
- (4) Pressure is uniform across the micro-channel's cross-sectional area.
- (5) Thermophysical properties are based on local saturation pressure.
- (6) Mean vapor velocity is assumed across the vapor core's cross-sectional area.
- (7) Mass transfer occurs only at the interface between the vapor core and the liquid film.
- (8) The liquid film interface is smooth.
- (9) Liquid film thickness is uniform around the channel's circumference.
- (10) Axial momentum changes in the liquid film are negligible.
- (11) The liquid film flow can be laminar or turbulent.
- (12) The circumferential heat flux is uniform along the vapor-liquid interface.

The boundary condition of base heat flux, q''_{base} , beneath the micro-channels is determined from local temperature measurements obtained by arrays of thermocouples embedded in two separate planes in the copper block. The local temperatures in the copper block are fitted to a third- or fourth-order polynomial function of stream-wise distance, and the corresponding variations of micro-channel base heat flux, q''_{base} , and base temperature, T_{base} , are obtained by assuming one-dimensional heat conduction along the direction perpendicular to the top surface of the copper block (Kim and Mudawar,

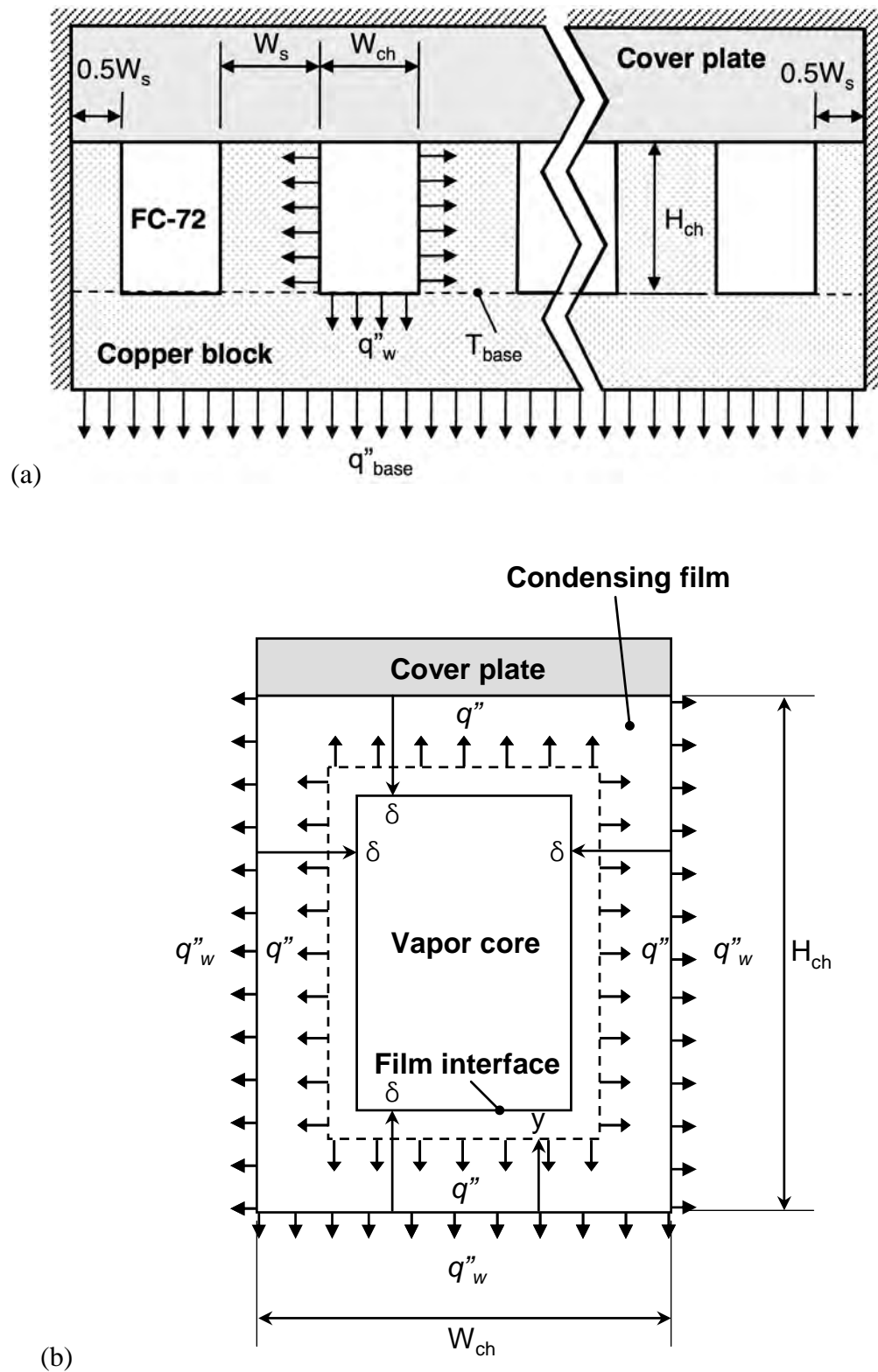


Figure 4.1 Schematic representations of (a) condenser with rectangular micro-channels and (b) liquid film condensation in micro-channel with three-sided wall cooling.

2010a). In the superheated vapor region near the channel inlet, sensible heat loss of FC-72 can be calculated from the following energy balance,

$$q''_{base} (W_{ch} + W_s) \Delta z = \frac{\dot{m}}{N} c_{p,g} \Delta T_f. \quad (4.1)$$

The onset of two-phase condensation is calculated to occur at the distance from the channel inlet where the fluid temperature reaches the saturation temperature corresponding to the local pressure. The quality in the superheated region can be determined from

$$x = 1 + \frac{c_{p,g} (T_f - T_{sat})}{h_{fg}}, \quad (4.2)$$

where T_f and T_{sat} are the local bulk fluid and saturation temperatures, respectively.

4.1.3. Control Volume Analysis

To develop a theoretical control-volume-based model, mass and momentum conservation are first applied to control volumes encompassing the liquid film and the vapor core separately. For the two-phase condensing region, mass conservation for the liquid film and the vapor core can be expressed, respectively, as

$$\frac{d\dot{m}_f}{dz} - \Gamma_{fg} = 0, \quad (4.3)$$

and

$$\frac{d\dot{m}_g}{dz} + \Gamma_{fg} = 0, \quad (4.4)$$

where the mass flow rates of the liquid film and the vapor core, and the rate of mass transfer due to condensation are defined, respectively, as

$$\dot{m}_f = 2\rho_f \int_0^\delta u_f [(H_{ch} - 2y) + (W_{ch} - 2y)] dy, \quad (4.5)$$

$$\dot{m}_g = \rho_g \bar{u}_g (W_{ch} - 2\delta)(H_{ch} - 2\delta), \quad (4.6)$$

and

$$\Gamma_{fg} = \frac{q''_w (2H_{ch} + W_{ch})}{h_{fg}} = \frac{q''_{base} (W_{ch} + W_s)}{h_{fg}}. \quad (4.7)$$

Applying momentum conservation to the liquid film element illustrated in Fig. 4.2(a) yields

$$-\Gamma_{fg} u_i \Delta z = PA_{f,*} - \left(P + \frac{dP}{dz} \Delta z \right) A_{f,*} - \tau_{f,y} \Delta z + \tau_i P_{f,\delta} \Delta z, \quad (4.8)$$

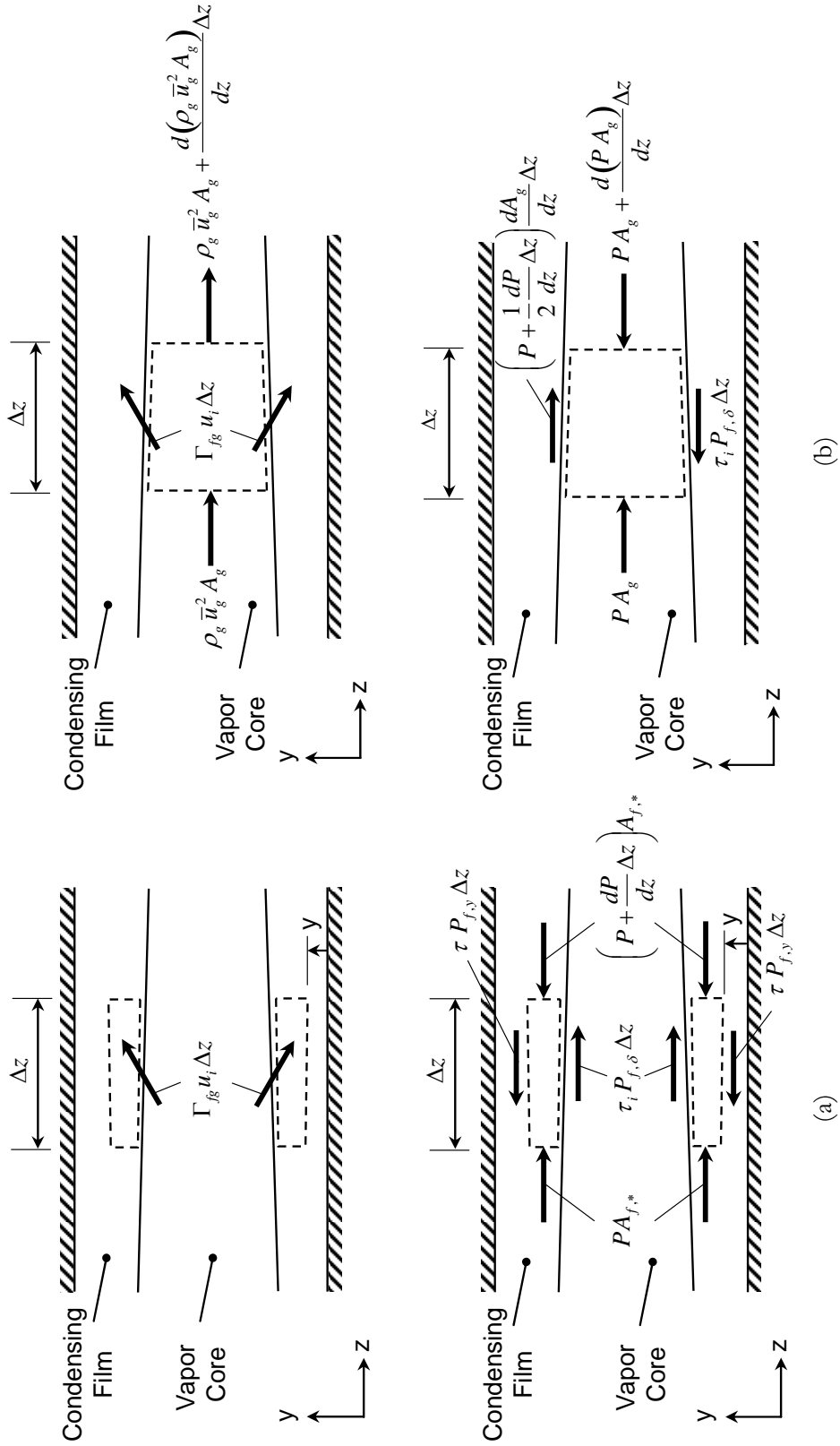


Figure 4.2 Momentum and force components for (a) liquid film control volume and (b) vapor core control volume.

where the flow area, $A_{f,*}$, local perimeter, $P_{f,y}$, and interfacial perimeter, $P_{f,\delta}$, can be expressed, respectively, as

$$A_{f,*} = (H_{ch} - 2y)(W_{ch} - 2y) - (H_{ch} - 2\delta)(W_{ch} - 2\delta), \quad (4.9)$$

$$P_{f,y} = 2[(H_{ch} - 2y) + (W_{ch} - 2y)], \quad (4.10)$$

and

$$P_{f,\delta} = 2[(H_{ch} - 2\delta) + (W_{ch} - 2\delta)]. \quad (4.11)$$

Rearranging Eq. (4.8) gives

$$\tau = \left(-\frac{dP}{dz} \right) \frac{A_{f,*}}{P_{f,y}} + \frac{\tau_i P_{f,\delta} + \Gamma_{fg} u_i}{P_{f,y}}. \quad (4.12)$$

Allowing for turbulence in the condensing film, the local shear stress in the film can be expressed as

$$\tau = \mu_f \left(1 + \frac{\varepsilon_m}{\nu_f} \right) \frac{du_f}{dy}, \quad (4.13)$$

where ε_m is the eddy momentum diffusivity. Substituting Eq. (4.13) into Eq. (4.12) and integrating yield the velocity profile across the liquid film.

$$u_f(y) = \frac{\delta}{\mu_f} \left(-\frac{dP}{dz} \right) \int_0^{y/\delta} \frac{A_{f,*}}{P_{f,y}} \left(1 + \frac{\varepsilon_m}{\nu_f} \right)^{-1} d\left(\frac{y}{\delta}\right) + \frac{\delta}{\mu_f} (\tau_i P_{f,\delta} + \Gamma_{fg} u_i) \int_0^{y/\delta} \frac{1}{P_{f,y}} \left(1 + \frac{\varepsilon_m}{\nu_f} \right)^{-1} d\left(\frac{y}{\delta}\right). \quad (4.14)$$

The interfacial velocity can be determined by setting $y = \delta$ in Eq. (4.14).

$$u_i = \frac{\left(-\frac{dP}{dz} \right) \int_0^1 \frac{A_{f,*}}{P_{f,y}} \left(1 + \frac{\varepsilon_m}{\nu_f} \right)^{-1} d\left(\frac{y}{\delta}\right) + \tau_i P_{f,\delta} \int_0^1 \frac{1}{P_{f,y}} \left(1 + \frac{\varepsilon_m}{\nu_f} \right)^{-1} d\left(\frac{y}{\delta}\right)}{\frac{\mu_f}{\delta} - \Gamma_{fg} \int_0^1 \frac{1}{P_{f,y}} \left(1 + \frac{\varepsilon_m}{\nu_f} \right)^{-1} d\left(\frac{y}{\delta}\right)}. \quad (4.15)$$

Substituting Eq. (4.14) into Eq. (4.5) yields the following relation for pressure gradient,

$$-\frac{dP}{dz} = \frac{\frac{\mu_f \dot{m}_f}{\rho_f \delta^2} - (\tau_i P_{f,\delta} + \Gamma_{fg} u_i) \int_0^1 \left[P_{f,y} \int_0^{y/\delta} \frac{1}{P_{f,y}} \left(1 + \frac{\varepsilon_m}{\nu_f} \right)^{-1} d\left(\frac{y}{\delta}\right) \right] d\left(\frac{y}{\delta}\right)}{\int_0^1 \left[P_{f,y} \int_0^{y/\delta} \frac{A_{f,*}}{P_{f,y}} \left(1 + \frac{\varepsilon_m}{\nu_f} \right)^{-1} d\left(\frac{y}{\delta}\right) \right] d\left(\frac{y}{\delta}\right)}. \quad (4.16)$$

The double integral terms in the above equation can be expanded as follows,

$$\int_0^1 \left[P_{f,y} \int_0^{y/\delta} F(y) d\left(\frac{y}{\delta}\right) \right] d\left(\frac{y}{\delta}\right) =$$

$$2(H_{ch} + W_{ch}) \int_0^1 \left[\int_0^{y/\delta} F(y) d\left(\frac{y}{\delta}\right) \right] d\left(\frac{y}{\delta}\right) + 4\delta \int_0^1 \left[\left(\frac{y}{\delta}\right)^2 - 1 \right] F(y) d\left(\frac{y}{\delta}\right). \quad (4.17)$$

Applying momentum conservation to a rectangular element of the vapor core illustrated in Fig. 4.2(b) yields

$$\rho_g \bar{u}_g^2 A_g + \frac{d(\rho_g \bar{u}_g^2 A_g)}{dz} \Delta z - \rho_g \bar{u}_g^2 A_g + \Gamma_{fg} u_i \Delta z =$$

$$PA_g - \left[PA_g + \frac{d(PA_g)}{dz} \Delta z \right] - \tau_i P_{f,\delta} \Delta z + \left(P + \frac{1}{2} \frac{dP}{dz} \Delta z \right) \frac{dA_g}{dz} \Delta z. \quad (4.18)$$

Rearranging Eq. (4.18) and neglecting the second order term of Δz yield the following relation for interfacial shear stress between the condensing film and vapor core,

$$\tau_i = \frac{1}{P_{f,\delta}} \left[A_g \left(-\frac{dP}{dz} \right) - \frac{d(\rho_g \bar{u}_g^2 A_g)}{dz} - \Gamma_{fg} u_i \right], \quad (4.19)$$

where the flow area of the vapor core is $A_g = (W_{ch} - 2\delta)(H_{ch} - 2\delta)$.

The interfacial shear stress is the result of velocity differences between the vapor core and interface, modified by the influence of interfacial momentum transfer due to condensation along the vapor-liquid interface due to condensation; the later is obtained using a treatment by Wallis (1969),

$$\tau_i = f_i \left[\frac{1}{2} \rho_g (\bar{u}_g - u_i)^2 \right] + \frac{(\bar{u}_g - u_i) \Gamma_{fg}}{2P_{f,\delta}}. \quad (4.20)$$

The interfacial friction factor, f_i , can be determined from relations by Shah and London (1978),

$$f_i \text{Re}_c = 24 \left(1 - 1.3553\beta_c + 1.9467\beta_c^2 - 1.7012\beta_c^3 + 0.9564\beta_c^4 - 0.2537\beta_c^5 \right)$$

for $\text{Re}_c < 2,000$, (4.21a)

$$f_i = 0.079 \text{Re}_c^{-0.25} \text{ for } 2,000 \leq \text{Re}_c < 20,000, \quad (4.21b)$$

and (4.21c)

$$f_i = 0.046 \text{Re}_c^{-0.2} \text{ for } \text{Re}_c \geq 20,000,$$

where β_c , Re_c , and $D_{h,c}$ are the aspect ratio, effective Reynolds number, and hydraulic diameter of the vapor core, respectively, which are given by

$$\beta_c = \frac{W_{ch} - 2\delta}{H_{ch} - 2\delta}, \quad (4.22)$$

$$\text{Re}_c = \frac{\rho_g (\bar{u}_g - u_i) D_{h,c}}{\mu_g}, \quad (4.23)$$

and

$$D_{h,c} = \frac{4A_g}{P_{f,\delta}}. \quad (4.24)$$

4.1.4. Turbulence Model

Equation (4.13) can be expressed in nondimensional form as

$$\frac{\tau}{\tau_w} = \left(1 + \frac{\varepsilon_m}{\nu_f} \right) \frac{du^+}{dy^+}, \quad (4.25)$$

where

$$u^+ = \frac{u}{u^*}, \quad (4.26)$$

$$y^+ = \frac{yu^*}{\nu_f}, \quad (4.27)$$

and

$$u^* = \left(\frac{\tau_w}{\rho_f} \right)^{0.5}. \quad (4.28)$$

Based on the Prandtl mixing length theory, the eddy diffusivity can be expressed in terms of the turbulent mixing length according to the relation

$$\frac{\varepsilon_m}{\nu_f} = l^{+2} \frac{du^+}{dy^+}. \quad (4.29)$$

A turbulent mixing length relation originally proposed by Van Driest (1956) was modified by Kays (1972, 1980) to the following form,

$$l^+ = K y^+ \left[1 - \exp \left(- \sqrt{\frac{\tau}{\tau_w}} \frac{y^+}{A^+} \right) \right], \quad (4.30)$$

where the Von-Karman constant of $K = 0.4$ is used for all subsequent calculations, and the constant A^+ is given by Kays (1972, 1980),

$$A^+ = 26 \left(1 + 30.18 \mu_f \rho_f^{-0.5} \tau_w^{-1.5} \frac{dP}{dz} \right)^{-1}. \quad (4.31)$$

Substituting Eqs. (4.25) and (4.30) into Eq. (4.29) yields the following eddy diffusivity profile,

$$\frac{\varepsilon_m}{\nu_f} = -\frac{1}{2} + \frac{1}{2} \sqrt{1 + 4K^2 y^{+2} \left[1 - \exp\left(-\sqrt{\frac{\tau}{\tau_w}} \frac{y^+}{A^+}\right) \right]^2} \frac{\tau}{\tau_w}. \quad (4.32)$$

In order to account for interfacial dampening in the condensation film due to surface tension suppression of turbulent eddies, a dampening term, $(1 - y^+/\delta^+)^n$, is included in the above eddy diffusivity profile, where the influence of the parameter n will be discussed later. The complete form of eddy momentum diffusivity distribution in the shear-driven film is expressed as

$$\frac{\varepsilon_m}{\nu_f} = -\frac{1}{2} + \frac{1}{2} \sqrt{1 + 4K^2 y^{+2} \left[1 - \exp\left(-\sqrt{\frac{\tau}{\tau_w}} \frac{y^+}{A^+}\right) \right]^2} \frac{\tau}{\tau_w} \left(1 - \frac{y^+}{\delta^+}\right)^n, \quad (4.33)$$

where, based on Eq. (4.12),

$$\frac{\tau}{\tau_w} = \frac{2(H_{ch} + W_{ch})}{P_{f,y}} \frac{\left(-\frac{dP}{dz}\right) A_{f,*} + \tau_i P_{f,\delta} + \Gamma_{fg} u_i}{\left(-\frac{dP}{dz}\right) [2\delta(H_{ch} + W_{ch}) - 4\delta^2] + \tau_i P_{f,\delta} + \Gamma_{fg} u_i}. \quad (4.34)$$

4.1.5. Determination of Heat Transfer Coefficient

Heat flux across the liquid film is related to the liquid temperature gradient by the relation,

$$\frac{q''}{q''_w} = \left(\frac{1}{\text{Pr}_f} + \frac{1}{\text{Pr}_T} \frac{\varepsilon_m}{\nu_f} \right) dT^+, \quad (4.35)$$

where T^+ is the dimensionless temperature defined as

$$T^+ = \frac{\rho_f c_{p,f} u^* (T - T_w)}{q''_w}, \quad (4.36)$$

and Pr_T is the turbulent Prandtl number (ε_m/Σ_h), which, as discussed by Mudawar and El-Masri (1986), can be evaluated from the experimental data of Ueda *et al.* (1977),

$$\text{Pr}_T = 1.4 \exp\left(-15 \frac{y^+}{\delta^+}\right) + 0.66. \quad (4.37)$$

Integrating Eq. (4.35), the dimensionless temperature profile across the liquid film can be expressed as

$$T^+ = \int_0^{y^+} \frac{q''}{q''_w} \left(\frac{1}{\text{Pr}_f} + \frac{1}{\text{Pr}_T} \frac{\varepsilon_m}{\nu_f} \right)^{-1} dy^+. \quad (4.38)$$

Under three-sided cooling conditions for trapezoidal micro-channels, Quan *et al.* (2010) developed a semi-analytical model for the annular condensation heat transfer coefficient based on the assumption of uniform circumferential heat flux in the vapor-liquid interface. Adopting a heat flux relation similar to that of Quan *et al.*, the present model for condensation in rectangular micro-channels with three-sided cooling walls employs the following energy balance.

$$\frac{q''}{q''_w} = \frac{2H_{ch} + W_{ch}}{2[(H_{ch} - 2y) + (W_{ch} - 2y)]}. \quad (4.39)$$

Therefore, the local condensation heat transfer coefficient can be expressed as

$$h_{tp} = \frac{q''_w}{(T_{sat} - T_w)} = \frac{\rho_f c_{p,f} u^*}{T_\delta^+} = \frac{\rho_f c_{p,f} u^*}{\int_0^{\delta^+} \frac{q''}{q''_w} \left(\frac{1}{\text{Pr}_f} + \frac{1}{\text{Pr}_T} \frac{\varepsilon_m}{\nu_f} \right)^{-1} dy^+}. \quad (4.40)$$

4.1.6. Calculation Procedure

The model equations presented in the previous sections are solved numerically using a finite difference technique. The axial distance is divided into small Δz increments and calculations are repeated starting at the upstream location where the film is initiated. The calculation procedure is as follows:

1. ε_m/ν_f and δ are both set to zero at the film's upstream location.
2. An initial guess of ε_m/ν_f at the next Δz location is made with the values of the wall shear stress, τ_w , interfacial shear, τ_i , interfacial velocity, u_i , and pressure gradient, $-dP/dz$, at the node immediately upstream using Eq. (4.33).
3. An initial value of the film thickness δ is assumed.
4. The interfacial velocity, u_i , interfacial friction factor, f_i , interfacial shear, τ_i , and pressure gradient, $-dP/dz$, are calculated using Eqs. (4.15), (4.21), (4.20), and (4.16), respectively.
5. Convergence is checked by comparing the two sides of Eq. (4.19). If the sides are not equal, ε_m/ν_f is updated with new values of τ_w , τ_i , u_i , and $-dP/dz$ at the present node, and steps (3)-(5) are repeated until the correct value for δ is found.

6. The values of ε_m/ν_f , u^+ , T^+ , and h_{tp} are calculated using Eqs. (4.33), (4.14), (4.38), and (4.40), respectively. Steps (2)-(6) are then repeated for the next downstream node. The procedure is continued until the last node is reached.

4.1.7. Simplified Model

Since the thickness of the condensing film is generally small compared to the micro-channel hydraulic diameter, a simplified model can be derived using the following assumption,

$$P_{f,y} = P_{f,\delta} = P_f = 2(H_{ch} + W_{ch}). \quad (4.41)$$

Then, the flow area and mass flow rate of the liquid film can be expressed, respectively, as

$$A_{f,*} = P_f (\delta - y), \quad (4.42)$$

and

$$\dot{m}_f = \rho_f P_f \int_0^\delta u_f dy. \quad (4.43)$$

Applying momentum conservation to a rectangular annular element of the liquid film yields the following shear stress relation,

$$\frac{\tau}{\tau_w} = \frac{\left(-\frac{dP}{dz}\right)(\delta - y) + \tau_i + \frac{\Gamma_{fg} u_i}{P_f}}{\left(-\frac{dP}{dz}\right)\delta + \tau_i + \frac{\Gamma_{fg} u_i}{P_f}}. \quad (4.44)$$

Similar to the procedure used in previous section, the velocity profile, interfacial velocity, and pressure gradient can be simplified, respectively, as

$$u_f(y) = \frac{\delta^2}{\mu_f} \left(-\frac{dP}{dz}\right) \int_0^{y/\delta} \left(1 - \frac{y}{\delta}\right) \left(1 + \frac{\varepsilon_m}{\nu_f}\right)^{-1} d\left(\frac{y}{\delta}\right) + \frac{\delta}{\mu_f} \left(\tau_i + \frac{\Gamma_{fg} u_i}{P_f}\right) \int_0^{y/\delta} \left(1 + \frac{\varepsilon_m}{\nu_f}\right)^{-1} d\left(\frac{y}{\delta}\right), \quad (4.45)$$

$$u_i = \frac{\delta \left(-\frac{dP}{dz}\right) \int_0^1 \left(1 - \frac{y}{\delta}\right) \left(1 + \frac{\varepsilon_m}{\nu_f}\right)^{-1} d\left(\frac{y}{\delta}\right) + \tau_i \int_0^1 \left(1 + \frac{\varepsilon_m}{\nu_f}\right)^{-1} d\left(\frac{y}{\delta}\right)}{\frac{\mu_f}{\delta} - \frac{\Gamma_{fg}}{P_f} \int_0^1 \left(1 + \frac{\varepsilon_m}{\nu_f}\right)^{-1} d\left(\frac{y}{\delta}\right)}, \quad (4.46)$$

$$\text{and } -\frac{dP}{dz} = \frac{\frac{\mu_f \dot{m}_f}{\rho_f P_f \delta^2} - \left(\tau_i + \frac{\Gamma_{fg} u_i}{P_f} \right) \int_0^1 \left[\int_0^{y/\delta} \left(1 + \frac{\varepsilon_m}{\nu_f} \right)^{-1} d\left(\frac{y}{\delta}\right) \right] d\left(\frac{y}{\delta}\right)}{\delta \int_0^1 \left[\int_0^{y/\delta} \left(1 - \frac{y}{\delta} \right) \left(1 + \frac{\varepsilon_m}{\nu_f} \right)^{-1} d\left(\frac{y}{\delta}\right) \right] d\left(\frac{y}{\delta}\right)}. \quad (4.47)$$

As discussed later, the predictive differences of pressure drop average only 1.8%, with a maximum difference of 3.8%; corresponding differences for the average heat transfer coefficient are 0.5% and 1.0%, respectively. Although both models yield very close results, all of the subsequent calculations are based on the complete model unless indicated otherwise.

4.2. Model Results

4.2.1. Effect of Turbulent Dampening Term

Mudawar and El-Masri (1986) examined the interfacial dampening effects on the turbulence mixing length for free-falling liquid films. They derived the following turbulence mixing length profile based on an eddy-diffusivity profile measured experimentally by Ueda *et al.* (1977) for open-channel flows,

$$l^+ = K y^+ \left[1 - \exp \left(- \sqrt{1 - \frac{y^+}{\delta^+}} \frac{y^+}{A^+} \right) \right] \sqrt{1 - \frac{y^+}{\delta^+}}. \quad (4.48)$$

Substituting Eqs. (4.25) and (4.48) into Eq. (4.29) gives the following eddy diffusivity profile,

$$\frac{\varepsilon_m}{\nu_f} = -\frac{1}{2} + \frac{1}{2} \sqrt{1 + 4K^2 y^{+2} \left[1 - \exp \left(- \sqrt{1 - \frac{y^+}{\delta^+}} \frac{y^+}{A^+} \right) \right]^2 \left(1 - \frac{y^+}{\delta^+} \right) \frac{\tau}{\tau_w}}. \quad (4.49)$$

It should be noted that, since the mixing length profile of Mudawar and El-Masri is valid only for $\varepsilon_m/\nu_f > 1$ and negligible interfacial shear stress, their eddy diffusivity profile cannot be used for micro-channel condensation, where turbulence effects are relatively weak and interfacial shear is the primary driving force for film motion.

The present eddy diffusivity profile given by Eq. (4.33) yielded values for dimensionless film thickness, $y^+ = \delta^+$, up to about 16 at the micro-channel exit, which is

close to the outer edge of the viscous sublayer for typical turbulent flows. The present diffusivity profile is justified by the fact that Van-Driest models are applicable near the solid wall region where $y^+ \leq 30$. The dampening coefficient, $(1 - y^+/\delta^+)^n$, in Eq. (4.33) accounts for the vanishing turbulence effects, if any, at the film interface. Without this term, the conventional Van-Driest profile cannot account for the interfacial dampening.

Using Eq. (4.33), four different powers of the dampening term, $(1 - y^+/\delta^+)^n$, $n = 0$ (corresponding to zero dampening as expressed by Eq. (4.32)), 0.1, 0.5, and 1.0, are examined. Figures 4.3(a), 4.3(b) and 4.3(c) show the impact of the dampening term on the distributions of eddy diffusivity, velocity, and temperature, respectively, across the FC-72 film for $G = 367 \text{ kg/m}^2\text{s}$ and $\dot{m}_w = 6 \text{ g/s}$. Figure 4.3(a) shows that, without the dampening term, the eddy diffusivity increases monotonically with increasing y^+ , while with the dampening term, the eddy diffusivity is reduced to zero at the film interface. Increasing the magnitude of the exponent n causes the effect of interfacial dampening to penetrate deeper towards the wall. Figure 4.3(b) shows that increasing n increases the liquid velocity near the interface. Figure 4.3(c) shows a similar trend of increasing liquid temperature near the interface with increasing n . An interesting aspect of the temperature profile is the unusual temperature rise in the immediate vicinity of the film interface caused by the eddy diffusivity term in Eq. (4.35) approaching zero.

Although Fig. 4.4(a) shows that different n values yield fairly similar film thickness results, Fig. 4.4(b) shows that increasing the power increases the temperature gradient near the interface, which can produce a measureable decrease in the heat transfer coefficient. An optimum value of $n = 0.1$ was ascertained by comparing predictions of the local as well as average heat transfer coefficients with the experimental data in Chapter 3.3. This value is therefore used for all of subsequent calculations.

4.2.2. Effect of Mass Velocity

Figure 4.5 shows predicted variations of several film parameters with quality for different FC-72 mass velocities at a constant water flow rate of 6 g/s. Liquid film and vapor core Reynolds numbers are defined, respectively, as

$$\text{Re}_f = \frac{4\rho_f \bar{u}_f \delta}{\mu_f}, \quad (4.50)$$

and

$$\text{Re}_g = \frac{\rho_g \bar{u}_g D_{h,c}}{\mu_g}, \quad (4.51)$$

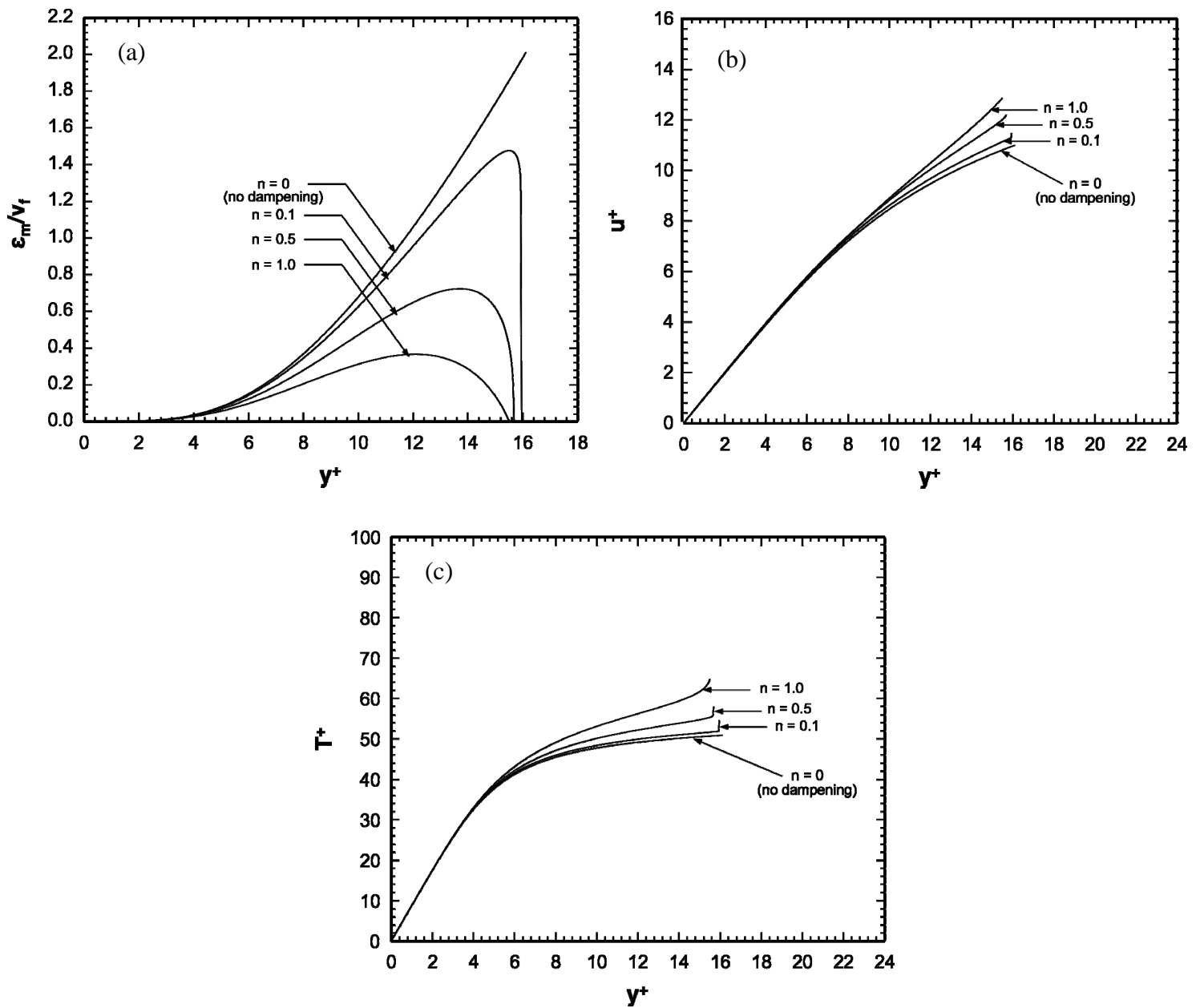


Figure 4.3 Effects of interfacial dampening term on (a) eddy momentum diffusivity, (b) velocity, and (c) temperature distributions across condensing FC-72 film for $G = 367 \text{ kg/m}^2\text{s}$, and $\dot{m}_w = 6 \text{ g/s}$.

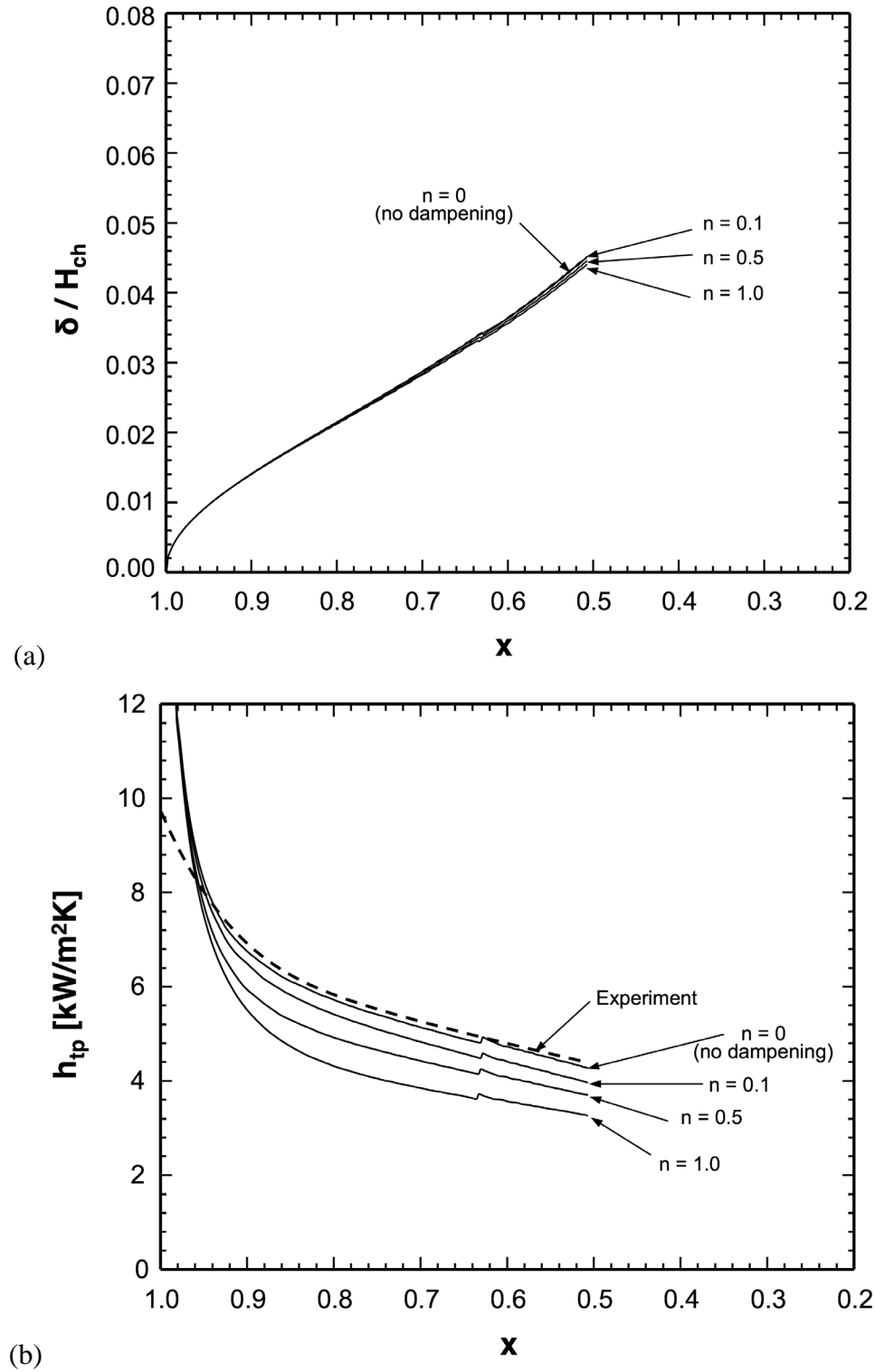


Figure 4.4 Effects of interfacial dampening term on variations of (a) liquid film thickness, and (b) local heat transfer coefficient with quality for $G = 367 \text{ kg/m}^2\text{s}$ and $\dot{m}_w = 6 \text{ g/s}$.

where the mean liquid film velocity, \bar{u}_f , is expressed as

$$\bar{u}_f = \frac{\dot{m}_f}{\rho_f [W_{ch} H_{ch} - (W_{ch} - 2\delta)(H_{ch} - 2\delta)]}. \quad (4.52)$$

Peterson *et al.* (1997) proposed the following correlation for transition from laminar to turbulent film flow for downward flowing films,

$$\text{Re}_{f,tr} = 4080 \left[(1 + 0.31 \tau_i^{*1.07}) (1.18 \text{Pr}_f^{0.87} - 0.23) \right]^{-1}, \quad (4.53)$$

where the nondimensional interfacial shear stress is defined as

$$\tau_i^* = \frac{\tau_i}{\rho_f g (v_f^2 / g)^{1/3}}. \quad (4.54)$$

Based on this correlation, transition to turbulent film flow is estimated to occur at very low film Reynolds numbers when the values of interfacial shear and liquid Prandtl number are high. Using values relevant to the present study, with $\tau_i = 15 \text{ Pa}$ ($\tau_i^* = 50$) and $T_{sat} = 60^\circ\text{C}$ ($\text{Pr}_f = 8.66$), Eq. (4.54) yields a transitional Reynolds number of $\text{Re}_{f,tr} = 25$. Therefore, although Re_f values for the present study are relatively small (less than 400), strong interfacial shear promotes turbulence film flow for most operating conditions. This fact supports assumption (11) used in the development of the present model.

Figures 4.5(a), 4.5(b) and 4.5(c) show that increasing the mass velocity of FC-72 increases the film Reynolds number, vapor core Reynolds number and interfacial shear stress, respectively. The slight discontinuities in the shear stress plots are caused by the different ranges of the effective Reynolds number of the vapor core, Re_c , as indicated by Eqs. 4.21(a) - (c). Figure 4.5(d) shows the film thickness decreasing with increasing mass velocity because of the increased interfacial shear. Figure 4.5(e) shows how the decreasing film thickness with increased mass velocity increases the heat transfer coefficient. For each mass velocity, Fig. 4.5(e) shows that the heat transfer coefficient is greatest where the film is first initiated and decreases monotonically downstream as the film thickens due to gradual condensation along the channel.

4.2.3. Validation of Model Predictions

Figure 4.6(a) compares pressure drop predictions with measured pressure drop data for different water mass flow rates and FC-72 mass velocities of $G = 248, 306$, and $367 \text{ kg/m}^2\text{s}$. This figure proves that the model accurately captures the measured pressure drop in both magnitude and trend.

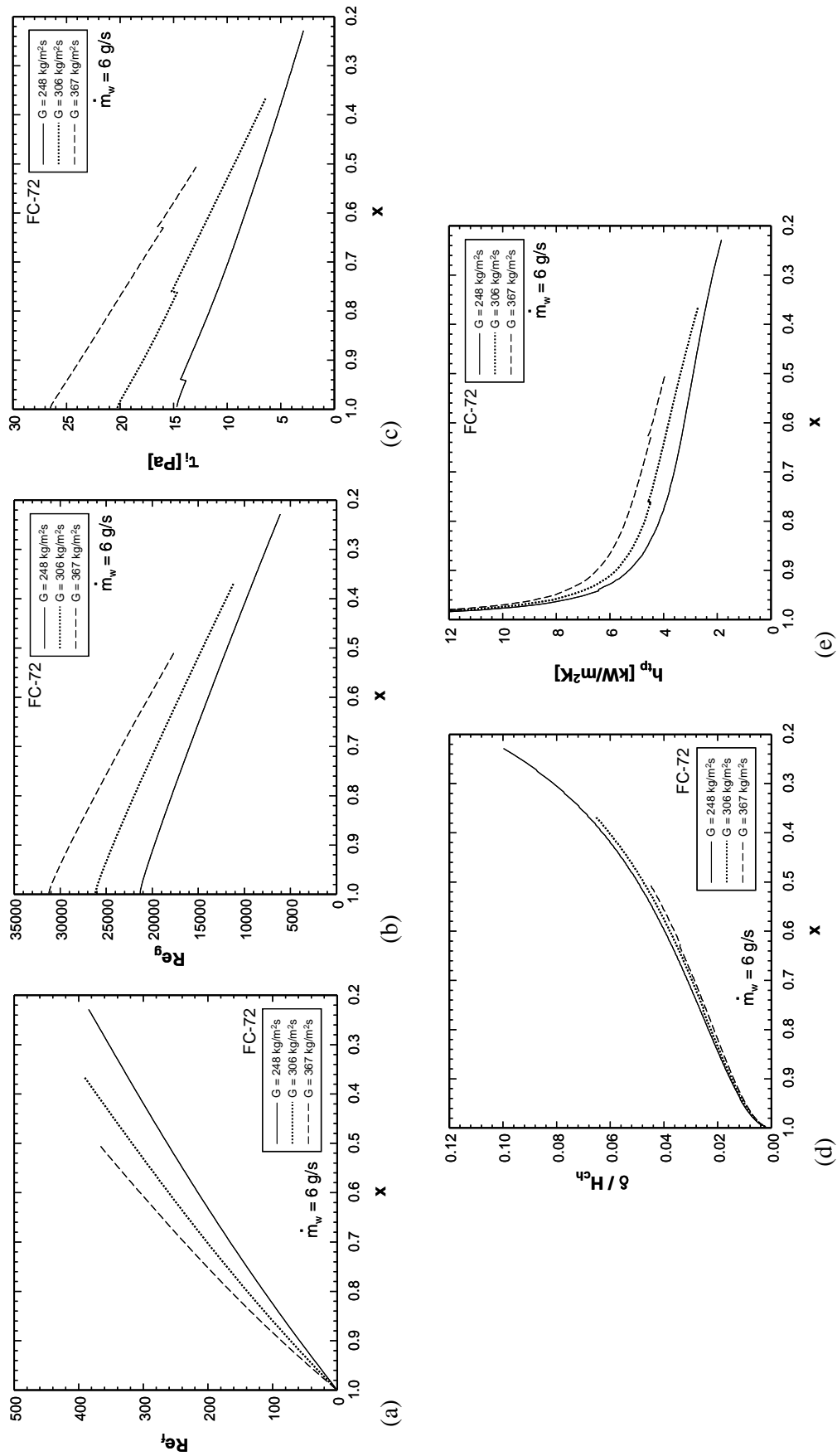


Figure 4.5 Variations of (a) liquid film Reynolds number, (b) vapor core Reynolds number, (c) interfacial shear stress, (d) liquid film thickness, and (e) local heat transfer coefficient with quality for different FC-72 mass velocities and $\dot{m}_w = 6 \text{ g/s}$.

Figure 4.6(b) compares predictions of the present model and nine prior separated flow correlations against the present pressure drop FC-72 data. The correlations include six specifically developed for mini/micro-channels; the other three are intended for macro-channels. All three macro-channel correlations significantly over predict the FC-72 micro-channel data. Among the mini/micro-channel correlations, those by Mishima and Hibiki (1996) and Nino *et al.* (2005), which are both based on air-water adiabatic flow, show fair predictions. Interestingly, these predictions are superior to those of the correlation by Tran *et al.* (2000), which was developed specifically for flow boiling in small channels. This supports the fact that, in the absence of droplet entrainment and deposition effects, micro-channel condensing flows are closer in flow structure (on a local basis) to adiabatic than boiling micro-channel flows as depicted in Fig. 3.8(a). Overall, Fig. 4.6(b) shows the excellent predictive capability of the present theoretical model, evidenced by a MAE of 3.6%.

Figure 4.7(a) compares predictions of the present model and average FC-72 heat transfer coefficient data for different FC-72 mass velocities and water flow rates. The model does capture the experimental trends relative to FC-72 mass velocity and water mass flow rate. Deviations between predicted and measure values may be related to film waviness, which is more prevalent for the lower mass velocity. Waviness can increase the heat transfer coefficient in two ways, by increasing liquid-vapor interfacial area and by decreasing mean film thickness due to the interfacial waves propagating slightly faster than the rest of the liquid. Another reason for the deviations between predicted and measured values is the circumferential non-uniformity of the liquid film, with more liquid driven towards the corners, thinning the film along the flat walls of the micro-channel. Despite the low surface tension of FC-72, corner effects can slightly influence the mean film thickness. Another source of predictive error may be minor stratification in the horizontal channels, especially at low mass velocities.

Figure 4.7(b) compares predictions of the present model and nine prior separated flow correlations against the present average heat transfer coefficient FC-72 data. The correlations include four specifically developed for mini/micro-channels; the other five are intended for macro-channels. Interestingly, excepting the correlation by Akers *et al.* (1958), most macro-channel correlations provide good predictions of the present data. With a MAE of 4.7%, the recent correlation by Kim and Mudawar (in review-a) shows the best predictive capability. Nearly as accurate, the present theoretical model predicts the data with a MAE of 9.3%.

Figure 4.8 compares predictions of the present model and prior correlations with the present local heat transfer coefficient data for three FC-72 mass velocities. Notice that, despite their low MAE in predicting the average heat transfer coefficient data, the correlations of Shah (1979), Cavallini and Zecchin (1974), and Dobson and Chato (1998), do not accurately capture the variation of local heat transfer coefficient with quality. Overall, both the present theoretical model and the recent correlation by Kim and Mudawar (in review-a) show good accuracy in predicting the measured trend of local heat transfer coefficient with quality.

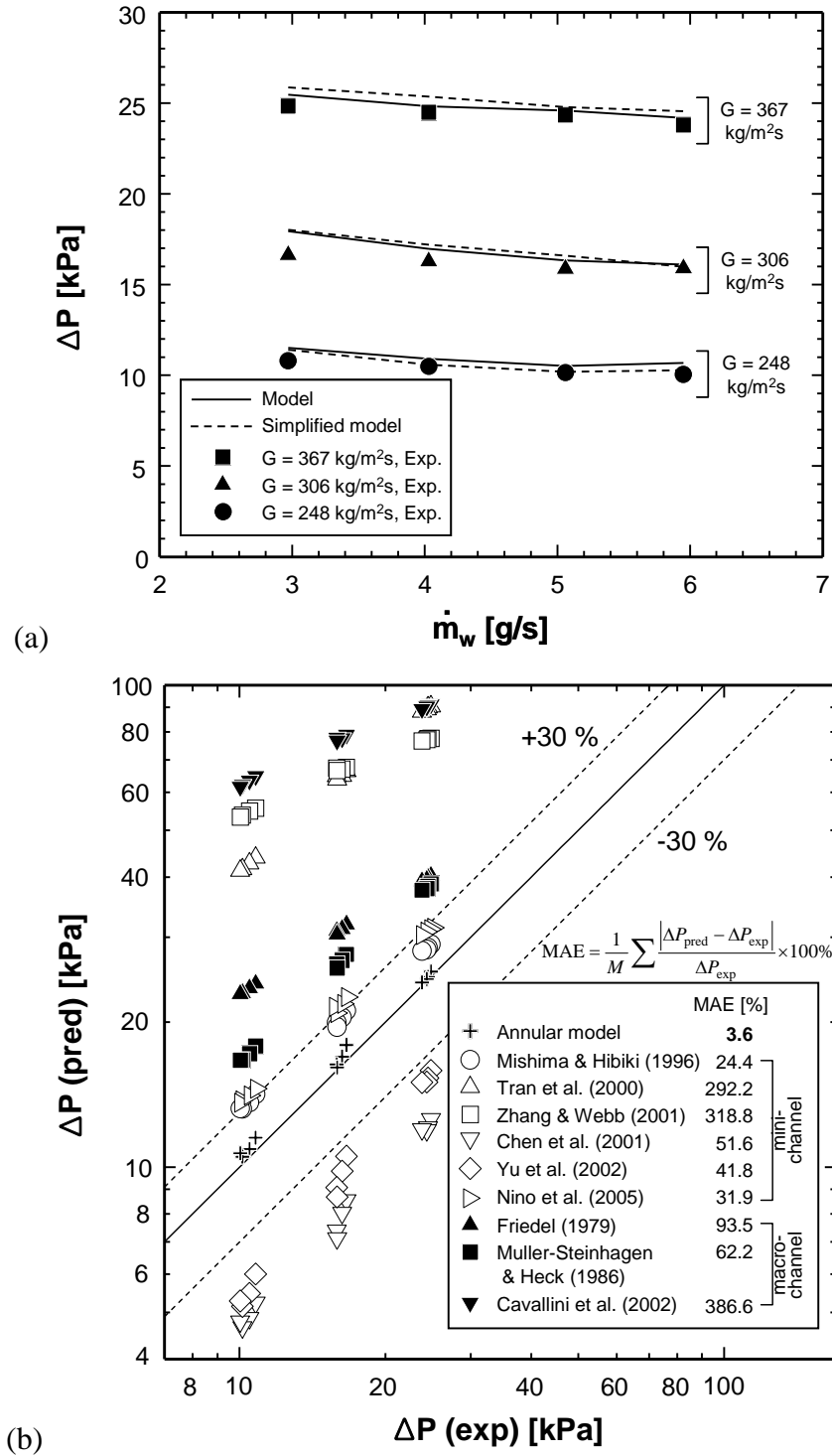


Figure 4.6 (a) Variations of predicted and measured total pressure drops with water mass flow rate for different FC-72 mass velocities. (b) Comparison of measured FC-72 total pressure drop data with predictions of present model and previous correlations.

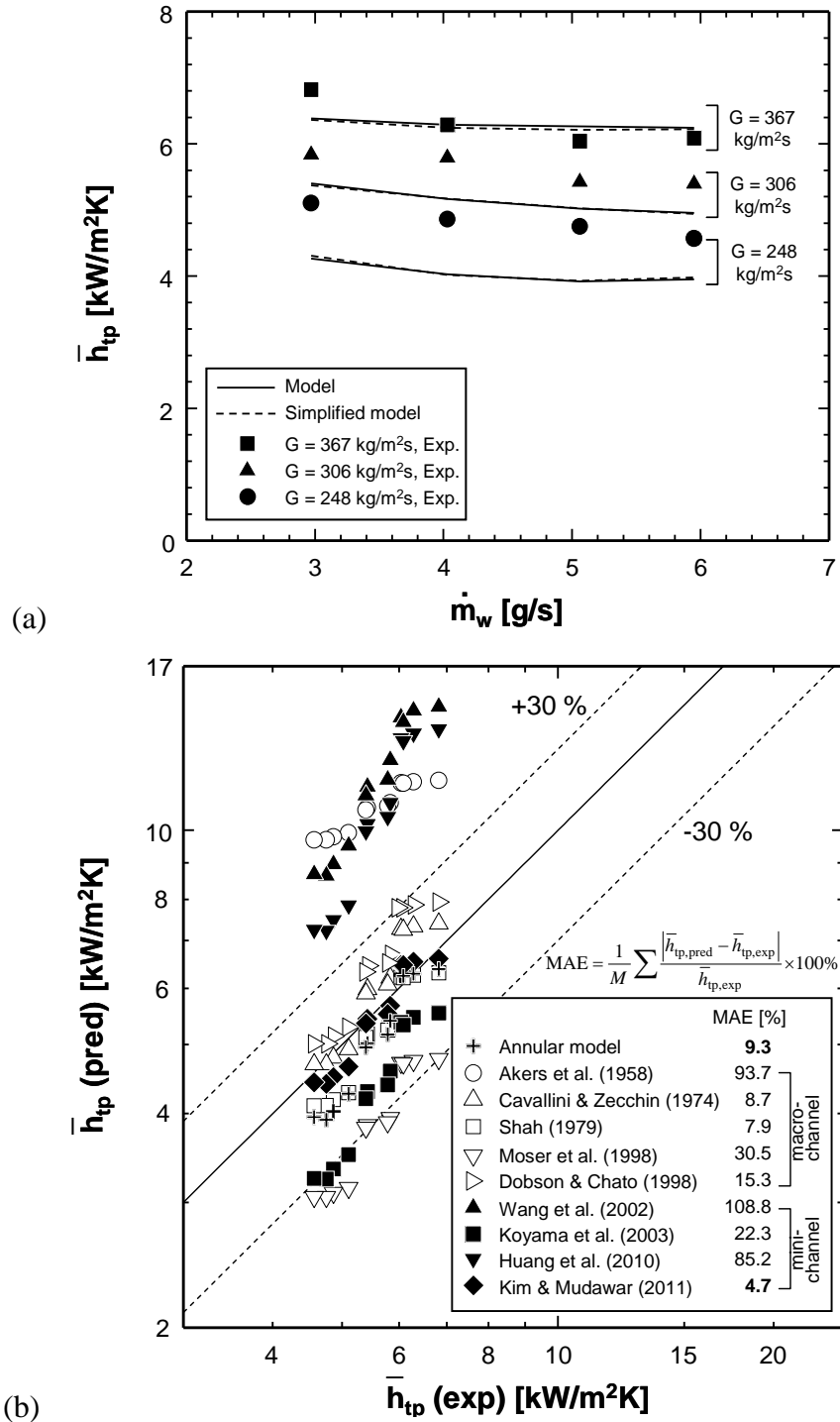


Figure 4.7 (a) Variations of predicted and measured average heat transfer coefficients with water mass flow rate for different FC-72 mass velocities. (b) Comparison of measured FC-72 average condensation heat transfer coefficient data with predictions of present annular model and previous annular condensation heat transfer correlations.

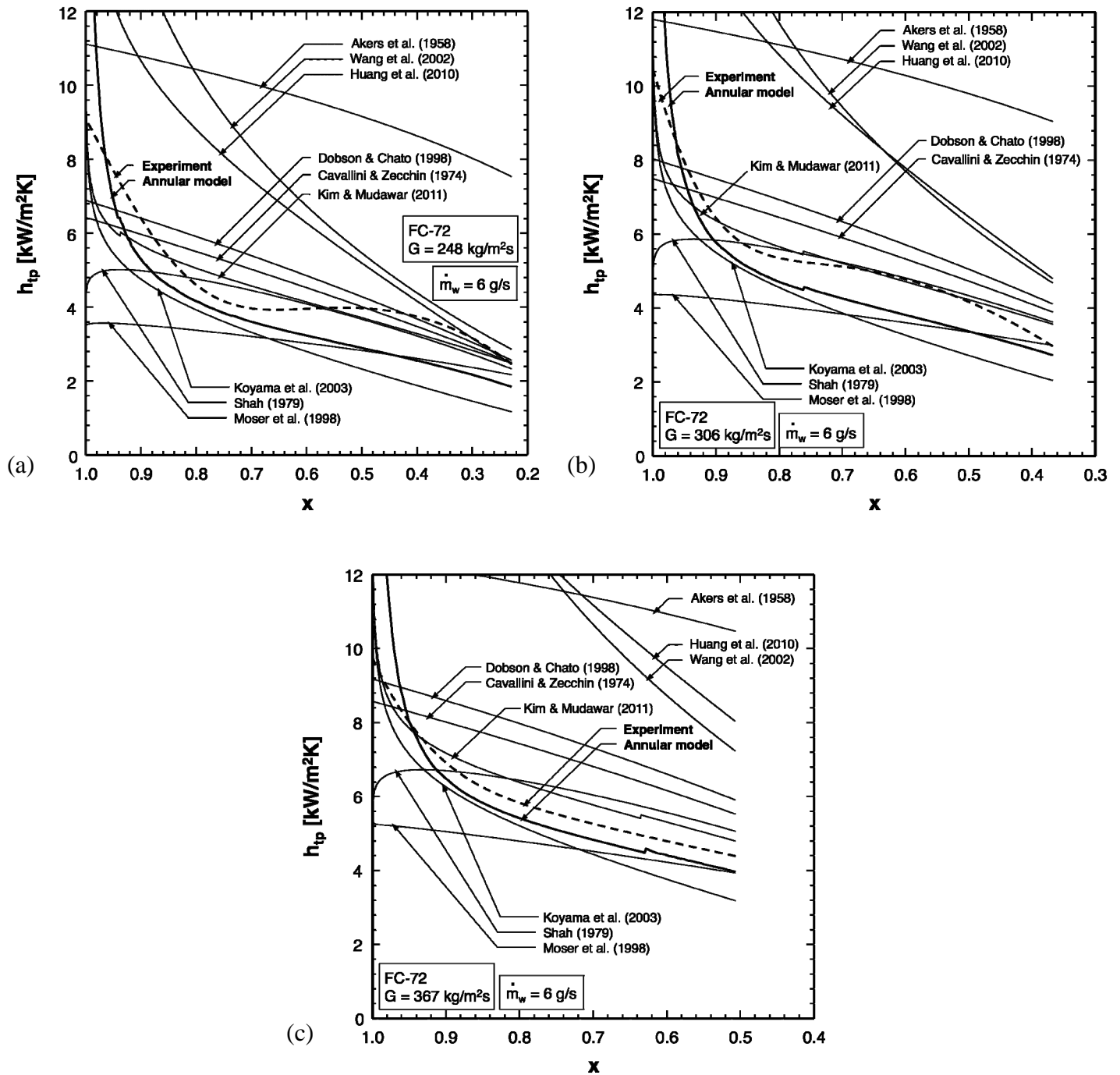


Figure 4.8 Comparison of measured FC-72 local heat transfer coefficient data with predictions of present model and previous annular condensation heat transfer correlations for $\dot{m}_w = 6 \text{ g/s}$ with (a) $G = 248 \text{ kg/m}^2\text{s}$, (b) $G = 306 \text{ kg/m}^2\text{s}$, and (c) $G = 367 \text{ kg/m}^2\text{s}$.

CHAPTER 5. CONCLUSIONS

This study concerns transport phenomena associated with condensation in micro-channels. The construction of the condensation module and flow loop, and the experimental methods used are discussed. High-speed video and photomicrographic techniques are used to explore and help categorize two-phase flow regimes associated with condensation of FC-72 in parallel square channels with $D_h = 1$ mm. The two-phase pressure drop and heat transfer characteristics of the condensation test module are examined. An assessment of the accuracy of prior models and correlations in predicting the present pressure drop as well as the heat transfer data is reported. A theoretical control-volume-based model tailored to turbulent shear-driven films is proposed, and the pressure drop and heat transfer characteristics of annular flow condensation in rectangular micro-channels with three-sided cooling walls are examined.

5.1. Condensation Pressure Drop

The total pressure drop measured between the inlet and outlet plenums was compared to predictions of previous models based on homogenous equilibrium and separated flow models. Key findings from this study are as follows:

(1) Five dominant condensation regimes, smooth-annular, wavy-annular, transition, slug, and bubbly, are identified. Transitions between these regimes are in general agreement with those from previous studies. Based on the current FC-72 flow visualization data, transition lines of flow regime in micro-channel condensation are proposed.

(2) The total pressure drop increases with increasing mass velocity due largely to the increased interfacial shear stress between the vapor core and the annular liquid film. Increasing the flow rate of cooling water decreases the total pressure drop slightly because of increased flow deceleration.

(3) A complete model was constructed for total pressure drop between the inlet and outlet plenums. To calculate the two-phase frictional pressure drop portion of the total pressure drop, different homogenous and separated models were tested. Although annular flow was dominant throughout the present experiments, most homogeneous models unexpectedly provided accurate predictions of the present data. All separated flow macro-channel correlations overpredicted the experimental data, some with very large MAE. Among the separated flow mini/micro-channels correlations, those that are based on adiabatic and condensing two-phase flows provide better predictions than those based on flow boiling. This can be attributed to fundamental differences in local annular flow behavior between condensing and adiabatic flows on one hand and evaporating flows on the other. While entrained droplets play an important role in evaporating flows, no droplets were observed in the present condensation experiments. Overall, weak predictions of separated flow correlations highlight the need of further study and new predictive tools specifically tailored to micro-channel condensing flows.

5.2. Condensation Heat Transfer

FC-72 condensation heat transfer coefficient data were compared to predictions of previous correlations, and a new correlation was developed for the annular regime. The accuracy of this correlation was ascertained against both the present FC-72 data and a large mini/micro-channel database from eight previous sources. Key findings from this study are as follows:

(1) The FC-72 condensation heat transfer coefficient is highest at the point of commencement of the smooth-annular regime, where the annular liquid film is thinnest. The heat transfer coefficient decreases along the micro-channel because of gradual thickening of the liquid film and eventual collapse of the annular regime. For high mass velocities, the variation of the heat transfer coefficient is flatter for intermediate quality values corresponding to the wavy-annular regime, where heat transfer enhancement by the interfacial waves partially compensates for the film thinning.

(2) The FC-72 condensation heat transfer coefficient decreases with increasing water flow rate because of the increased rate of condensation and resulting thickening of the annular liquid film. However, the condensation heat transfer coefficient is less sensitive to variations in water mass flow rate than in FC-72 mass velocity.

(3) In general, prior annular condensation heat transfer correlations intended for macro-channels provide better predictions of the present average FC-72 condensation heat transfer coefficient than more recent correlations intended specifically for mini/micro-channels.

(4) A new condensation heat transfer coefficient correlation is proposed for annular condensation heat transfer in mini/micro-channels. This correlation accurately predicts the present FC-72 average heat transfer data with a MAE of 9.0%.

(5) To further assess the predictive accuracy of the new correlation, a database of 923 data points for mini/micro-channels (including multi-channels and single channels) was amassed from eight previous sources, of which 713 data points correspond to annular flow. The new correlation shows excellent predictive capability based on the 713 annular data, evidenced by an overall MAE of 18.3%.

5.3. Theoretical Model for Annular Flow Condensation

A theoretical control-volume-based model is developed, which is based on the assumptions of smooth interface between the annular liquid film and vapor core, and uniform film thickness around the channel's circumference. The model predictions are compared with experimental micro-channel pressure drop and condensation heat transfer data for FC-72. This study also explored the accuracy of prior separated flow correlations in predicting the same data. Key conclusions from this study are as follows.

(1) Unlike flow boiling, droplet entrainment and deposition effects are nonexistent in micro-channel annular condensing flows.

(2) Annular condensation can be divided into two separate regions, an upstream smooth-annular region and a downstream wavy-annular region. While the annular film in the wavy-annular regime is marred by interfacial waves, these waves are fairly small in profile and do not evolve into large waves, nor do they appear to have an appreciable influence on the film's transport behavior.

(3) For shear-driven films, transition from laminar to turbulent film flow may occur at unusually small film Reynolds numbers. Turbulent effects must therefore be incorporated when modeling the transport behavior of annular condensing films.

(4) Interfacial dampening of turbulent eddies is accurately accounted for in the new model with the aid of a new eddy diffusivity model specifically tailored to turbulent shear-drive films.

(5) While some of the previous separated flow correlations do provide accurate predictions of the average heat transfer coefficient, they fail to predict axial variations of the local condensation heat transfer coefficient.

(6) The present model accurately predicts the pressure drop and heat transfer coefficient data in both magnitude and trend, evidenced by mean absolute error values of 3.6% and 9.3%, respectively.

LIST OF REFERENCES

LIST OF REFERENCES

- Akers, W.W., Deans, H.A., Crosser, O.K., Condensing heat transfer within horizontal tubes, *Chem. Engr. Prog.* 54 (1958) 89-90.
- Allen, W.F., Flow of a flashing mixture of water and steam through pipes and valves, *Trans. ASME* 73 (1951) 257-265.
- Beattie, D.R.H., Whalley, P.B., A simple two-phase frictional pressure drop calculation method, *Int. J. Multiphase Flow* 8 (1982) 83-87.
- Benjamin, N.W., Miller, J.G., The flow of a flashing mixture of water and steam through pipes, *Trans. ASME* 64 (1942) 657-664.
- Bottomley, W.T., Flow of boiling water through orifices and pipes, *Trans. North East Coast Inst. Engrs. Ship Builders* 53 (1936) 65-100.
- Cavallini, A., Censi, G., Col, D.D., Doretti, L., Longo, G.A., Rossetto, L., Condensation of halogenated refrigerants inside smooth tubes, *HVAC&R Research* 8 (2002) 429-451.
- Cavallini, A., Col, D.D., Doretti, L., Matkovic, M., Rossetto, L., Zilio, C., Condensation heat transfer and pressure gradient inside multiport minichannels, *Heat Transfer Engr.* 26 (2005) 45-55.
- Cavallini, A., Zecchin, R., A dimensionless correlation for heat transfer in forced convection condensation, *Proc. 5th Int. Heat Transfer Conf.* 3 (1974) 309-313, Tyoko, Japan.
- Chen, I.Y., Yang, K.-S., Chang, Y.-J., Wang, C.-C., Two-phase pressure drop of air-water and R-410A in small horizontal tubes, *Int. J. Multiphase Flow* 27 (2001) 1293-1299.
- Chen, Q., Amano, R.S., Xin, M., Experimental study of flow patterns and regimes of condensation in horizontal three-dimensional micro-fin tubes, *Heat Mass Transfer* 43 (2006) 201-206.

- Chisholm, D., Two-phase flow in pipelines and heat exchanger, Longman, New York, 1983.
- Chung, P.M.-Y., Kawaji, M., The effect of channel diameter on adiabatic two-phase flow characteristics in microchannels, *Int. J. Multiphase Flow* 30 (2004) 735-761.
- Cicchitti, A., Lombardi, C., Silvestri, M., Soldaini, G., Zavalluilli, R., Two-phase cooling experiments-pressure drop, heat transfer and burnout measurements, *Energia nucleare* 7 (1960) 407-425.
- Collier, J.G., Thome, J.R., Convective boiling and condensation, 3rd ed., Oxford University Press, New York, 1994.
- Dobson, M.K., Chato, J.C., Condensation in smooth horizontal tubes, *ASME J. Heat Transfer* 120 (1998) 193-213.
- Dukler, A.E., Wicks, M., Cleaveland, R.G., Pressure drop and hold up in two-phase flow, *AIChE J.* 10 (1964) 38-51.
- Friedel, L., Improved friction pressure drop correlations for horizontal and vertical two-phase pipe flow, European Two-phase Group Meeting, Ispra, Italy, (1979) Paper E2.
- Geiger, G.E., Sudden contraction losses in single and two-phase flow, PhD Thesis, University of Pittsburgh, PA, 1964.
- Haraguchi, H., Koyama, S., Fujii, T., Condensation of refrigerants HCFC 22, HFC 134a and HCFC 123 in a horizontal smooth tube (1st report), *Trans. JSME (B)* 60 (1994a) 239-244.
- Haraguchi, H., Koyama, S., Fujii, T., Condensation of refrigerants HCFC 22, HFC 134a and HCFC 123 in a horizontal smooth tube (2nd report), *Trans. JSME (B)* 60 (1994b) 245-252.
- Hirofumi, H., Webb, R.L., Condensation in extruded aluminum tubes, Penn State Research Report, Showa Aluminum Corporation, 1995.
- Huang, X., Ding, G., Hu, H., Zhu, Y., Peng, H., Gao, Y., B. Deng, Influence of oil on flow condensation heat transfer of R410A inside 4.18 mm and 1.6 mm inner diameter horizontal smooth tubes, *Int. J. Refrigeration* 33 (2010) 158-169.
- Hubbard, G.L., Mills, A.F., Chung, D.K., Heat transfer across a turbulent falling film with cocurrent vapor flow, *ASME J. Heat Transfer* 98 (1976) 319-320.

- Hwang, Y.W., Kim, M.S., The pressure drop in microtubes and the correlation development, *Int. J. Heat Mass Transfer* 49 (2006) 1804-1812.
- Incropera, F.P., Dewitt, D.P., Fundamentals of heat and mass transfer, 5th ed. Wiley, New York, 2002.
- Jiang, L., Wong, M., Zohar, Y., Forced convection boiling in a microchannel heat sink, *J. Microelectromechanical Systems* 10 (2001) 80-87.
- Jung, D.S., Radermacher, R., Prediction of pressure drop during horizontal annular flow boiling of pure and mixed refrigerants, *Int. J. Heat Mass Transfer* 32 (1989) 2435-2446.
- Kawahara, A., Chung, P.M.-Y., Kawaji, M., Investigation of two-phase flow pattern, void fraction and pressure drop in a microchannel, *Int. J. Multiphase Flow* 28 (2002) 1411-1435.
- Kays, W.M., Heat transfer to the transpired turbulent boundary layer, *Int. J. Heat Mass Transfer* 15 (1972) 1023-1044.
- Kays, W.M., Crawford, M.E., Convective heat and mass transfer, 2nd ed. McGraw-Hill, New York, 1980.
- Kim, S.M., Mudawar, I., Analytical heat diffusion models for different micro-channel heat sink cross-sectional geometries, *Int. J. Heat Mass Transfer* 53 (2010a) 4002-4016.
- Kim, S.M., Mudawar, I., Analytical heat diffusion models for heat sinks with circular micro-channels, *Int. J. Heat Mass Transfer* 53 (2010b) 4552-4566.
- Kim, S.M., Kim, J., Mudawar, I., Flow condensation in parallel micro-channels – Part 1: Experimental results and assessment of pressure drop correlations, *Int. J. Heat Mass Transfer*, in review.
- Kim, S.M., Mudawar, I., Flow condensation in parallel micro-channels – Part 2: Heat transfer results and correlation technique, *Int. J. Heat Mass Transfer*, in review-a.
- Kim, S.M., Mudawar, I., Theoretical model for annular flow condensation in rectangular micro-channels, *Int. J. Heat Mass Transfer*, in review-b.
- Koskie, J.E., Mudawar, I., Tiederman, W.G., Parallel-wire probes for measurement of thick liquid films, *Int. J. Multiphase Flow* 15 (1989) 521-530.

- Koyama, S., Kuwahara, K., Nakashita, K., Yamamoto, K., An experimental study on condensation of refrigerant R134a in a multi-port extruded tube, *Int. J. Refrigeration* 24 (2003) 425-432.
- Lee, H.J., Lee, S.Y., Pressure drop correlations for two-phase flow within horizontal rectangular channels with small heights, *Int. J. Multiphase Flow* 27 (2001) 783–796.
- Lee, J., Mudawar, I., Two-phase flow in high-heat-flux micro-channel heat sink for refrigeration cooling applications: Part I - pressure drop characteristics, *Int. J. Heat Mass Transfer* 48 (2005a) 928-940.
- Lee, J., Mudawar, I., Two-phase flow in high-heat-flux micro-channel heat sink for refrigeration cooling applications: Part II - heat transfer characteristics, *Int. J. Heat Mass Transfer* 48 (2005b) 941-955.
- Lee, J., Mudawar, I., Fluid flow and heat transfer characteristics of low temperature two-phase micro-channel heat sinks – part 1: experimental methods and flow visualization results, *Int. J. Heat Mass Transfer* 51 (2008a) 4315-4326.
- Lee, J., Mudawar, I., Fluid flow and heat transfer characteristics of low temperature two-phase micro-channel heat sinks – part 2: subcooled boiling pressure drop and heat transfer, *Int. J. Heat Mass Transfer* 51 (2008b) 4327-4341.
- Lee, J., Mudawar, I., Experimental investigation and theoretical model for subcooled flow boiling pressure drop in microchannel heat sinks, *ASME J. Electronic Packaging* 131 (2009) 031008.
- Lewis, W.Y., Robertson, S.A., The circulation of water and steam in water-tube boilers and the rational simplification of boiler design, *Proc. Inst. Mech. Engrs., London*, 143 (1940) 147-181.
- Lin, L., Ponnappan, R., Heat transfer characteristics of spray cooling in a closed loop, *International Journal of Heat and Mass Transfer* 46 (2003) 3737-3746.
- Lin, S., Kwok, C.C.K., Li, R.Y., Chen, Z.H., Chen, Z.Y., Local frictional pressure drop during vaporization of R-12 through capillary tubes, *Int. J. Multiphase Flow* 17 (1991) 95-102.
- Lockhart, R.W., Martinelli, R.C., Proposed correlation of data for isothermal two-phase, two-component flow in pipes, *Chem. Eng. Prog.* 45 (1949) 39–48.

- Lyu, T.H., Mudawar, I., Statistical investigation of the relationship between interfacial waviness and sensible heat transfer to a falling liquid film, *Int. J. Heat Mass Transfer* 34 (1991a) 1451-1464.
- Lyu, T.H., Mudawar, I., Determination of wave-induced fluctuations of wall temperature and convective heat transfer coefficient in the heating of a turbulent falling liquid film, *Int. J. Heat Mass Transfer* 34 (1991b) 2521-2534.
- Markson, A.A., Raverse, T., Humphreys, C.G.R., A method for estimating the circulation in steam boiler furnace circuits, *Trans. ASME* 64 (1942) 275-286.
- Matkovic, M., Cavallini, A., Col, D.D., Rossetto, L., Experimental study on condensation heat transfer inside a single circular minichannel, *Int. J. Heat Mass Transfer* 52 (2009) 2311-2323.
- McAdams, W.H., Woods, W.K., Heroman, L.C., Vaporization inside horizontal tubes, II. Benzene-oil mixture, *Trans. ASME* 64 (1942) 193-200.
- Mishima, K., Hibiki, T., Some characteristics of air–water two-phase flow in small diameter vertical tubes, *Int. J. Multiphase Flow* 22 (1996) 703–712.
- Moser, K.W., Webb, R.L., Na, B., A new equivalent Reynolds number model for condensation in smooth tubes, *ASME J. Heat Transfer* 120 (1998) 410-417.
- Mudawar, I., El-Masri, M.A., Momentum and heat transfer across freely-falling turbulent liquid films, *Int. J. Multiphase Flow* 12 (1986) 771-790.
- Mudawar, I., Houpt, R.A., Mass and momentum transport in Falling liquid films laminarized at relatively high Reynolds numbers, *Int. J. Heat Mass Transfer* 36 (1993a) 3437-3448.
- Mudawar, I., Houpt, R.A., Measurement of mass and momentum transport in wavy-laminar falling liquid films, *Int. J. Heat Mass Transfer* 36 (1993b) 4151-4162.
- Mudawar, I., Wadsworth, D.C., Critical heat flux from a simulated electronic chip to a confined rectangular impinging jet of dielectric liquid, *Int. J. Heat Mass Transfer* 34 (1991) 1465-1480.
- Muller-Steinhagen, H., Heck, K., A simple friction pressure drop correlation for two-phase flow in pipes, *Chem. Eng. Process.* 20 (1986) 297-308.

- Nino, V.G., Jassim, E.W., Hrnjak, P.S., Newell, T.A., Flow regime based model for pressure drop predictions in microchannels, University of Illinois at Urbana-Champaign (2005) ACRC TR-242.
- Owens, W.L., Two-phase pressure gradient. Int. Dev. Heat Transfer, Pt. II., ASME, New York, 1961.
- Park, C.Y., Hrnjak, P., CO₂ flow condensation heat transfer and pressure drop in multi-port microchannels at low temperatures, Int. J. Refrigeration 32 (2009) 1129-1139.
- Peterson, P.F., Schrock, V.E., Kuhn, S.Z., Recent experiments for laminar and turbulent film heat transfer in vertical tubes, Nuclear Engineering Design 175 (1997) 157-166.
- Qu, W., Mudawar, I., Measurement and prediction of pressure drop in two-phase micro-channel heat sinks, Int. J. Heat Mass Transfer 46 (2003a) 2737-2753.
- Qu, W., Mudawar, I., Flow boiling heat transfer in two-phase micro-channel heat sinks-I. Experimental investigation and assessment of correlation methods, Int. J. Heat Mass Transfer 46 (2003b) 2755-2771.
- Qu, W., Mudawar, I., Flow boiling heat transfer in two-phase micro-channel heat sinks-II. Annular two-phase flow model, Int. J. Heat Mass Transfer 46 (2003c) 2773-2784.
- Qu, W., Mudawar, I., Transport phenomena in two-phase micro-channel heat sinks, ASME J. Electronic Packaging 126 (2004) 213-224.
- Quan, X., Cheng, P., Wu, H., An experimental investigation on pressure drop of steam condensing in silicon microchannels, Int. J. Heat Mass Transfer 51 (2008) 5454-5458.
- Quan, X., Dong, L., Cheng, P., Determination of annular condensation heat transfer coefficient of steam in microchannels with trapezoidal cross sections, Int. J. Heat Mass Transfer 53 (2010) 3670-3676.
- Shah, M.M., A general correlation for heat transfer during film condensation inside pipes, Int. J. Heat Mass Transfer 22 (1979) 547-556.
- Shah, R.K., London, A.L., Laminar flow forced convection in ducts: a source book for compact heat exchanger analytical data, Supl 1, Academic press, New York, 1978.
- Shmerler, J.A., Mudawar, I., Local heat transfer coefficient in wavy free-falling turbulent liquid films undergoing uniform sensible heating, Int. J. Heat Mass Transfer 31 (1988a) 67-77.

- Shmerler, J.A., Mudawar, I., Local evaporative heat transfer coefficient in turbulent free-falling liquid films, *Int. J. Heat Mass Transfer* 31 (1988b) 731-742.
- Soliman, H.M., The mist-annular transition during condensation and its influence on the heat transfer mechanism, *Int. J. Multiphase Flow* 12 (1986) 277-288.
- Sturgis, J.C., Mudawar, I., Critical heat flux in a long, rectangular channel subjected to one-sided heating-II. Analysis of critical heat flux data, *Int. J. Heat Mass Transfer* 42 (1999) 1849-1862.
- Tran, T.N., Chyu, M.-C., Wambsganss, M.W., France, D.M., Two-phase pressure drop of refrigerants during flow boiling in small channels: an experimental investigation and correlation development, *Int. J. Multiphase Flow* 26 (2000) 1739-1754.
- Triplett, K.A., Ghiaasiaan, S.M., Abdel-Khalik, S.I., Sadowski, D.L., Gas-liquid two-phase flow in microchannels Part I: two-phase flow patterns, *Int. J. Multiphase Flow* 25 (1999) 377-394.
- Ueda, H., Moller, R., Komori, S., Mizushima, T., Eddy diffusivity near the free surface of open channel flow, *Int. J. Heat Mass Transfer* 20 (1977) 1127-1136.
- Van Driest, E.R., On turbulent flow near a wall, *J. Aeronautical Sciences* 23 (1956) 1007-1011.
- Wallis, G.B., *One dimensional two-phase flow*, McGraw-Hill, New York, 1969.
- Wang, C.C., Chiang, C.S., Lu, D.C., Visual observation of two-phase flow pattern of R-22, R-134a, and R-407C in a 6.5-mm smooth tube, *Exp. Thermal Fluid Sci.* 15 (1997) 395-405.
- Wang, W.-W., Radcliff, T.D., Christensen, R.N., A condensation heat transfer correlation for millimeter-scale tubing with flow regime transition, *Exp. Thermal and Fluid Sci.* 26 (2002) 473-485.
- Yang, C.-Y., Webb, R.L., Condensation of R-12 in small hydraulic diameter extruded aluminum tubes with and without micro-fins, *Int. J. Heat Mass Transfer* 39 (1996) 791-800.
- Yan, Y.-Y., Lin, T.-F., Condensation heat transfer and pressure drop of refrigerant R-134a in a small pipe, *Int. J. Heat Mass Transfer* 42 (1999) 697-708.

Yu, W., France, D.M., Wambsganss, M.W., Hull, J.R., Two-phase pressure drop, boiling heat transfer, and critical heat flux to water in a small-diameter horizontal tube, *Int. J. Multiphase Flow* 28 (2002) 927-941.

Zhang, M., A new equivalent Reynolds number model for vapor shear-controlled condensation inside smooth and micro-fin tubes, PhD Thesis, The Pennsylvania State University, PA, 1998.

Zhang, M., Webb, R.L., Correlation of two-phase friction for refrigerants in small-diameter tubes, *Exp. Thermal Fluid Sci.* 25 (2001) 131–139.

Zhi-qing, W., Study on correction coefficients of laminar and turbulent entrance region effect in round pipe, *Applied Mathematics Mechanics* 3 (1982) 433-446.

Zivi, S.M., Estimation of steady-state steam void-fraction by means of the principle of minimum entropy production, *ASME J. Heat Transfer* 86 (1964) 247-252.